STABILITY ANALYSIS AND CONTROL DESIGN IN SMART GRID WITH RENEWABLE INTEGRATION AND TOPOLOGY CONTROL

A Dissertation

by

WENZONG WANG

Submitted to the Office of Graduate and Professional Studies of
Texas A&M University
in partial fulfillment of the requirements for the degree of

DOCTOR OF PHILOSOPHY

Chair of Committee,	Garng M. Huang
Committee Members,	Chanan Singh
	P. R. Kumar
	Erick Moreno-Centeno
Head of Department,	Miroslav M. Begovic

May 2019

Major Subject: Electrical Engineering

ABSTRACT

The increasing penetration of variable energy resources such as wind and solar is changing the dynamic characteristics of power systems. As the majority of variable energy resources are asynchronously connected to the grid through power converter based generators (CBGs), power system stability is affected significantly by this new type of generator and new stability issues are emerging. Meanwhile, the flexible operation of future power grids, especially the active transmission topology control (TTC) will introduce frequent disturbances to the system and pose threats to power system stability.

With the aforementioned background, the first aim of this dissertation is to analyze the impact of CBGs and TTC on power system stability while the second aim is to design a control method for battery energy storage system (BESS) that can improve the transient stability of power systems and therefore better accommodate the variability and the flexible operation of the future smart grid.

The main results of this research are listed as follows:

- Based on the linearized system model, the mechanism of dynamic interaction between CBGs and synchronous generators is revealed and the conditions for strong interactions are identified.
- The transient stability mechanism of CBGs is analyzed and an index to quantify the transient stability margin of CBGs is proposed. The index can be obtained analytically without running dynamic simulations.

- The impact of TTC on power system stability is investigated. Various forms of instability that can be triggered by TTC are identified and discussed. A simulation based method to assess system stability efficiently following a TTC action is proposed.
- A novel wide area control method is proposed for BESSs to improve power system transient stability. The proposed control method has clear physical meanings and does not require system model or post-disturbance steady state information, which makes it suitable for future smart grid application with uncertainties and constantly changing operating conditions.

DEDICATION

To my beloved parents, wife and son.

ACKNOWLEDGEMENTS

I would like to express my sincere gratitude to my committee chair, Dr. Garng M. Huang. Throughout my Ph.D. study, I enjoyed his guidance and have learned a tremendous amount of knowledge from him. His interest and passion for scientific research and his rigorous attitude towards research and teaching have influenced me a lot. I am fortunate to be mentored by him.

I would also like to thank Dr. Chanan Singh, Dr. P. R. Kumar and Dr. Erick Moreno-Centeno to serve as my committee members. I have enjoyed the classes they offered.

Last but not the least, I want to thank my parents for their unselfish love and support. Special thanks go to my wife for all the sacrifices she made during my study. I will treasure all the happiness and bitterness we shared along the road. Becoming a father is a challenge yet a huge blessing for me. I would like to thank my son for all the laughers as well as the sleepless nights he brought to me that made my life colorful.

CONTRIBUTORS AND FUNDING SOURCES

This work was supervised by a dissertation committee consisting of Professor Garng M. Huang (advisor) and Professors Chanan Singh, P. R. Kumar of the Department of Electrical and Computer Engineering and Professor Erick Moreno-Centeno of the Department of Industrial and Systems Engineering. All work conducted for the dissertation was completed by the student independently.

The work was in part supported by U.S. Department of Energy, ARPA-E program, Robust Adaptive Topology Control (RATC), project award number: DE-AR0000220.

This work was made possible by NPRP grant # 7-106-2-053 from the Qatar National Research Fund (a member of Qatar Foundation).

The work was also partly supported by Electric Power Research Institute (EPRI), project title Limitations of Positive Sequence Models in Comparison with Three-Phase Models for Weak System Studies.

The contents herein are solely the responsibility of the authors.

NOMENCLATURE

AEP	American Electric Power
AGC	Automatic generation control
BESS	Battery energy storage system
CBG	Converter based generator
CCT	Critical clearing time
CoB	Coupling bus
COI	Center of inertia
DFIG	Doubly fed induction generator
ERCOT	Electric Reliability Council of Texas
FACTS	Flexible alternating current transmission system
GE	General Electric
GSC	Grid side converter
HSC	High short circuit
LSC	Low short circuit
LVRT	Low voltage ride through
MSC	Machine side converter
MPPT	Maximum power point tracking
PCC	Point of common coupling
PEBS	Potential energy boundary surface
PF	Participation factor

PJM	Pennsylvania New Jersey Maryland Interconnection
PLL	Phase locked loop
PSS	Power system stabilizer
SCR	Short circuit ratio
SG	Synchronous generator
SMIB	Single machine infinite bus
TTC	Transmission topology control
WSCR	Weighted short circuit ratio
WTG	Wind turbine generator

TABLE OF CONTENTS

Page

LIST OF FIGURES

Page

LIST OF TABLES

Page

1. INTRODUCTION

1.1. Background and Motivation

Power systems all over the world have witnessed the increasing penetration of variable energy resources (VERs) in the past decade. For instance, the cumulative additions of utility-level VERs to the North American power system have surpassed 100 GW in 2016 [1]. This trend will continue as various countries and regions around the world are aiming at a higher percentage of renewable penetration in the future.

The influence of this trend on power system dynamics and stability is crucial in three aspects:

1) The increasing penetration of VERs will change the dynamic characteristics of power systems. Unlike the traditional energy resources, the majority of VERs such as wind and solar are asynchronously connected to the grid through power converter interfaced generators, commonly referred to as converter-based generators (CBGs) [1]. As more and more CBGs are connected to the system, power system dynamics are no longer dominated by synchronous machines (SMs) but become a mixture of SM and CBG dynamics.
2) The power grid will be operated more flexibly, driven by the high penetration of VERs. In traditional power systems, the load and generations are relatively predictable and well planned. The topology of the system is rather fixed and the power flow patterns well defined. In the future power grid, however, in order to accommodate the variability and to achieve high utilization rate of the VERs, power system topology,

generation/load dispatch as well as power flow patterns need to be constantly changed. Consequently, the future power grid is constantly disturbed and undergoes dynamic transitions more frequently.

3) The future power grid will operate closer to stability limits. In traditional power systems the operating conditions are well planned with sufficient stability margin. The increasing share of renewable energy leads to an increase of uncertainties in the availability of energy which will cause more unplanned scenarios with reduced stability margins. Therefore the future power grid will operate close to the stability limits more frequently and are thus more vulnerable to disturbances [2].

Stability analysis and control design in this new environment are critical in realizing the future smart grid with high renewable penetrations. Toward this goal, the following research are motivated:

1) To understand the dynamics of CBGs and their impact on power system stability. Since CBGs have different dynamics from the traditional SMs, it is important to understand the stability mechanism of this new type of generator and its influence on power system stability.

2) To understand the influence of the flexible grid operation, especially the transmission topology control (TTC) on power system stability. TTC is a promising technique that has been demonstrated to be beneficial to the system in both normal and emergency operating conditions [3]–[6]. However, the stability impact of TTC still needs to be understood in order to implement it in practice.

3) Control design to improve power system stability in order to accommodate the flexible operation of future power grids with increased uncertainties. Specifically, control of battery energy storage system (BESS) is explored to improve power system transient stability due to its fast power regulating capability.

1.2. Literature Review

In this section, the current literature related to the research topics in this dissertation are reviewed and discussed.

1.2.1. Impact of CBGs on Power System Small Signal Stability

Power system small signal stability concerns mostly about the electro-mechanical oscillations among synchronous generators (SGs), especially the inter-area oscillations where SGs in different areas are involved and thus have a greater impact on the system compared to the local oscillations.

Tremendous research efforts have been devoted to assess the impact of different types of CBGs on power system electro-mechanical oscillations. Unlike synchronous generators (SGs), the mechanical part of CBGs is decoupled from the grid and does not participate in the electro-mechanical oscillations. Because of this characteristic, it has been widely accepted that there are mainly three mechanisms by which the CBGs can affect the damping of the electro-mechanical oscillation modes [7]:

- Displacing SGs and the associated controls
- Impacting the power flow of the system
- CBG controls interacting with SGs

Among different types of CBGs, variable speed wind generators, especially doubly fed induction generators (DFIGs) have attracted the most attention due to their growing numbers in the system. Reference [8]–[10] studied different scenarios of wind power penetration in different test systems and evaluated their effect on the electro-mechanical oscillation damping based on eigenvalue calculations. Factors such as penetration level, tie line flow level and wind plant locations were discussed. However, the three mechanisms by which the CBGs affect the electro-mechanical modes were considered together so the level of dynamic interaction between the wind power generators and the SGs was unclear.

Reference [11]–[13] assessed the DFIG's effect on the electro-mechanical modes. By modeling the DFIG as a static power source (negative load) in the first step, the influence of power flow change on the electro-mechanical modes was evaluated. Comparing with the case where DFIG was modeled dynamically, the influence of DFIG dynamic interactions was evaluated separately. Participation factors were used to measure the DFIG's participation in the electro-mechanical modes. Results from these references suggest that the participation of DFIG state variables in the electro-mechanical mode is very low and thus the static power model is often adequate to capture the influence of DFIGs on the electro-mechanical modes.

Reference [14] and [15] used the DFIG model with detailed control loops developed by General Electric to study its impact on electro-mechanical oscillations. It was observed in [14] that the reactive power control loop of the DFIG introduces an oscillatory mode whose frequency falls in the range of electro-mechanical oscillations

(0.1Hz to 2Hz). DFIG's influence on the electro-mechanical mode was found to be highly dependent on parameters of this control loop [14] [15]. [16] presented eigenvalue analysis for the Western Electricity Coordinating Council (WECC) system with projected renewable generation conditions. An oscillation mode involving both wind turbine and SG state variables and covering a wide geographic region was observed. It was found that the wind generator reactive power control state variables have the highest participation in this mode. Results in [14] to [16] indicate that the DFIG dynamics can influence the electro-mechanical oscillations at least in certain conditions and are not in line with the conclusions from reference [11] to [13].

The aforementioned studies mainly focused on case studies with different system configurations, operating conditions and control structures/parameters, which leads to different conclusions under different scenarios. The underlying mechanism of the dynamic interaction between CBGs and SGs needs to be revealed to truly understand the impact of CBGs on power system small signal stability and to interpret results obtained from the various case studies.

1.2.2. Transient Stability Analysis of CBGs

Power system transient stability concerns about the system stability following a large disturbance (e.g. a short circuit fault). When the renewable penetration level is low, the support for grid frequency and voltage is mainly provided by SGs. The CBGs can be disconnected from the grid during low voltage conditions after a fault to protect the converters and to avoid transient instability of the CBGs. In this scenario, transient

stability is mainly studied with respect to rotor angle dynamics and the synchronization among SGs.

As the penetration level of CBGs increases, many grid codes require that the CBGs stay connected to the grid and provide voltage and frequency support during the low voltage condition after a fault in the system [1]. This is commonly referred to as the low voltage ride through (LVRT) operation of CBGs.

So far CBGs can be categorized into grid-forming and grid-following CBGs. The grid-forming ones such as the virtual synchronous generators have dynamics and stability mechanism similar to SGs. On the other hand, the grid-following CBGs are synchronized to the grid via phase locked loops (PLL). It is important that the PLL maintains its stability and tracks the angle of the terminal voltage in a fast and accurate manner to ensure reliable and accurate operation of the control structure of a CBG. Losing PLL stability can result in severe power/voltage deviations and may even cause tripping of the CBGs. Since the grid-following CBGs have dynamics different from the SGs, their transient stability mechanism needs to be established and understood.

Transient instability of PLL-synchronized CBGs during the LVRT caused by grid faults was studied in [17]-[20]. The instability is characterized by the drifting of the PLL frequency and is attributed to the lack of a steady state solution during the LVRT [18]-[20]. However, as pointed out in [17], converter dynamics also need to be considered since the existence of a stable equilibrium does not imply stability following a large disturbance. The work in [17] considered the PLL dynamics and offered a basic dynamic view of the grid synchronization process. However, factors that impact the transient stability of the

CBG were not analyzed and the dynamic interaction between PLL and other control loops were ignored. Moreover, the previous work in [17]-[20] studied the dynamic behavior and transient stability of CBGs only during the fault. However, even if a CBG loses synchronization with the grid during a fault, it may still resynchronize to the grid and restore normal operation if the fault is cleared fast enough. Hence CBG dynamics during and after the fault should be considered together to fully assess the CBG transient stability.

1.2.3. Impact of TTC on Power System Stability

The study on the impact of TTC on power system stability is relatively limited in the literature. This may be due to the fact that TTC is not practiced in the real world so far. Since the power system with traditional energy resources has relatively little uncertainty and the flow patterns in the system are well-defined, the demand for more efficient use of the transmission resources is not significant. However, with increasing penetration of the renewable resources in the smart grid and with more flexible load demand, planned and even unplanned changes in power flows and congestion patterns will increase in both frequency and magnitude [21]. Therefore, TTC can play a much more important role in the future smart grid. The impact of TTC on inter-area oscillations in large scale traditional power systems was investigated in [21] and [22]. It was found that different TTC actions can have different effects on inter-area modes (either increase or decrease the damping), and only a small number of TTC actions has the potential to impair system dynamic performance. An efficient way to update the critical eigenvalues of the system after a TTC action was also proposed in [21].

As the integration of CBGs introduces new dynamics into power system, the impact of TTC on system stability needs to be studied in the new smart grid environment with renewable integrations. The impact of TTC on the stability of CBGs also needs to be analyzed.

1.2.4. Control Design for BESS to Improve Power System Stability

As the technology matures for BESS, more and more utility-scale BESSs are employed in power systems [23]. The research on utilizing BESS to improve power system stability mainly focus on two aspects. The first area of research is on small signal stability of the system. BESSs have been shown to be effective in increasing damping of power system oscillations in [23] to [26]. Even though small signal stability is important for power system operation, there are plenty of methods to improve the damping of small signal oscillations including the use of power system stabilizer (PSS) and flexible alternating current transmission system (FACTS).

The second area is on utilizing BESS to improve power system transient stability. Since BESS has the ability to fast inject or absorb power after a disturbance, it is a good candidate to improve power system transient stability. Also, as mentioned in section 1.1, future power system will operate closer to the stability limits and undergo frequent changes in topology and operating conditions, which makes it more challenging to maintain transient stability of the system. Therefore, transient stability improvement using BESS is focused in this dissertation.

Research in this area are relatively limited. [27] applied the interconnection and damping assignment passivity-based control (IDA-PBC) theory to design the control law

for the BESS together with the static synchronous compensator (STATCOM). However, this method needs to find the steady state solution of the post-disturbance system to design the control. Also, it requires the complete dynamic model of the system. [28] designed a distributed control method where it assigns a desired rotor angle to each SG and ensure that the actual rotor angle tracks the desired value. Steady state information of the post-disturbance system is also relied upon to find the desired rotor angles. [29] proposed a linear optimal control method which requires the linearized model of the whole system. However, the linear approach may not work when the disturbance is large.

As can be seen, the existing control method for BESS to improve power system transient stability either requires the complete dynamic model of the system or requires the knowledge of the post-disturbance steady state. In practice, neither of the two requirements is easy to be met. The complete dynamic model of a realistic power system is hard to be obtained or verified and the steady state information after a disturbance (or a set of disturbances) is practically unknown and unpredictable since the topology and power generation may change during the disturbance due to protection operations. Therefore, a control method that is robust to steady state conditions and dynamic modeling uncertainties is highly desired and is sought after in this work.

1.3. Dissertation Outline

The rest of the dissertation is organized as follows:

Section 2 investigate the impact of converter based generators (CBGs) on power system small signal stability. An oscillation mode originated from the reactive power/voltage control loop of the CBG is first analyzed using damping torque analysis.

Influence of different control parameters and system operating conditions on the damping of this mode is revealed through the analysis. Its dynamic coupling with the SG electromechanical oscillation mode is then analyzed and explained based on the mode coupling theory. Conditions when the CBG dynamics have high influence on power system inter-area oscillations are then identified.

In section 3, the limitations of the positive sequence models for CBGs are revealed. Transient stability mechanism of the CBGs is then analyzed. Subsequently, a novel analytical method to evaluate the transient stability margin of the CBGs considering detailed control loops is proposed. Numerical simulations are then carried out to demonstrate the effectiveness of the proposed method. The advantage of the proposed method over the short circuit ratio (SCR) based method in evaluating the transient stability margin of the CBGs is also discussed.

Section 4 investigate the impact of TTC on power system stability and propose a simulation based method to assess different forms of stability all together following a TTC action. Firstly, the impact of TTC on system transient stability margin is discussed. The impact of TTC on power system small signal stability is then investigated in a traditional power system considering different loading levels. Renewable integration is then considered and the impact of TTC on power system small signal stability as well as nonlinear oscillations is investigated. Measures to improve power system small signal stability to better accommodate the TTC actions are discussed and a simulation based method is proposed at last to assess system overall stability after a TTC action.

Section 5 explores the opportunity to improve power system transient stability utilizing the BESS. A novel wide area control method is proposed using SG rotor speeds relative to the center of inertia speed as feedback signals. The proposed method does not require knowledge of the system model or the post-disturbance steady state information. It is proved theoretically that the proposed control method can stabilize the system given certain conditions. Its effectiveness and advantage over a local damping control method is then demonstrated through simulation studies.

Section 6 concludes the dissertation and provides directions for future research.

2. IMPACT OF CONVERTER-BASED GENERATORS ON POWER SYSTEM SMALL SIGNAL STABILITY*

In this section, considering a DFIG model with detailed control loops, an oscillatory mode originated from the DFIG reactive power/voltage control loop (referred to as VAR controller mode for simplicity) is first investigated using damping torque analysis. Impact of operating condition change on its damping and frequency is shown analytically. The coupling between the VAR controller mode and an inter-area electro-mechanical mode in a two-area test system is then explored. The mechanism of dynamic interaction between CBGs and SGs are revealed and explained using mode coupling theory.

This work shed light on understanding the mechanism by which the CBG dynamics affect the electro-mechanical oscillations dominated by SGs. It is revealed that the CBG dynamics have strong effect on the electro-mechanical oscillations only when it has a converter control mode with a frequency similar to the electro-mechanical mode. This helps to explain the diverse conclusions based on case studies in the previous literature reviewed in section 1.2.1.

* © [2017] IEEE. Reprinted, with permission, from [W. Wang and G. M. Huang, Impacts of DFIG reactive power/voltage control on power system oscillations through mode coupling, 2017 IEEE Power & Energy Society General Meeting, 07/2017]

2.1. DFIG Modeling

The General Electric DFIG model with detailed control loops as incorporated in the commercial software PSS/E and PSLF is used. Details about the model can be found in [30] and [31]. The generator and the reactive power control models are illustrated in detail next.

2.1.1. Generator/Converter Model

The generator is modeled as a controlled current source (shown in Figure 2.1) that tracks the active and reactive current commands from the electrical control model [31].

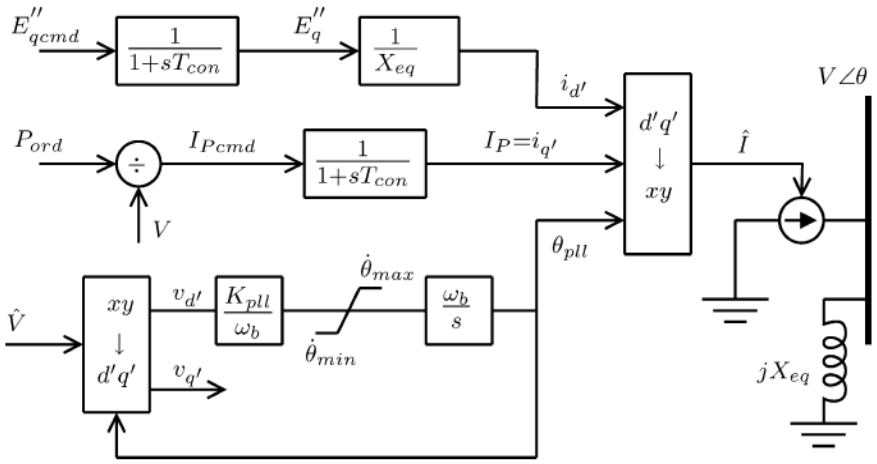

Figure 2.1 Generator/Converter model: Reprinted with permission from [© 2017, IEEE]

Both stator and rotor dynamics are eliminated with two time delay blocks added. In this work, an ideal phase-locked loop (PLL) is assumed, so the q axis of the dq reference frame is perfectly aligned with the terminal voltage vector. Thus the current and reactive power injection into the grid can be found as in (2.1). The d axis is assumed to lag the q axis by $\pi/2$.

$$I = \left(i_{q'} - ji_{d'}\right)e^{j\theta} - Ve^{j\theta} \Big/ jX_{eq}$$
$$Q = V\left(E_q'' - V\right) \Big/ X_{eq} \tag{2.1}$$

Note the current injection I is expressed in the network synchronous reference frame. $i_{d'}$ and $i_{q'}$ are the real and reactive current generation from the DFIG in the dq reference frame. $E_q^{"}$ is an equivalent voltage that controls the reactive current generation. X_{eq} is the equivalent Norton reactance and $Ve^{j\theta}$ is the complex terminal voltage.

2.1.2. Reactive Power/Voltage Control Model

The VAR controller model is shown in Figure 2.2. It can switch between power factor control and voltage control scheme. With power factor control, the reactive power command (Q_{cmd}) is calculated based on real power output and a constant power factor. In the voltage control scheme, the command is generated from the supervisory voltage controller to regulate the voltage of a specific bus.

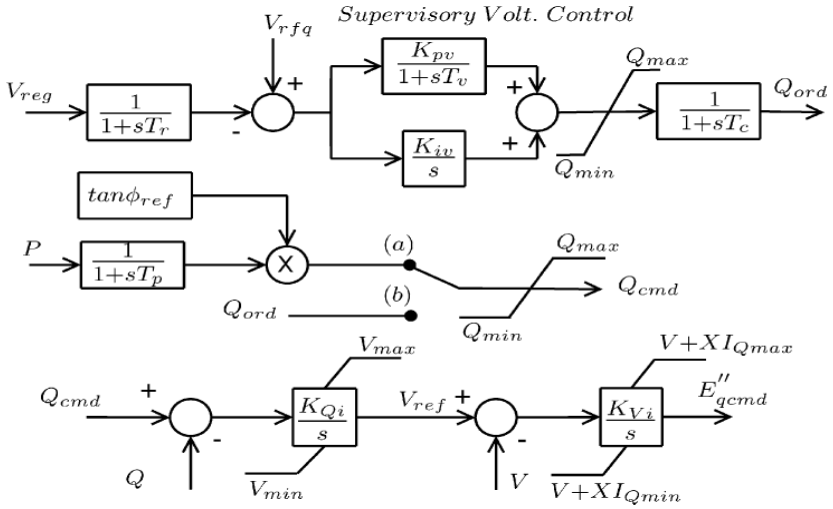

Figure 2.2 VAR controller model: Reprinted with permission from [© 2017, IEEE]

2.2. Damping Torque Analysis for the VAR Controller Mode

To investigate the VAR controller oscillation mode, a single DFIG infinite bus (SDIB) system is set up as shown in Figure 2.3. The DFIG generator used is an aggregation model of 128 General Electric 1.5MW Type 3 wind turbines and has a total capacity of 213.4 MVA and a rated real power generation of 192 MW. The same typical dynamic data as is listed in [30] is used in the study. The collector system and the transformers are also modeled. All the voltages and impedances used in the analysis are labeled in Figure 2.3. V_{reg} is the voltage magnitude at bus 4.

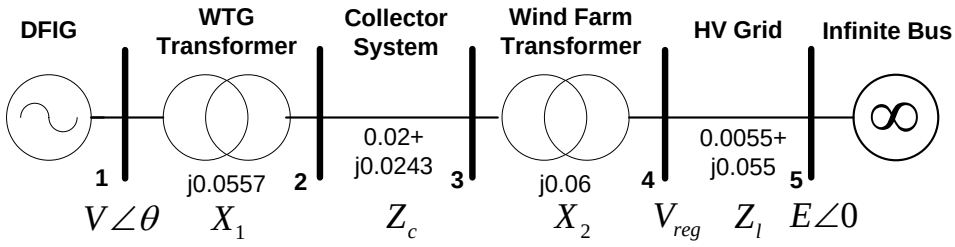

Figure 2.3 Single DFIG infinite bus system: Reprinted with permission from [© 2017, IEEE]

A MATLAB program is written to calculate the initial conditions, linearize the algebraic equations, derive the system state matrix and calculate the eigenvalues. The dynamic equations for the DFIG and its controls are derived from the block diagrams. The calculation indicates that besides the VAR controller mode, the shaft mode is also in the frequency range of electromechanical oscillations (0.1 to 2Hz). The results are consistent with those presented in [30]. For the rest of this section, stability of the VAR controller mode is analyzed with different control schemes.

2.2.1. Power Factor Control Scheme

As shown in Figure 2.2, in power factor control scheme, the supervisory control block is not active. Two assumptions are made here: 1) The wind speed stays constant and the dynamics in the real power control loop are ignored; and 2) The time delay block (with time constant $T_{con} = 0.02$s) in the generator/converter model is ignored to simplify the analysis. Since decoupled PQ control is used in DFIG, the dynamic interaction between the real and reactive power control loops is very limited, thus assumption 1) causes little error. By assumption 1), the real power output from the DFIG stays constant. Since power factor is also constant, the change in reactive power command ΔQ_{cmd} is zero. Thus the reactive power control loop can be simplified to the block diagram in Fig. 4, where K_1 and K_2 are sensitivity indices defined as in (2.2).

$$K_1 = \frac{\Delta V}{\Delta E_q''}$$
$$K_2 = \frac{\Delta Q}{\Delta E_q''} \tag{2.2}$$

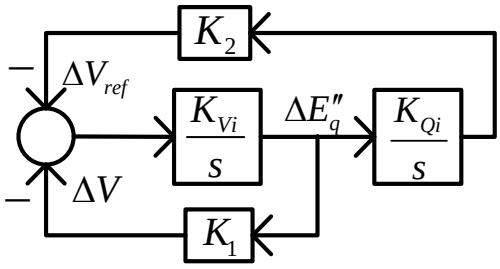

Figure 2.4 Block diagram for the VAR controller mode in power factor control scheme: Reprinted with permission from [© 2017, IEEE]

The network equation for the SDIB system is

$$Ve^{j\theta} = E + I\left(R_{tot} + jX_{tot}\right) \tag{2.3}$$

where R_{tot} and X_{tot} are the total network resistance and reactance.

After linearizing (2.1) and (2.3) and some algebraic manipulations, K_1 and K_2 can be derived as

$$\begin{aligned} K_1 &= \frac{\Delta V}{\Delta E_q''} = \frac{R_{tot}\tan\left(\theta\right) + X_{tot}}{R_{tot}\tan\left(\theta\right) + X_{tot} + X_{eq}} \\ K_2 &= \frac{\Delta Q}{\Delta E_q''} = \frac{\left(E_{q0}'' - 2V_0\right)K_1 + V_0}{X_{eq}} \end{aligned} \tag{2.4}$$

Subscript 0 denotes initial condition. Based on Figure 2.4, eigenvalue for the VAR controller mode can be calculated by solving (2.5)

$$s^2 + K_{Vi}K_1 s + K_{Vi}K_{Qi}K_2 = 0 \tag{2.5}$$

Analogous to the damping torque analysis for the electromechanical mode in SGs, the damping and synchronizing torques T_d and T_s for the VAR controller mode can be defined as

$$\begin{aligned} T_d &= K_{Vi}K_1 \\ T_s &= K_{Vi}K_{Qi}K_2 \end{aligned} \tag{2.6}$$

For this mode to be stable, both T_d and T_s should be positive. Several observations can be made here:

1) K_1 is between 0 to 1 and K_{Vi} is positive, thus T_d is always positive. Sign of K_2 depends on the initial conditions and K_1. With a wide range of system conditions tested, K_2

stays positive. Thus the VAR controller mode in this control scheme stays stable in the SDIB system. Also, its damping and frequency depends highly on K_{Vi} and K_{Qi}.

2) K_1 increases when total impedance or generation amount increases. Thus the power factor control scheme renders a more stable VAR controller mode in weak grids and heavily loaded situations. However, since the terminal voltage is not regulated, it may deviates from the acceptable range.
3) From the equation for K_1, the influence of real power generation amount on this mode's damping is much less compared to impedance change, since the total resistance is much less than the total reactance.

The above observations match the eigenvalue plot in Figure 2.5 with the high voltage (HV) grid impedance changing from 10% to 200% of the base case value and real power generation changing from 10% to 100%. Note that no assumptions are made in the eigenvalue calculations. Also, the shaft mode changes very little (plots omitted) when the operating point changes, which verifies its decoupling from the grid.

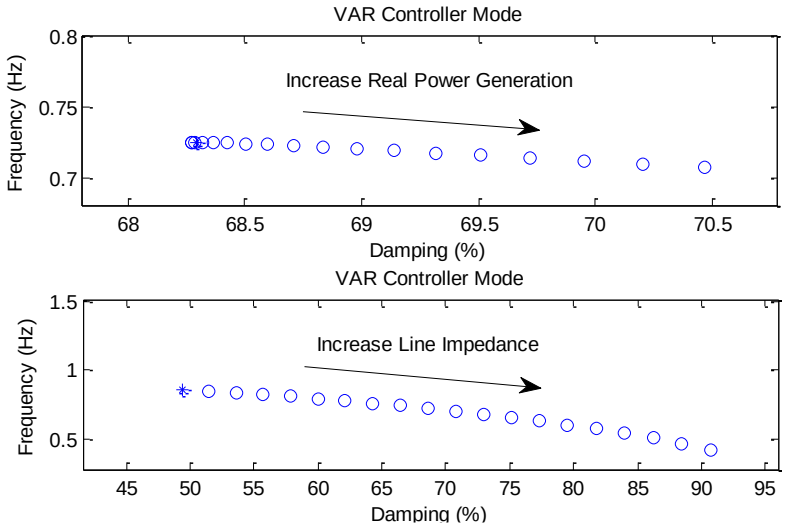

Figure 2.5 VAR controller mode change in power factor control scheme: Reprinted with permission from [© 2017, IEEE]

2.2.2. Voltage Control Scheme

Voltage control scheme is considered in this subsection where the voltage after the wind farm transformer (bus 4) is controlled. The supervisory voltage control block is involved and its transfer function $W(s)$ is added in the VAR controller diagram as shown in Figure 2.6.

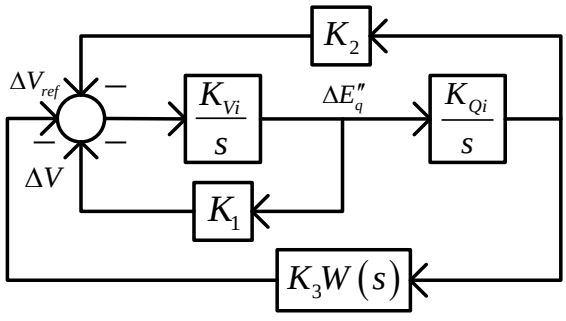

Figure 2.6 Block diagram for the VAR controller mode in voltage control scheme: Reprinted with permission from [© 2017, IEEE]

Since the time constants T_r and T_v are much smaller than T_c (based on values in [31]), the low-pass filter with T_r and T_v are ignored to simplify $W(s)$.

$$W(s) = \frac{\Delta Q_{cmd}}{\Delta V_{reg}}(s) = \left(K_{pv} + \frac{K_{iv}}{s} \right) \times \frac{1}{1 + sT_c} \tag{2.7}$$

K_1 and K_2 have the same expression as in (2.2) and K_3 can be approximated as follows

$$K_3 = \frac{\Delta V_{reg}}{\Delta E''_q} \doteq \frac{X_l}{X_{tot}} K_1 = \frac{X_l}{X_{tot}} \times \frac{R_{tot} \tan(\theta_0) + X_{tot}}{R_{tot} \tan(\theta_0) + X_{tot} + X_{eq}} \tag{2.8}$$

where X_l is the reactance of the HV grid.

Since bus 4 is downstream of bus 1, K_3 is less than K_1. The damping and synchronizing torque in this case can be found as in (2.9), where ω is the modal frequency of the VAR controller mode.

$$\begin{aligned} T_s &= K_{Vi} K_{Qi} K_2 + K_{Vi} K_{Qi} K_3 \, real\left(W(j\omega)\right) = K_{Vi} K_{Qi} \left(K_2 + K_3 \frac{K_{pv} - K_{iv} T_c}{1 + \omega^2 T_c^2} \right) \\ T_d &= K_{Vi} K_1 + \frac{K_{Vi} K_{Qi} K_3 \, imag\left(W(j\omega)\right)}{\omega} = K_{Vi} \left(K_1 - K_3 K_{Qi} \frac{K_{iv} + K_{pv} \omega^2 T_c}{\omega^2 \left(1 + \omega^2 T_c^2\right)} \right) \end{aligned} \tag{2.9}$$

Compared with the damping torque expression for the power factor control scheme, a negative term is added. Thus the VAR controller mode in this case is less damped and is more prone to oscillatory instability.

As line impedance or real power generation increases, both K_1 and K_3 increases, how T_d changes depends on the value of K_{Qi}, K_{iv} and K_{pv}. When these parameters are relatively large, T_d is low and T_d decreases with the increase in line impedance or real power generation. This situation thus possesses more threat to the system. This

observation is in line with the ERCOT experience where it is concluded that aggressive voltage control (high controller gains) causes problems in weak grid conditions [32]. The VAR controller eigenvalues in this case are plotted in Figure 2.7 with impedance change (100% to 300%) and real generation change (10% to 100%). It can be seen that damping of the controller mode deteriorates fast with impedance increase and is comparatively less sensitive to real power generation change.

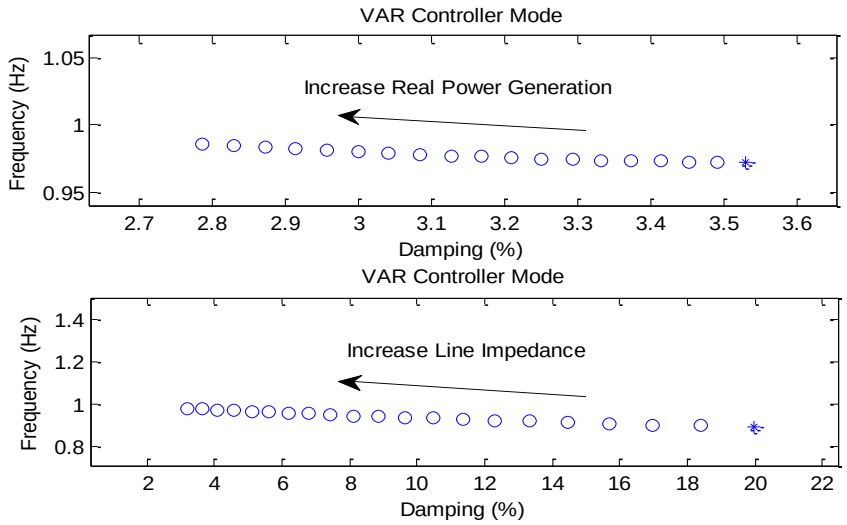

Figure 2.7 VAR controller mode change in voltage control scheme: Reprinted with permission from [© 2017, IEEE]

2.3. Mode Coupling Analysis and the Impact of DFIG Dynamics on Inter-area Oscillations

Coupling between different oscillatory modes in power system has been previously studied [33, 34]. Strong resonance occurs when a system has two equal eigenvalues with a single eigenvector [33]. In practice, a power system will not experience exact strong resonance but two oscillatory modes may approach each other due to

operating condition change or control parameter change and may pass close to a strong resonance [34]. In this case, the mutual participation increases and the eigenvectors of the two modes become similar to each other [33]. It is worth pointing out that through mode coupling, a local oscillatory mode can become coupled with other areas of the system.

In this section the coupling between the VAR controller mode and an inter-area mode is demonstrated in a two-area test system shown in Figure 2.8. It is revealed that through mode coupling, the VAR controller dynamics can have strong influence on inter-area oscillations.

The power flow and dynamic parameters for the SGs are provided in [35]. An aggregated model of 54 General Electric 1.5MW DFIGs is connected to bus 11 close to SG3. It generates 70MW real power (2.5% of total system real power generation). The wind power plant is in voltage control scheme regulating the voltage of bus 104.

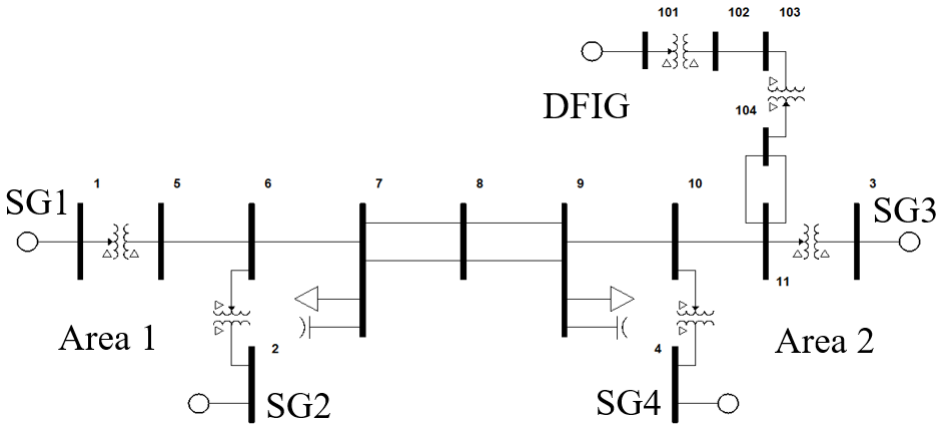

Figure 2.8 Two-area test system: Reprinted with permission from [© 2017, IEEE]

2.3.1. Weak Grid Condition Near the Wind Power Plant

Weak grid conditions for the DFIG plant is first studied by switching off one transmission line between bus 104 and bus 11. As analysed in section 2.2.2, the VAR controller mode can become unstable after line impedance increase. Three sets of control parameters are considered. The VAR controller mode and inter-area mode before and after the line switching are tabulated in Table 2.1 and Table 2.2.

Table 2.1 Critical modes in the system before line switching: Reprinted with permission from [© 2017, IEEE]

		Set 1	Set 2	Set 3
		$K_{Qi} = 0.4$ $K_{Vi} = 4$	$K_{Qi} = 0.64$ $K_{Vi} = 10$	$K_{Qi} = 5$ $K_{Vi} = 80$
IA	Freq.(Hz)	0.6190	0.6295	0.6084
	DR (%)	9.43	7.24	9.74
	WPaf (%)	0.58	16.96	0.33
VC	Freq.(Hz)	0.3047	0.5426	2.5511
	DR (%)	4.77	2.39	11.92
	SPaf (%)	16.06	21.05	0.78

Table 2.2 Critical modes in the system after line switching: Reprinted with permission from [© 2017, IEEE]

		Set 1	Set 2	Set 3
		$K_{Qi} = 0.4$ $K_{Vi} = 4$	$K_{Qi} = 0.64$ $K_{Vi} = 10$	$K_{Qi} = 5$ $K_{Vi} = 80$
IA	Freq.(Hz)	0.6186	0.6133	0.6108
	DR (%)	9.45	6.49	9.6
	WPaf (%)	0.60	20.46	0
VC	Freq.(Hz)	0.3417	0.6126	2.4199
	DR (%)	0.12	-1.2	-0.66
	SPaf (%)	6.31	24.83	0.31

In the tables, IA and VC stand for the inter-area and the VAR controller mode. DR denotes damping ratio. The participation of DFIG state variables in the inter-area mode is measured through WPaf which is defined for mode i as

$$WPaf = \frac{\sum_{DFIG} paf_{ki}}{\sum_{ALL} paf_{ki}} \tag{2.10}$$

where $paf_{ki}$is the participation factor of state k in mode i. The participation of SGs in the VAR controller mode is similarly defined as SPaf.

The inter-area mode ignoring the DFIG dynamics is listed in Table 2.3. This is obtained by modelling the wind power plant as a static power source. All the eigenvalues as well as the participation factors and mode shape information are obtained using Small-signal Security Assessment Tool (SSAT).

Table 2.3 Inter-area mode (DFIG modelled as static power source): Reprinted with permission from [© 2017, IEEE]

	Before Switching		After Switching	
Inter-area mode	Freq. (Hz)	DR (%)	Freq. (Hz)	DR (%)
	0.6189	9.62	0.6185	9.64

Several observations can be made comparing the results in Table 2.1, Table 2.2 and Table 2.3:

1) Before the switching, the VAR controller mode is stable with all 3 sets of parameters. After switching off the line, damping of the VAR controller mode decreases and become marginally stable or even unstable. This is consistent with the previous analysis in section 2.2.2 and the real life ERCOT event.

2) It is clear that when the frequencies of the two modes are close to each other (parameter set 2), the coupling between the two modes increases dramatically. Large mutual participation is evident in this case. Also, damping of the inter-area mode is noticeably influenced by the coupling (compared to the static power model results in Table 2.3).
3) The further away the frequencies separate for the two modes, the lesser mutual participation is observed and the lesser influence wind dynamics have on the inter-area mode and the more accurate to model the DFIG as static power source.

The mode shapes of the two oscillatory modes are plotted in Figure 2.9 for the case after switching. $\emptyset_{KQi}$ and $\emptyset_{KVi}$ denote the VAR controller state variables. The observability of the VAR controller mode in the SG rotor speeds increases when the frequencies of the two modes become closer. And the same is true for the inter-area mode. Interestingly, as the two modes approach each other, the VAR controller mode shape changes a lot, but not the inter-area mode. The two mode shapes become very similar when their frequencies are close to each other, indicating it is near a strong resonance. Notice with parameter set 1 and 3, observability of the VAR controller mode in the SG rotor speeds is low and the SG rotor speeds are almost in phase and thus the VAR controller mode causes local oscillations. Whereas with parameter set 2, its observability increases dramatically in the SG rotor speeds and the SG rotor speeds oscillate out of phase, thus it becomes an inter-area mode. This implies that the ERCORT event in [32] may have caused detrimental inter-area oscillations instead of local oscillations if frequency of the VAR controller mode is close to the inter-area mode, even though the inter-area mode itself has sufficient damping.

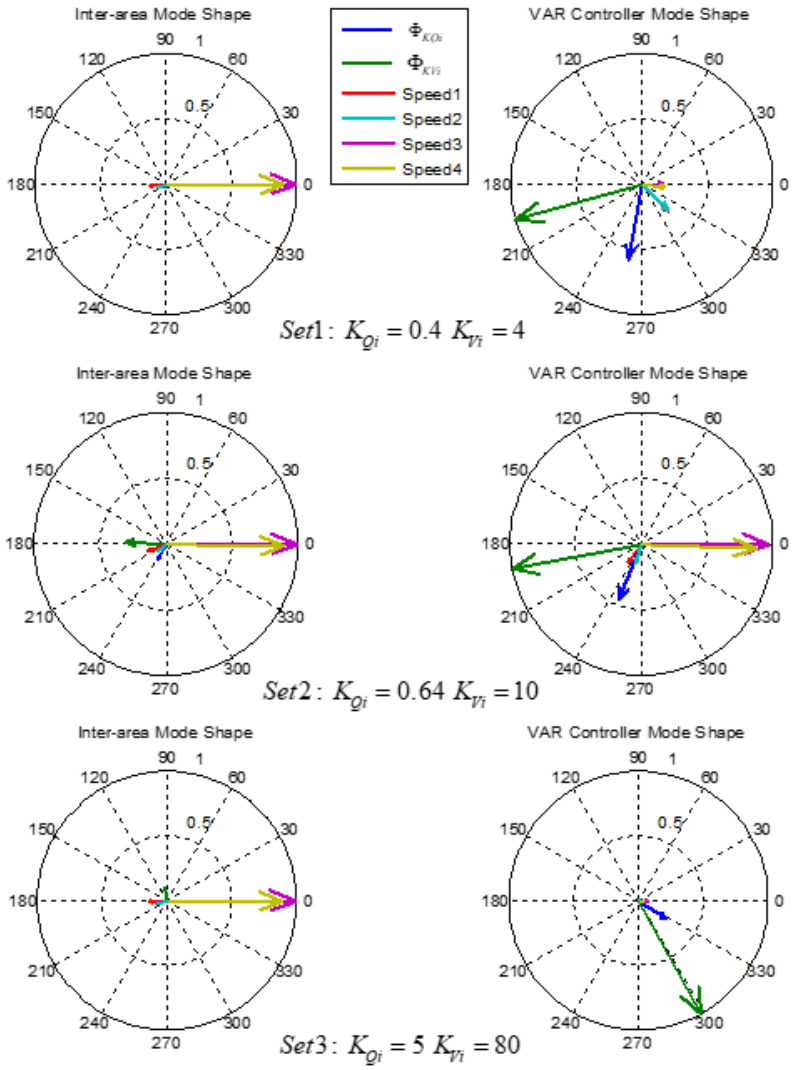

Figure 2.9 Mode shapes with different controller parameters: Reprinted with permission from [© 2017, IEEE]

2.3.2. Strong Grid Condition Near the Wind Power Plant

In this part we consider strong grid condition for the DFIG plant by reducing the impedance to half for both of the lines connecting bus 104 and bus 11. We also reduce the PSS gain of the SGs to simulate a weaker inter-area mode. Four sets of VAR controller parameters are considered. The VAR controller mode and the inter-area mode are

tabulated in Table 2.4. The inter-area mode ignoring the DFIG dynamics has a frequency of 0.5786 Hz with damping 3.77%.

Table 2.4 Critical modes in strong grid condition: Reprinted with permission from [© 2017, IEEE]

		Set 1	Set 2	Set 3	Set 3
		$K_{Qi} = 0.4$ $K_{Vi} = 4$	$K_{Qi} = 0.75$ $K_{Vi} = 10$	$K_{Qi} = 0.7$ $K_{Vi} = 14$	$K_{Qi} = 5$ $K_{Vi} = 80$
IA	Freq.(Hz)	0.5787	0.5949	0.5641	0.5746
	DR (%)	3.70	1.13	5.65	4.20
	WPaf (%)	0.51	38.51	19.95	0.39
VC	Freq.(Hz)	0.2839	0.5417	0.634	2.9465
	DR (%)	5.61	3.87	3.3	15.4
	SPaf (%)	9.42	43.49	25.62	1.28

For all the parameter sets considered here, the VAR controller mode is stable. With parameter set 1 and 4, the frequencies of the two modes are well separated and the mutual coupling is very weak, thus DFIG has negligible impact on damping of the inter-area mode. However, with parameter set 2 and 3, the frequencies of the two modes are close to each other and the coupling between them is strong. DFIG dynamics in this case can either cause the inter-area mode to become unacceptable (set 2) or increase its damping (set 3). The results indicate that when the VAR controller mode is stable and is coupled with the inter-area mode, it has the chance to reduce the damping of the inter-area mode. On the other hand, it also has the potential to increase the inter-area mode damping given proper control parameters.

2.4. Summary

In this section, the DFIG VAR controller mode is analytically studied using damping torque analysis. It is shown that the VAR controller mode is sensitive to system operating conditions close to the wind generator. The voltage control scheme is shown to be more prone to instability than the reactive power control mode. Damping and frequency of the mode vary with different operating conditions.

Coupling between the VAR controller mode and the inter-area mode is then demonstrated in a two-area test system. When frequency of the VAR controller mode approaches the inter-area mode, the followings are observed: 1) mutual participation of the two modes increases; 2) the influence of DFIG dynamics on the inter-area mode damping increases; 3) mode shape of the VAR controller mode changes to involve inter-area oscillation of the SGs. When the coupling is strong, unstable inter-area oscillations can be caused by two mechanisms: 1) a stable VAR controller mode contributes negative damping to the inter-area mode 2) the VAR controller mode becomes unstable and couples with a sufficiently damped inter-area mode (change in VAR controller mode shape) and cause inter-area oscillations. Both situations can be severely detrimental to the system and should be carefully studied to avoid them.

Results in this work can be generalized to other types of CBGs since they have similar VAR controller structures (based on models in PSS/E). Thus the potential coupling between the VAR controller mode and the inter-area mode is generic for CBGs. When setting the CBG controller parameters, this potential mode coupling should be checked over the entire operating range of the CBG plant considering potential topology change

near the CBG plant. It is observed from our research that the CBG mode frequency is sensitive to its operating conditions whereas the inter-area mode is not. This is because the inter-area mode involves large SG inertia from different areas and its frequency is mainly determined by the total amount of inertia involved. Therefore to check for mode coupling, the CBG mode can be evaluated in the SMIB system (shown in Figure 2.3) first to identify the scenarios where the CBG mode has a frequency close to the inter-area mode. Only these scenarios need to be further assessed based on dynamic equations of the whole system. This approach expedites the analysis significantly. If mode coupling is identified and it causes adverse impact on the inter-area mode damping, the control parameters of CBG should be better tuned to avoid the negative impact.

3. TRANSIENT STABILITY ANALYSIS AND STABILITY MARGIN EVALUATION OF CONVERTER-BASED GENERATORS*

3.1. Introduction

As the integration of CBGs continuously grows in power system grids, they are required by various grid codes to provide grid support services such as voltage control and low voltage ride through (LVRT). To meet these requirements and to achieve reliable operation of the grid, maintaining stability of the CBGs under both normal and abnormal grid conditions is becoming increasingly critical.

Operational challenges and instability events of CBGs have been previously identified in the industry, especially in low short-circuit (LSC) systems (aka weak grids). For example, the Electric Reliability Council of Texas (ERCOT) has identified voltage control of wind generators in LSC areas as one of its system operational challenges [32]. Voltage and power oscillations close to a wind power plant were observed in ERCOT, following the outage of a nearby transmission line (which further reduced the available short circuit current) [32]. Another real-world event was recently analyzed by First Solar, Inc., in which a 550MW utility-scale PV plant experienced power and voltage oscillations in a LSC system during the time of day with high real power generation [36]. The converter control parameters were subsequently re-tuned to mitigate the oscillations.

Since CBGs have controls and dynamics that differ from traditional synchronous generators (SGs), the causes and reasons of instability are different and thus, further understanding is required. Presently, vector control is employed for the majority of CBGs and it relies on a phase locked loop (PLL) to synchronize to the main grid [1]. Stability analysis of PLL-synchronized CBGs is an ongoing research topic. To this end, most previous research efforts have been devoted to the area of small signal stability. For example, it is demonstrated that CBGs can experience small signal instability in normal operating state [37]-[39] and during LVRT [40] in LSC systems.

Transient stability analysis of CBGs, which is the focus of this study, has drawn relatively less attention. As reviewed in section 1.2.2, even though some efforts have been made to analyze the transient stability mechanism of CBGs, a more thorough analysis considering dynamic interaction between PLL and other control loops during and after the fault is still needed.

Furthermore, it is important to identify the CBGs with instability risks in both the planning and the operation stages. Dynamic simulations are often relied upon for this task. Nowadays, positive sequence models for CBGs have been widely used in electro-mechanical transient simulation software for bulk power system dynamic studies. However, there are a few inherent limitations in modeling CBGs in positive sequence [1]. These limitations have a significant impact in representing the behavior of VERs in a LSC system, which make the positive sequence models insufficient to be used in LSC scenarios. It is demonstrated in the next section that positive sequence models for VERs can fail to indicate the instability of VERs in LSC systems.

Since the present electromechanical type models are insufficient in representing the CBG dynamics, especially in LSC conditions, electromagnetic type modeling and simulations are often used to assess the stability of CBG integrated systems, which is very time consuming and not suitable for online environment.

To overcome this difficulty, screening indices based on short circuit ratio (SCR) have been proposed to identify potential instability risks of CBGs [1], [41]. For example, ERCOT has set up a practice where the grid strength in a LSC area of its system is evaluated online by an index known as weighted SCR (WSCR). When necessary, wind generator output is curtailed to ensure that the WSCR is above a pre-determined threshold [42].

However, even though lower system strength typically increases the likelihood of stability issues for CBGs, the SCR based method can only be used as a high level screening tool for two reasons [1]. First of all, besides system strength, other factors such as system operating conditions and control parameters also affect the stability of CBGs significantly. Therefore, system strength alone is insufficient in assessing CBG stability accurately. Secondly, different types of instability issues (e.g. transient instability, small signal instability, etc.) may be encountered by CBGs in LSC systems, where each type of instability requires an appropriate evaluation method accounting for the specific instability mechanism. The SCR based method is not detailed enough to indicate the form of instability or to provide information on the stability margin of a certain type of stability.

Therefore, a method tailored specifically to evaluate the transient stability of CBGs and to quantify its stability margin considering the influence of operating conditions and control parameters is highly desired as a supplement to traditional SCR based methods.

The main contributions of the work presented in this section are:

1) It is demonstrated that the present positive sequence modeling of CBGs is insufficient in representing CBG dynamics in LSC systems.
2) The transient stability mechanism of CBGs is thoroughly investigated considering CBG dynamics during and after the fault. Both the PLL and the converter control dynamics are included in the analysis.
3) Key factors that influence the transient stability of CBGs are identified.
4) Based on the stability mechanism, a transient stability margin index which can be obtained analytically is proposed for the CBGs to evaluate their transient stability and stability margin quantitatively.

3.2. CBG Modeling

In this work, a full converter-based Type 4 wind turbine generator (WTG) is considered and its stability is studied under large disturbances. Since solar generators use the same full converter structure and similar converter control algorithms for the grid side converter, the results are also representative of the response of solar generators.

3.2.1. Type 4 WTG - Detailed Model

The configuration of the detailed WTG model is shown in Figure 3.1. The detailed model is used in electromagnetic transient simulation software. In this work, the detailed model is developed in the PSCAD® environment. The main controls of the WTG include

pitch control, machine side converter (MSC) control, grid side converter (GSC) control and the chopper control for DC link overvoltage protection. Vector control is applied to both the MSC and GSC control. The goal of the MSC controller is to achieve maximum power point tracking (MPPT) and the goal of the GSC controller is to maintain the DC link voltage by regulating the real current output I_d and to regulate the terminal bus voltage by regulating the reactive current output I_q. The grid-side converter controls are shown in detail in Figure 3.1 together with the PLL, as they are most relevant to the stability phenomenon discussed subsequently.

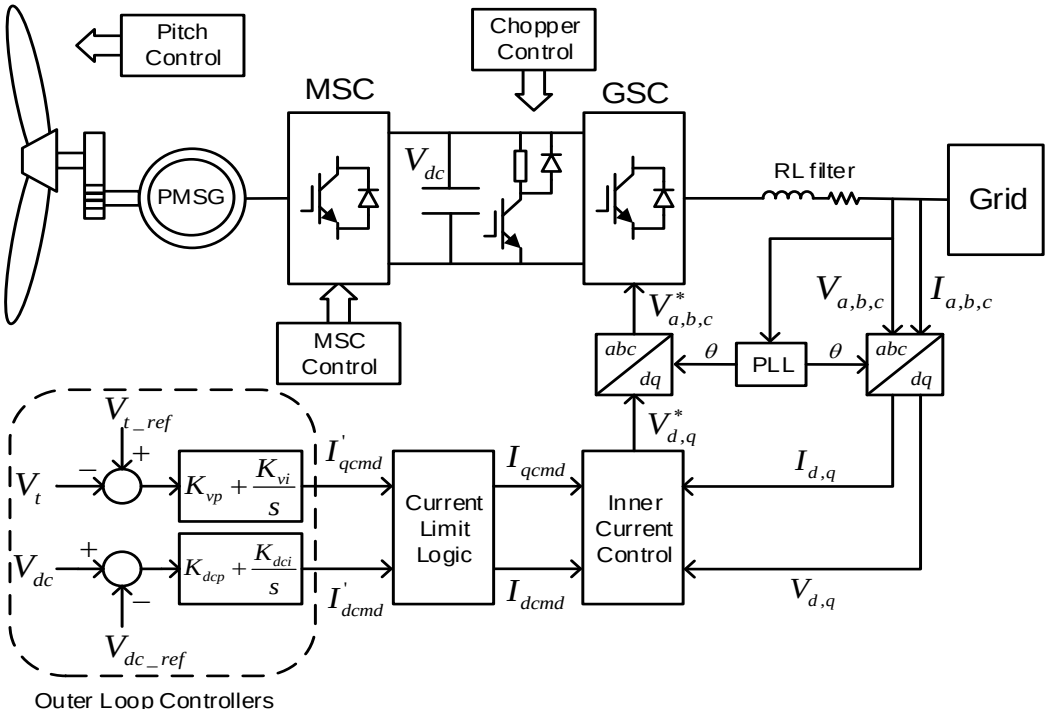

Figure 3.1 Detailed Type 4 WTG model and GSC control algorithm

3.2.2. Type 4 WTG - Generic Positive Sequence Model

The structure of the 2nd generation generic Type 4 WTG model available in most positive sequence stability software (e.g. PSS®E, GE-PSLF™, etc) is shown in Figure 3.2 [43]. The converter control logic is modeled in the REEC model and it generates the real/reactive current injection reference signals. The REGC model contains simplified generator/converter dynamics and it injects current into the grid following the reference signals. The entire Type 4 WTG is modeled as a controlled current source.

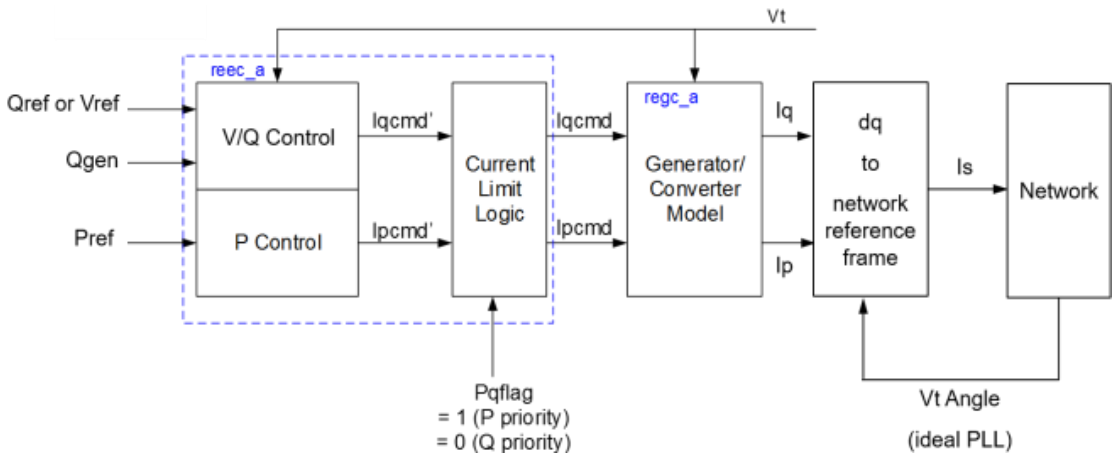

Figure 3.2 Type 4 WTG positive sequence model: Reprinted with permission from [© 2018, IEEE]

The main simplifications of this model, when compared to the detailed model, are listed below:

- The PLL dynamics are ignored. Since positive sequence simulation is a phasor based simulation framework, the terminal voltage phase angle is directly available to the controller without any need of the PLL. Therefore, PLL dynamics get completely ignored in positive sequence models for simplification.

- Dynamics of the inner current control loop are approximated by a first order time delay of 10 to 20 ms.
- The real power control loop is largely simplified ignoring pitch control, machine side converter control and the maximum power point tracking control.
- The dynamics of the PMSG are ignored.
- The capacitor (DC bus) voltage control and dynamics are ignored.

3.3. Description of the System Studied

The system studied is a part of the American Electric Power (AEP) utility's system with several hypothetical renewable energy resources. Both detailed and positive sequence models are used in the simulation study with their responses compared. The portion of the AEP system consists 119 buses, 3 equivalent sources (representing external system outside the studied area) and 9 Type 4 WTGs operating in voltage control mode with reactive power priority during LVRT. The same control parameters are used for all the WTGs. The system topology and the WTG locations are shown in Figure 3.3.

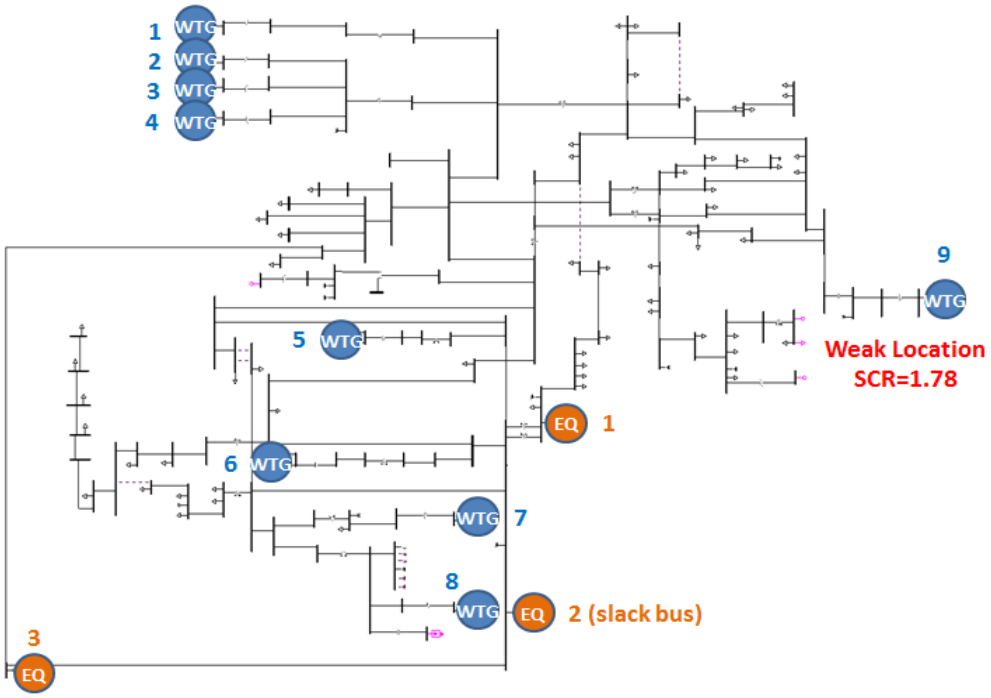

Figure 3.3 Configuration of portion of the AEP System: Reprinted with permission from [© 2018, IEEE]

Short circuit ratio (SCR) is used to quantify the strength of the electric power system at the point of common coupling (PCC) of an energy source, with respect to the size of the energy source. SCR is defined as the ratio of the interconnected grid's short circuit MVA to the MW rating of the interconnecting generator, as shown in (3.1).

$$SCR = \frac{S_{MIN}}{P_{WTG}} \tag{3.1}$$

where S_{min} is the minimum fault level at the PCC without the wind power plant itself (MVA), and P_{WTG} is the MW rating of the WTG. To identify the low and high short circuit locations in the AEP system, the SCR at each WTG PCC bus is calculated and listed in Table 3.1, along with the MVA capacity and the power generation of the WTGs. The WTGs are listed with descending SCR order.

Table 3.1 SCRs at different WTG locations: Reprinted with permission from [© 2018, IEEE]

WTG No.	MVA	PGen (MW)	QGen (MVar)	SCR
2	8.40	7.50	-0.41	12.40
3	25.20	22.50	-3.22	7.20
4	25.20	22.40	-4.20	7.19
5	125.00	66.00	-42.35	4.35
6	117.00	69.50	-36.95	4.29
7	166.50	135.00	-4.20	3.01
8	166.50	135.00	8.64	2.93
1	193.98	157.00	11.37	2.90
9	66.50	50.00	-0.66	1.78

3.4. Limitations of the Positive Sequence CBG Models

To study the transient behavior of the Type 4 WTGs, symmetrical grid faults were applied at the PCC of different WTGs in the AEP system. The solid three phase fault is applied at $t = 0.1s$ and is cleared at $t = 0.2s$ for a fault duration of 6 cycles. The fault is cleared without tripping any lines. WTGs with different SCRs are chosen to study the effect of grid strength on the WTG stability and on the effectiveness of positive sequence modeling.

Heuristically, a location in the system is considered to be a LSC location if its SCR is below 3. Here the simulation results for faults at WTG 6 and WTG 9 are presented. The former is connected to a high short-circuit (HSC) location where SCR equals 4.29, while the latter to a LSC location where SCR equals only 1.78.

The dynamic response of the WTGs during and after the symmetrical grid fault is simulated with both the positive sequence simulation software PSS®E and the electromagnetic transient simulation software PSCAD®, and the results are compared between the two platforms. Note that PSS®E and PSCAD® are representative software platforms used in this study, the purpose of which is to compare positive sequence modeling vs detailed modeling (used as benchmark) in general, irrespective of specific commercial platforms.

3.4.1. WTG Response for Fault at a HSC Location

In the first scenario, a solid three phase fault is applied at the PCC of WTG 6, whose SCR equals 4.29 and represents a HSC location. The real/reactive power outputs and the terminal voltages of WTG 6 and WTG 9 are shown in Figure 3.4. All the quantities are in RMS values. Both WTGs are able to remain stable after the fault is cleared. Thus, this particular fault at the HSC location does not cause instability of the WTGs. Additionally, the results obtained from the positive sequence model and the detailed model are fairly consistent. The largest difference is in the real power response because the temporarily high real power output to discharge the DC link capacitor does not show up in the positive sequence simulation due to the modelling absence of the capacitor dynamics. Overall, the positive sequence model shows a satisfactory response when the fault is at the HSC location.

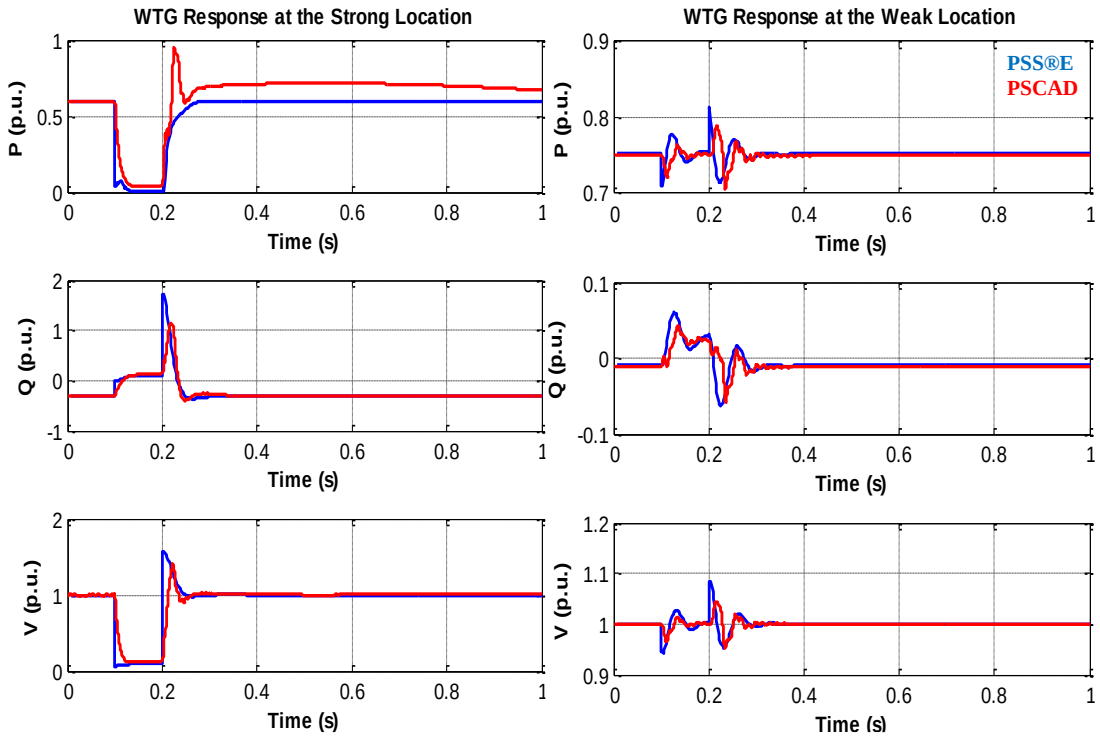

Figure 3.4 Dynamic response of WTG 6 (left) and WTG 9 (right) for fault at the HSC location: Reprinted with permission from [© 2018, IEEE]

3.4.2. WTG Response for Fault at a LSC Location

In this scenario, a solid three phase fault is applied at the PCC of WTG 9, whose SCR equals 1.78 and represents a LSC location. The real/reactive power outputs and the terminal voltages of WTG 6 and WTG 9 are shown in Figure 3.5. As can be concluded from the PSCAD simulation, the fault causes instability of the WTG 9 (close to the fault) and its power outputs and terminal voltage oscillate with large magnitude which will cause tripping of the WTG. Since no protection is simulated, the oscillation sustains and also propagates to WTG 6 with reduced magnitude.

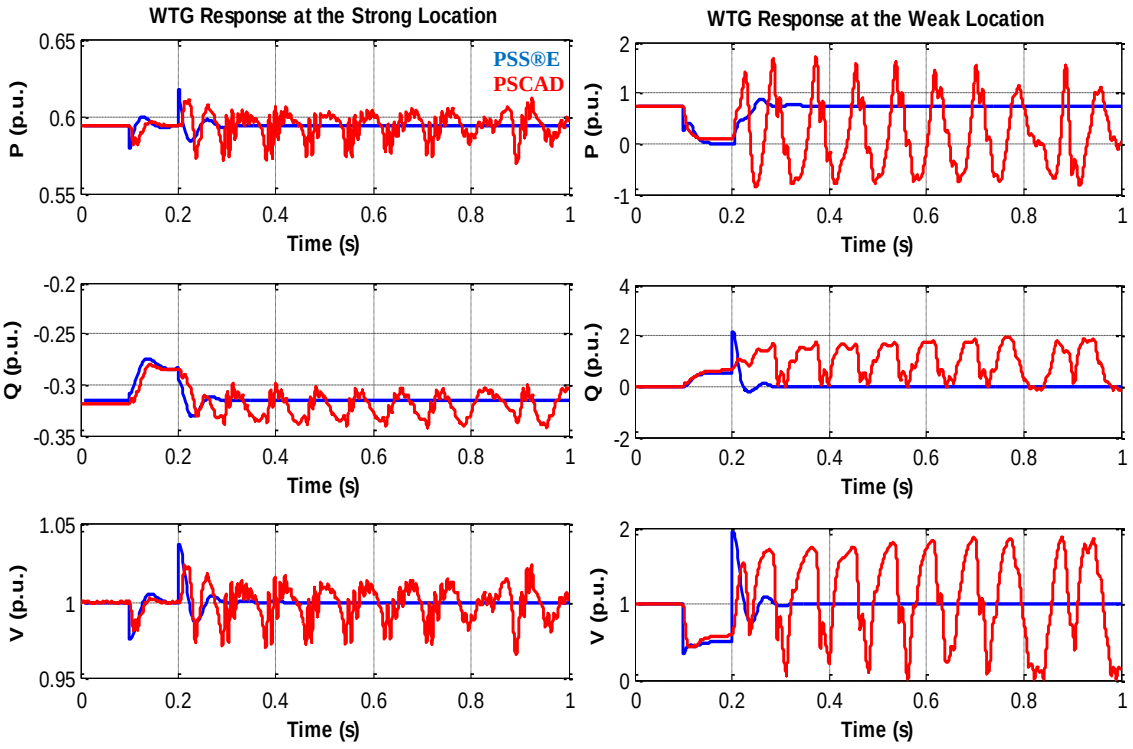

Figure 3.5 Dynamic response of WTG 6 (left) and WTG 9 (right) for fault at the LSC location: Reprinted with permission from [© 2018, IEEE]

It is important to notice that the positive sequence simulation in this case shows that the WTGs remain stable after the fault. Since the positive sequence WTG model ignores the dynamics of the PLL, this instability phenomenon cannot be captured by the positive sequence simulation. This reveals the limitation of using positive sequence WTG models in interconnection studies when the WTG is connected to a LSC point in the system. Therefore, detailed electromagnetic transient simulations should be carried out to study WTG stability in this situation.

3.5. Transient Stability Analysis of CBGs

Simulations in section 3.4 clearly reveal that the CBGs can become transiently unstable after a fault. In this section, the transient stability mechanism of CBGs is investigated in detail.

Toward this goal, a simple system is first considered where one aggregated full converter based WTG is connected to the grid represented by the Thevenin equivalent circuit, as shown in Figure 3.6.

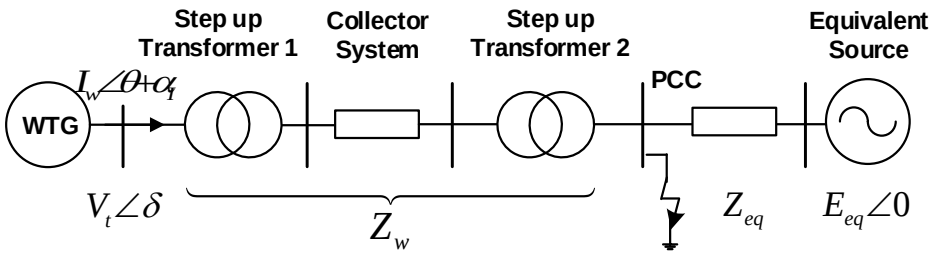

Figure 3.6 Single full converter based WTG connected to the grid

Z_w is the total impedance of the step up transformers and the collector system. Z_{eq} is the equivalent grid impedance at the point of common coupling (PCC) and a higher Z_{eq} indicates a lower SCR at the PCC. The voltages and currents in the system are expressed in phasors and their relationship is shown in Figure 3.7. The equivalent voltage source is assumed to have a constant magnitude E_{eq} and a constant frequency of 60 Hz. Its angle is zero in the synchronous reference frame. V_t and δ are the magnitude and angle of the WTG terminal voltage. The WTG output current has a magnitude of I_w and an angle of

α_I in the dq reference frame. The d axis of the dq reference frame is leading the synchronous frame by angle θ defined by the PLL.

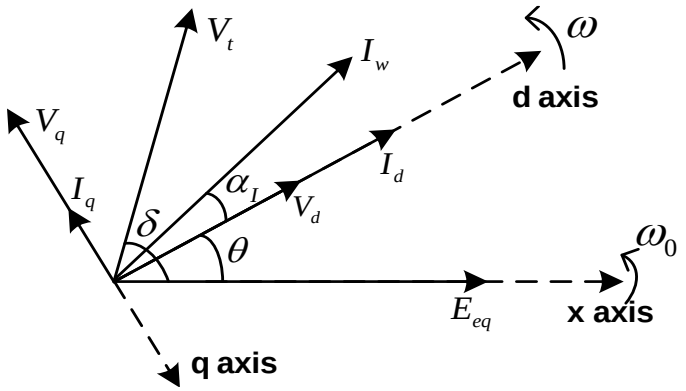

Figure 3.7 Voltage and current phasor diagram

The WTG is regarded as a controlled current source ignoring the inner current control dynamics, since the bandwidth of the inner current control loop is much higher than that of the PLL and the outer loop controllers [44]. By this assumption, the current output of the WTG is the same as the current command ($I_q = I_{qcmd}$, $I_d = I_{dcmd}$ in Figure 3.1). It should be noticed that the frequency of the WTG current output depends on the PLL frequency, which deviates from 60 Hz in the dynamic state. However, throughout this study the reactance in the system is calculated based on the synchronous frequency only. This gives a clearer view of the transient stability mechanism. The introduced error by this assumption in the stability margin evaluation is minimal, as will be shown later on.

3.5.1. PLL Dynamics With and Without a Fault

The control diagram of a generic PLL is shown in Figure 3.8.

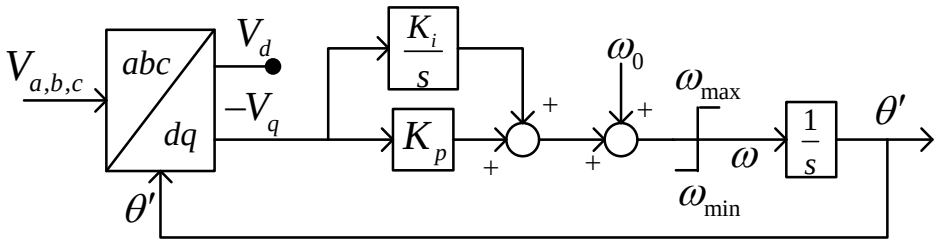

Figure 3.8 Control diagram for the generic PLL

The angle output θ' is with reference to a steady reference frame and is related to θ in Figure 3.7 by (3.2).

$$\theta = (\omega - \omega_0)t = \theta' - \omega_0 t \tag{3.2}$$

The position and the rotation speed of the dq axis are determined by the PLL output θ and ω. In steady state, $\theta = \delta$ and $\omega = \omega_0$ (synchronous frequency) and the d axis is aligned with the terminal voltage vector.

Consider first the system operation in normal operating state. Based on the system configuration and the phasor diagram, the terminal voltage of WTG can be expressed as in (3.3).

$$V_t e^{j\delta} = E_{eq} + (Z_w + Z_{eq}) I_w e^{j(\alpha_I + \theta)} \tag{3.3}$$

Define

$$\begin{aligned} Z &= Z_w + Z_{eq} = R + jX \\ Z_w &= R_w + jX_w \end{aligned} \tag{3.4}$$

Then the q axis terminal voltage V_q can be derived as

$$\begin{aligned} V_t e^{j(\delta-\theta)} &= E_{eq} e^{-j\theta} + (I_d - jI_q)(R + jX) \\ -V_q &= V_t \sin(\delta - \theta) = (I_d X - I_q R) - E_{eq} \sin(\theta) \end{aligned} \tag{3.5}$$

Ignoring the proportional gain K_p and the output frequency limits in the PLL control loop for now, the differential equations of the PLL state variables (θ and ω) are

$$\begin{aligned} \dot{\theta} &= \omega - \omega_0 \\ \frac{1}{K_i}\dot{\omega} &= -V_q = \underbrace{\left(I_d X - I_q R\right)}_{R1} - \underbrace{E_{eq}\sin\theta}_{R2(\theta)} \end{aligned} \tag{3.6}$$

It can be seen that (3.6) is structurally similar to the well-known swing equations of a SG connecting to an infinite bus, where $1/K_i$ is analogous to the machine inertia H, $R1$ to the mechanical power input P_m and $R2(\theta)$ to the electrical power output P_e. It should however be emphasized that the analogy drawn here **does not** imply similarity between WTG and synchronous machine dynamics and stability at all. It is solely based on the similarity between the PLL dynamic equations and the synchronous machine swing equations. Because of this similarity, techniques traditionally used for analyzing the stability of the swing equations (e.g. equal area criterion) can be adapted to analyze the CBG transient stability, as is shown later in this section.

In normal operating stage, the WTG would normally generate more real power than reactive power, thus $I_d > I_q$. Since for the transmission grid normally $X > R$, $R1$ is greater than zero. The greater the real power generation and lower reactive power generation, the larger the value of $R1$.

Now consider the case where a solid three phase to ground fault occurs at the PCC of the WTG. During the fault $R2(\theta)$ becomes zero and the dynamic equations of the PLL become

$$\dot{\theta} = \omega - \omega_0$$
$$\frac{1}{K_i}\dot{\omega} = \underbrace{I_d X_w - I_q R_w}_{R3} \tag{3.7}$$

During the fault, it is assumed that the GSC control works in Q priority mode which gives priority to reactive power injection to support grid voltage while limiting the real power injection. The real and reactive currents (I_d, I_q) are limited as in (3.8).

$$\begin{aligned} \left|I_q\right| &\le I_{q\,max} \\ \left|I_d\right| &\le \sqrt{I_{max}^2 - I_q^2} \end{aligned} \tag{3.8}$$

where I_{qmax} and I_{max} are maximum allowed reactive current and total current, respectively, and are constants. Since the fault is close to the WTG, it is reasonable to assume that I_q and I_d hit their respective limits with the attempt to increase the terminal voltage and to maintain the DC link voltage, respectively. I_d is smaller than I_q since I_{qmax} is close to I_{max} in Q priority mode. Again $X_w > R_w$, so $R3$ can be positive, negative or zero depending on the I_q/I_d ratio and the X_w/R_w ratio.

3.5.2. Mechanism of CBG Transient Stability

To analyze the mechanism for CBG transient stability and to gain engineering insights on the influencing factors, it is first assumed that $R1$ and $R3$ are constant. This assumption ignores transients in I_d and I_q following the occurrence and clearance of the fault, i.e. the dynamics from the outer loop controllers. The dq currents are assumed to be at their limits during the fault and at the steady state values before and after the fault. This assumption will be relaxed later on in section 3.6 to improve the accuracy of transient stability margin evaluation.

As illustrated in Figure 3.9, the equal area criterion can be adapted to analyze the transient stability of the WTG. The case where $R3$ is positive is chosen to illustrate the analysis in this study while the case where $R3$ is negative can be similarly analyzed.

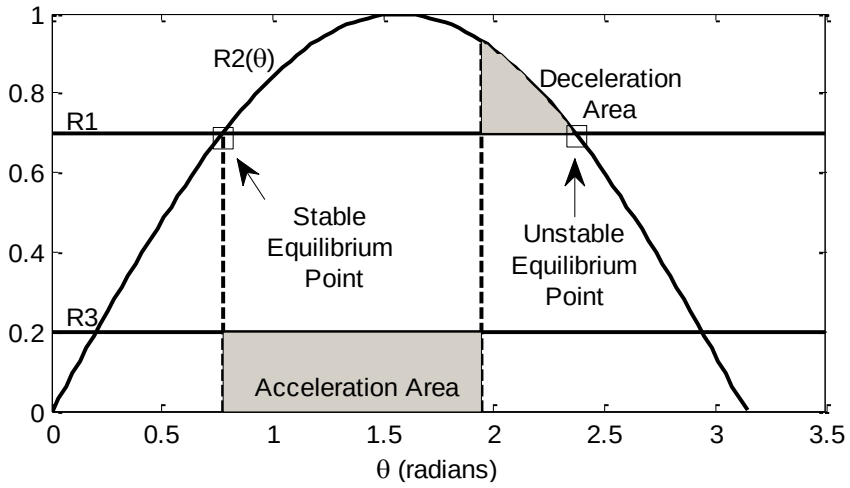

Figure 3.9 Analysis of the PLL stability using equal area criterion

The stable equilibrium point for the normal operating state can be calculated by setting (3.6) equal to zero. The results are shown in (3.9).

$$\theta_s = \arcsin\left(\frac{R1}{E_{eq}}\right) \qquad (3.9)$$
$$\omega_s = \omega_0$$

The unstable equilibrium point can be easily obtained as

$$\theta_u = \pi - \theta_s = \pi - \arcsin\left(\frac{R1}{E_{eq}}\right) \qquad (3.10)$$
$$\omega_u = \omega_0$$

When the fault occurs at the PCC, dynamics of the PLL is determined from (3.7). The frequency and angle output of the PLL continues to increase due to a positive $R3$. Denoting the angle output of PLL at the fault clearing moment as θ_c, the acceleration area can be calculated as

$$A_{acc} = R3\left(\theta_c - \theta_s\right) \tag{3.11}$$

Assuming that the fault is cleared without any line tripping, the stable and unstable equilibrium points stay the same as before the fault. If $\theta_c < \theta_u$, the PLL frequency will start to decrease. The deceleration area can be defined as

$$A_{dec} = \int_{\theta_c}^{\theta_u} \left[R2\left(\theta\right) - R1\right] d\theta \tag{3.12}$$

From the equal areal criterion, the system will return to the stable equilibrium if and only if $A_{dec} > A_{acc}$. Otherwise a "pole slipping" will occur and the PLL frequency will continue to increase even after the fault is cleared. Instability of the PLL and failure to track the grid voltage angle after the fault will cause power and voltage oscillations at the WTG location and will cause the tripping of the WTG eventually.

Based on the above analysis, the factors that affect the transient stability of a CBG can be summarized as follows:

- A weaker grid evaluated at the PCC (larger Z_{eq} and/or lower E_{eq}) has adverse effect on CBG transient stability since it increases $R1$ and/or reduces the peak of $R2(\theta)$ thus reduces the deceleration area.
- A CBG with higher real power generation has a higher value of $R1$ and is more prone to transient instability.

- In normal operating conditions, generating (absorbing) reactive power together with real power generation reduces (increases) $R1$ thus improves (worsens) the transient stability of a CBG.

Similar to increasing the inertia of a synchronous machine, a smaller integral gain (K_i) in the PLL improves the transient stability of a CBG. A smaller value of K_i decreases the tracking speed of the controller. In a LSC system, a slower controller is more stable as the feedback to the controller from the system will be delayed and can have a large phase lag. To compensate for this delay, the controller has to be made slower in order to keep the system stable.

3.6. Transient Stability Margin Evaluation of CBGs

In power system planning and operations, it is important to evaluate and monitor the system's transient stability subjected to a set of plausible transient disturbances. In this section we propose a method to screen the CBGs in the system and evaluate their transient stability margin quantitatively without running dynamic simulations, which renders it especially beneficial for online applications.

3.6.1. Transient Stability Margin Definition

The maximum amount of time which can be tolerated to clear a fault and still maintain system stability is commonly called the critical clearing time (CCT). The CCT when compared to the expected clearing time, indicates the margin of safety between stability and instability. Thus a transient stability margin index was proposed in [45] as

$$S_m = \frac{100\left(t_{cc} - t_e\right)}{t_e} \tag{3.13}$$

where t_{cc} is the CCT and t_e is the expected clearing time which is mainly determined by the protection relay settings.

In this study, we use the same stability margin index to evaluate the transient stability margin for CBGs. The scenario where a solid three phase to ground fault occurs at the PCC of the CBG is considered. From the analysis in section 3.5.2, during the fault the voltage reference from the main grid is lost and no steady state operating point exists. It thus serves as the worst case scenario to analyze the CBG transient stability margin.

Please note that the CBGs that experience stability issues are often located in LSC areas where few synchronous machines exist [1]. Thus they have little dynamic interaction with synchronous machines. In addition, the current output from an electrically far away CBG has little influence on the terminal voltage of a local CBG, and thus has little impact on its PLL dynamics that is coupled through the terminal voltage. Given these two observations, the power grid connected to the PCC of a CBG or a group of electrically close CBGs can be modelled as a Thevenin equivalent circuit with a constant voltage source. Then the reduced system model shown in Figure 3.6 can be used to obtain CCT and S_m for each individual CBG (or a group of electrically close CBGs).

3.6.2. Calculation of CCTs

Following (3.11) and (3.12) the critical clearing angle θ_{cc} can be obtained by setting $A_{acc} = A_{dec}$ as in (3.14).

$$R3\left(\theta_{cc} - \theta_s\right) = \int_{\theta_{cc}}^{\theta_u} E_{eq} \sin\left(\theta\right) d\theta - R1\left(\theta_u - \theta_{cc}\right) \tag{3.14}$$

Subsequently, since $R3$ is a constant during the fault, by double integrating the second equation in (3.7), the CCT t_{cc} can be obtained analytically as in (3.15) by plugging in θ_{cc} calculated from (3.14).

$$\frac{1}{2}K_i R3 \times t_{cc}^2 = \theta_{cc} - \theta_s$$
$$t_{cc} = \sqrt{\frac{2(\theta_{cc} - \theta_s)}{K_i R3}} \tag{3.15}$$

3.6.3. Consideration of Outer Loop Controller Dynamics

Equation (3.14) and (3.15) shows a simple way to obtain the CCT analytically. However, it follows directly from the analysis in section 3.6.1 where the dynamics of the outer loop voltage controllers are ignored. To illustrate the effect of this simplification, typical dq current response of a CBG during and after a fault is shown in Figure 3.10 (a) and (b). The blue curve is the response from an electromagnetic simulation with detailed converter model, while the red curve shows the dq current response without the outer loop controller dynamics. The fault occurs at $t = 0$ and is cleared at $t = t_c$.

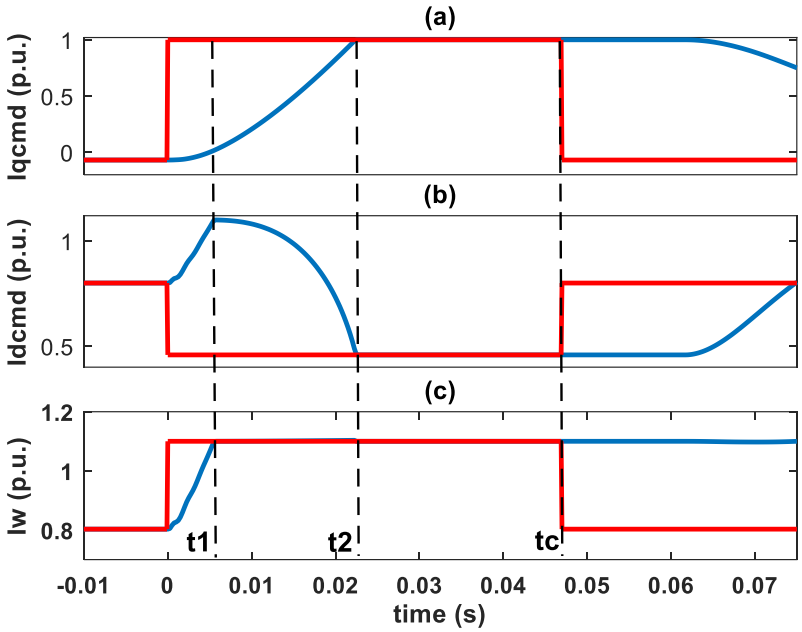

Figure 3.10 Typical dq current response and total current magnitude following a fault. (blue curve: response from detailed model; red curve: response without outer loop controller dynamics)

As shown by the blue curve, following occurrence of the fault, I_{qcmd} increases due to the reduced terminal voltage and it reaches the limit at t_2. Meanwhile, I_{dcmd} first increases until it reaches the limit at t_1. Then it follows the limit till t_c. Notice from (3.8) that the limit for I_{dcmd} is a function of I_{qcmd} and is not a constant before t_2. When the current transients are ignored during the fault, as shown by the red curve, I_{dcmd} and I_{qcmd} hit their respective limits at $t = 0$ which deviates from the blue curve significantly and thus will cause huge error in the CCT calculation. Therefore, to assess the CCT more accurately, it is necessary to analytically represent the transient behavior of the dq current response before they hit their respective limits.

Analytical time domain expressions for the inputs of the outer loop controllers (V_t and V_{dc} as shown in Figure 3.1), which depend on the output current magnitude $I_w = \sqrt{I_{dcmd}^2 + I_{qcmd}^2}$ during the fault, would facilitate our aim. In order to express V_t and V_{dc} analytically, it is assumed that I_w reaches I_{max} at $t = 0$ and stays at I_{max} during the fault. I_w with and without this assumption is shown in Figure 3.10 (c) by the red and blue curve, respectively. As can be seen, this assumption is not valid before t_1. However, the error introduced is small since t_1 is very close to 0 and the simplified I_w response is very close to the detailed response during the fault.

Following this assumption and ignoring the electromagnetic transients in the network, the terminal voltage of the CBG has a step change from the normal state value V_0 to the faulted state value V_f at $t = 0$, where V_f is determined as

$$V_f = I_{max} \times |Z_w| \tag{3.16}$$

The measured terminal voltage V_t which is used in the control loop has a first order delay with time constant τ. Thus its time response is

$$V_t(t) = V_f + (V_0 - V_f)e^{-t/\tau} \tag{3.17}$$

With reference to the control logic in Figure 3.1, the time response of I_{qcmd} can be obtained as in (3.18), where I_{q0} is the initial steady state q axis current.

$$I_{qcmd}(t)=\begin{cases} I_{q0}+\left(K_{vp}+K_{vi}\int_0^t dt\right)\left(V_0-V_t(t)\right) & 0\le t<t_2 \\ I_{q\,max} & t_2\le t<t_c \end{cases} \qquad (3.18)$$

t_2 is solved from

$$I_{q0}+\left(K_{vp}+K_{vi}\int_0^t dt\right)\left(V_0-V_t(t)\right)=I_{q\,max}$$

To obtain the time domain equation for I_{dcmd}, the dynamics of the DC link capacitor need to be determined first as in (3.19), where P_{in} denote the real power input to the DC link from the MSC and P_{out} the real power output to the GSC. We assume a constant P_{in} during the study period since the real power control in the MSC is based on MPPT and pitch control which are much slower compared to the GSC and PLL dynamics. P_{out} during the fault can be calculated from (3.20) and the DC link voltage is obtained as in (3.21). Notice that the DC chopper control to increase P_{out} during the fault is not considered in this analysis. The time response of I_{dcmd} is obtained as in (3.22).

$$P_{in}-P_{out}=CV_{dc}(t)\frac{dV_{dc}(t)}{dt} \qquad (3.19)$$

$$P_{out}=I_{max}^2\times R_w \qquad (3.20)$$

$$V_{dc}(t)=\sqrt{\frac{2\left(P_{in}-P_{out}\right)}{C}t+V_{dc\_ref}^2} \qquad (3.21)$$

$$I_{dcmd}(t)=\begin{cases} I_{d0}+\left(K_{dcp}+K_{dci}\int_0^t dt\right)\left(V_{dc}(t)-V_{dc\_ref}\right) & 0\le t<t_1 \\ \sqrt{I_{max}^2-I_{qcmd}^2(t)} & t_1\le t<t_2 \\ \sqrt{I_{max}^2-I_{q\,max}^2} & t_2\le t<t_c \end{cases} \tag{3.22}$$

t_1 is solved from

$$I_{d0}+\left(K_{dcp}+K_{dci}\int_0^t dt\right)\left(V_{dc}(t)-V_{dc\_ref}\right)=\sqrt{I_{max}^2-I_{qcmd}^2(t)}$$

3.6.4. Consideration of Current Dynamics and the Proportional Gain in PLL Control Loop

In the equal area criterion described in section 3.5.2, the acceleration area quantifies the "kinetic energy" gained in the PLL integrator. Note that "kinetic energy" is defined here for the PLL integrator based on the mathematical (not physical) analogy between the PLL dynamic equations and the SG swing equations. During the fault, the PLL proportional gain K_p provides an offset to the PLL frequency, as shown in (3.23)

$$\omega(t)=\underbrace{K_pR3(t)}_{\omega_p(t)}-\underbrace{\int_0^t K_iR3(t)dt}_{\omega_i(t)} \tag{3.23}$$

Since the current dynamics are considered, $R3$ is no longer constant during the fault and is time dependent as in (3.24)

$$R3(t)=I_{dcmd}(t)X_w-I_{qcmd}(t)R_w \tag{3.24}$$

The "kinetic energy" stored in the integrator during the fault can be obtained as

$$E_K(t_c)=\frac{1}{2K_i}\omega_i^2(t_c)=\frac{1}{2K_i}\left[\int_0^{t_c}K_iR3(t)dt\right]^2 \tag{3.25}$$

PLL angle output at $t=t_c$ is

$$\theta_c(t_c) = \theta_s + \int_0^{t_c} \omega(t)\,dt \tag{3.26}$$

With reference to Figure 3.10 (a) and (b), when the fault clears, the terminal voltage of the CBG increases gradually and the dq current outputs stay at their respective limit until the measured terminal voltage reaches the reference value. Thus $R1$ for a short period after the fault clearing is constant as

$$R1 = \sqrt{I_{max}^2 - I_{qmax}^2}\,X - I_{qmax}R \tag{3.27}$$

The deceleration area denotes the maximum amount of incremental potential energy (E_p) that can be gained without losing stability

$$E_p(t_c) = \int_{\theta_c(t_c)}^{\theta_u} E_{eq}\sin(\theta)\,d\theta - R1\left[\theta_u - \theta_c(t_c)\right] \tag{3.28}$$

Since both E_K and E_p are functions of the clearing time, the CCT can be obtained by solving the equation $E_K(t_{cc}) = E_p(t_{cc})$. It should be emphasized that besides the various controller settings, all the information needed for the CCT calculation can be obtained from the power flow solution of the pre-fault system and without any dynamic simulation.

It should be noticed that K_p also provides a time varying offset to the PLL frequency after the fault clearance. This is equivalent to adding frequency dependent damping to the post fault dynamic equations. Ignoring this damping effect will result in a slightly reduced CCT, as will be shown in the demonstrating results.

3.6.5. Consideration of Interactions Among Electrically Close CBGs

When multiple CBGS are electrically close to each other, the dynamic interaction among them is too large to be ignored. Here a case with two electrically close WTGs is

used to illustrate the process to account for their interactions. It can be easily extended to the cases with more than two close by CBGs. The reduced system to calculate the CCT is shown in Figure 3.11. Here the fault is applied at the first bus that couples the two WTGs, which is referred to as the coupling bus. Notice that this reduction is mostly useful when the electrically close CBGs are connected to a distant bus through separate transmission lines, which is common in a transmission system. However, further studies are needed for systems that cannot be reduced to a topology like this.

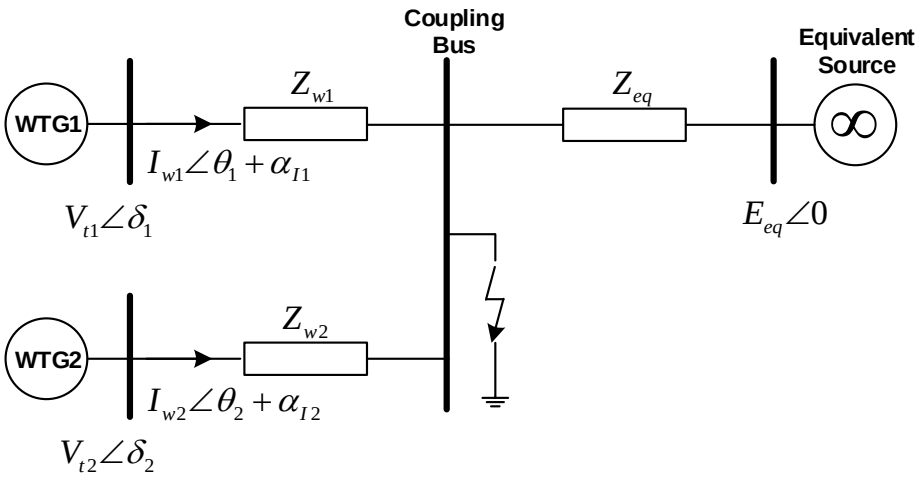

Figure 3.11 Two close by WTGs connected to the grid

Given the reduced system in Figure 3.11, during the solid three phase fault, the two WTGs are decoupled, thus (3.16) to (3.26) can be directly applied to each WTG individually. When the fault is cleared, the two WTGs become coupled since the current output of one WTG will affect the terminal voltage of the other. The terminal voltage of WTG1 is shown as

$$
\begin{aligned}
V_{t1}e^{j(\delta_1-\theta_1)} &= E_{eq}e^{-j\theta_1} + \left(Z_{w1}+Z_{eq}\right)I_{w1}e^{j\alpha_{I1}} + Z_{eq}I_{w2}e^{j\alpha_{I2}}e^{j(\theta_2-\theta_1)} \\
&= E_{eq}e^{-j\theta_1} + \left(Z_{w1}+Z_{eq}+\frac{|I_{w2}|}{|I_{w1}|}Z_{eq}e^{j(\alpha_{I2}-\alpha_{I1})}e^{j(\theta_2-\theta_1)}\right)I_{w1}e^{j\alpha_{I1}}
\end{aligned}
\tag{3.29}
$$

Comparing (3.29) to (3.5) for WTG1, the effect of having WTG2 is to add a coupling impedance to the equation. The complexity of treating this equation comes from the term $e^{j(\theta_2-\theta_1)}$ which is not constant during the transient process after the fault. However, this can be simplified by locking the angle difference between the two PLLs to the value at fault clearing (i.e. $\theta_2(t)-\theta_1(t)=\theta_2(t_c)-\theta_1(t_c)$ for $t>t_c$). Then the effect of having WTG2 on the PLL dynamics of WTG1 after the fault is to modify the Thevenin equivalent impedance by the factor shown as

$$
Z_{eq1} = \left(1+\frac{|I_{w2}|}{|I_{w1}|}e^{j(\alpha_{I2}-\alpha_{I1})}e^{j(\delta_2-\delta_1)}\right)Z_{eq} \tag{3.30}
$$

Then following the same procedure illustrated in (3.27) and (3.28) the CCT can be obtained for WTG1. The CCT for WTG2 can be obtained following a similar process and the smaller CCT between the two is selected to approximate the actual CCT for fault at the coupling bus.

3.7. Demonstrating Results

Electromagnetic dynamic simulations with detailed WTG models were conducted to verify the stability margin index proposed in section 3.6. The system studied is the AEP network introduced in section 3.3.

The detailed WTG model illustrated in Figure 3.1 (including the inner current controller) was developed in the PSCAD® environment. An average value model [46] is

used for the voltage converters, ignoring the high frequency switching dynamics. Notice that the DC chopper control is not modeled so the DC link voltage is allowed to go higher during the fault and the extra energy stored is discharged after the fault.

3.7.1. Base Case Study

As analyzed in section 3.5, the key control loops that affect the transient stability margin of a CBG are the PLL and the GSC outer control loops (terminal voltage control and DC link voltage control). For the base case, the parameters for the key control loops are listed in Table 3.2. The voltage measurement delay τ is assumed to be 0.01s for all the WTGs. The same control parameters are used for each of the 9 WTGs in the system. As shown in Figure 3.12, there are two groups of electrically close WTGs. The first group contains WTG 1 through 4 while the second contains WTG 7 and 8. The dynamic interaction within each group of WTGs are accounted for in the CCT calculation as discussed in section 3.6.5. To obtain the CCT from the PSCAD simulation, a solid three phase fault is applied at the coupling bus (CoB) for group 1 and 2 and at the PCC bus for the rest of the WTGs. The CCT is obtained by gradually increasing the fault clearing time until a "pole slipping" occurs for the PLL angle after the fault.

Table 3.2 Base case control parameters

PLL		Terminal Voltage Control		DC Voltage Control	
K_i	K_p	K_{vi}	K_{vp}	K_{dci}	K_{dcp}
1400	60	120	0	40	10

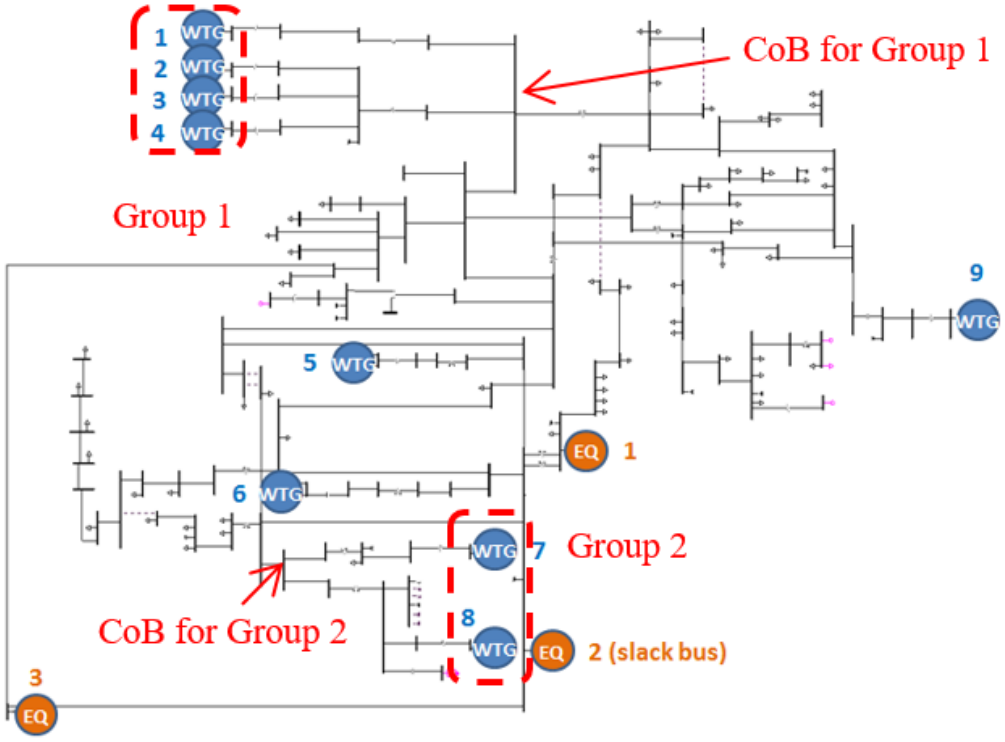

Figure 3.12 Configuration of the AEP System

Following (15) to (27), the calculated CCTs (CCT_C) are compared with the simulated CCTs (CCT_S) in Table 3.3. As can be seen, the error increases slightly when the number of interacting WTGs increases. However, the error is marginal even for the case with four interacting WTGs in group 1.

Table 3.3 CCT and S_m for WTGs in the base case

	CCT_S (s)	CCT_C (s)	Error (%)	S_m_S	S_m_C	WSCR
WTG 9	0.0630	0.0623	-1.11	-37	-37.7	1.78
WTG 5	0.1110	0.1074	-3.24	11	7.4	5.44
WTG 6	0.1135	0.1119	-1.41	13.5	11.9	4.76
Group 2	0.1222	0.1166	-4.58	22.2	16.6	1.65
Group 1	0.1248	0.1176	-5.77	24.8	17.6	1.814

From (3.13) and assuming $t_e = 0.1s$, the calculated and simulated stability margin indices (S_m_C and S_m_S) are obtained and listed in Table 3.3. Even though S_m is closely related to CCT, it has the advantage to indicate the transient stability directly since a negative (positive) S_m indicates an unstable (stable) situation. From Table 3.3, WTG 9 has a negative transient stability margin which indicates that it will become unstable if a fault occurs close to it. Hence measures need to be taken to increase its stability margin. From our analysis in section 3.5, candidate measures include reducing its real power output and reducing the PLL integral gain.

Another observation is that in most studied cases, the calculated CCTs are smaller than the simulated CCTs which results in conservative estimation of the stability margin. This is due to the fact that the damping effect caused by K_p after the fault clearance is ignored. This feature is preferable since it gives the system operator more confidence in using the calculated stability margin.

The time domain response of WTG 5 following the fault is plotted in Figure 3.13. The blue curve shows the response when the fault is cleared 1/6 cycle before the CCT and the red curve 1/6 cycle after the CCT.

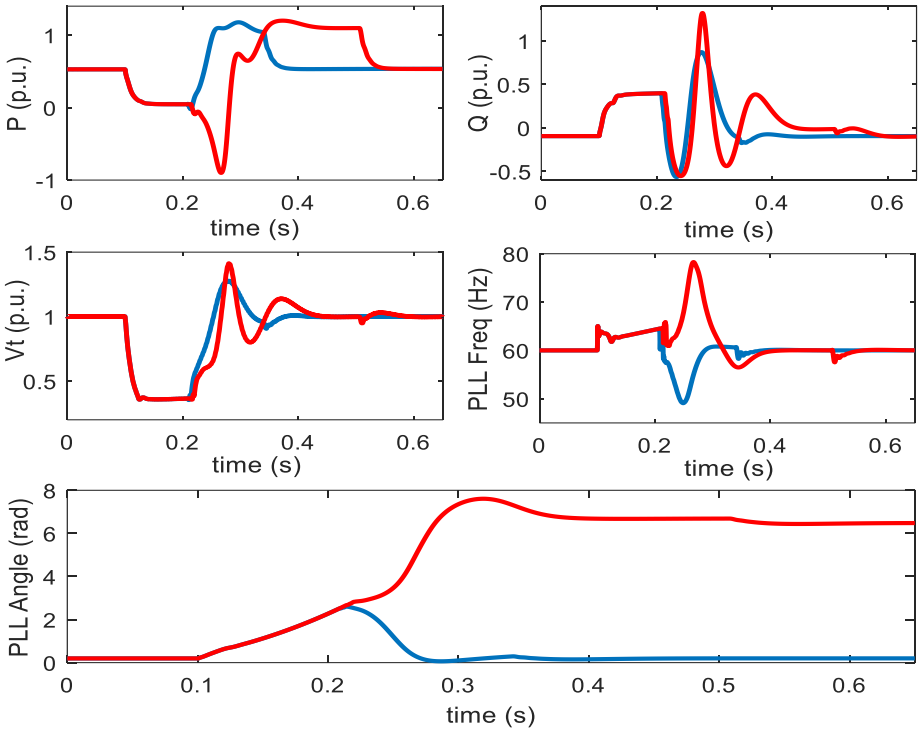

Figure 3.13 Response of WTG 5 in base case. (blue curve: fault duration 0.108s, stable; red curve: fault duration 0.114s, unstable)

As can be seen, when the fault is cleared marginally after the CCT, a "pole slipping" occurs and the PLL angle keeps increasing after the fault clearance. Due to the damping effect caused by the PLL proportional gain, the PLL angle is able to settle down at the stable equilibrium which is 2π apart from the original one. However, this "pole slipping" phenomenon is not advisable since it causes a large oscillation in real/reactive power output of the WTG as well as in the terminal voltage. Also, the overshoot in reactive

power and terminal voltage is increased along with the settling time. Therefore, it is considered as unstable in obtaining the CCT.

3.7.2. Control Parameter Sensitivity on the Stability Margin

To further verify the effectiveness of the proposed CCT calculation method and the applicability of the stability margin index, and to investigate the control parameter sensitivity on the stability margin, control parameters of WTG 5 are varied while the base case control parameters are kept for all other WTGs. The results are listed in Table 3.4. Time domain response of WTG 5 following the fault is plotted in Figure 3.14 through Figure 3.18 with different control parameters. Notice that the control parameters for the PLL, terminal voltage controller and DC link voltage controller are varied individually while all other parameters are kept the same as in the base case.

Table 3.4 CCT and S_m for WTG 5 with different control parameters

		CCT_S (s)	CCT_C (s)	Error (%)	S_m_S	S_m_C
Higher PLL gain	K_i=2800 K_p=120	0.0580	0.0601	3.62	-42	-39.9
Lower PLL gain	K_i=700 K_p=30	0.1857	0.1766	-4.90	87.5	76.6
Higher VC gain	K_{vi}=240 K_{vp}=0	0.1247	0.1185	-4.97	24.7	18.5
Lower VC gain	K_{vi}=60 K_{vp}=0	0.0941	0.0911	-3.19	-5.9	-8.9
Lower DCVC gain	K_{dci}=4 K_{dcp}=1	0.1274	0.1198	-5.97	27.4	19.8

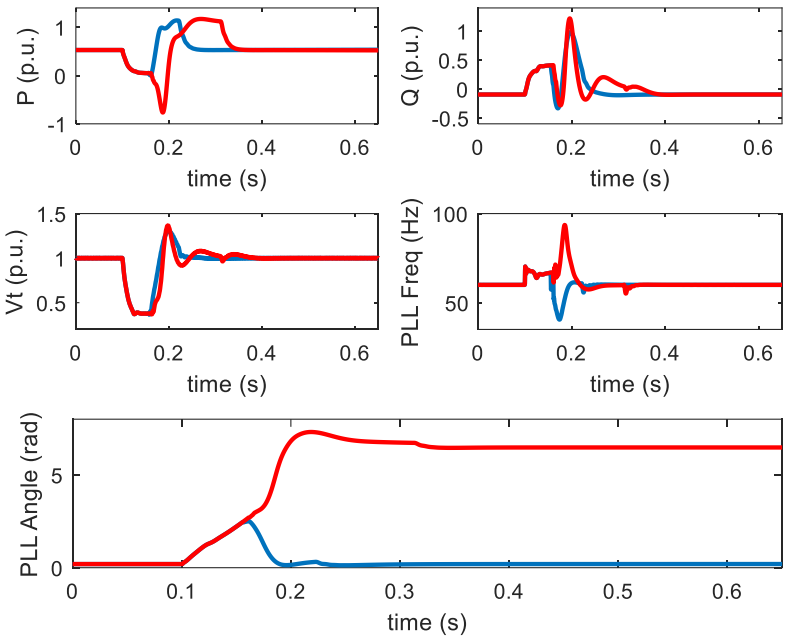

Figure 3.14 Response of WTG 5 with higher PLL gain. (blue curve: fault duration 0.055s, stable; red curve: fault duration 0.061s, unstable)

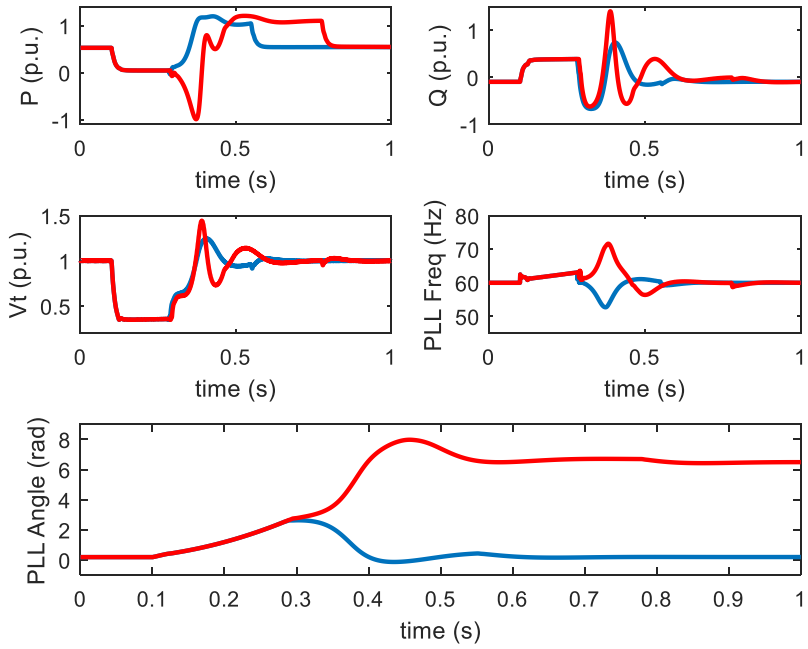

Figure 3.15 Response of WTG 5 with lower PLL gain. (blue curve: fault duration 0.1827s, stable; red curve: fault duration 0.1887s, unstable)

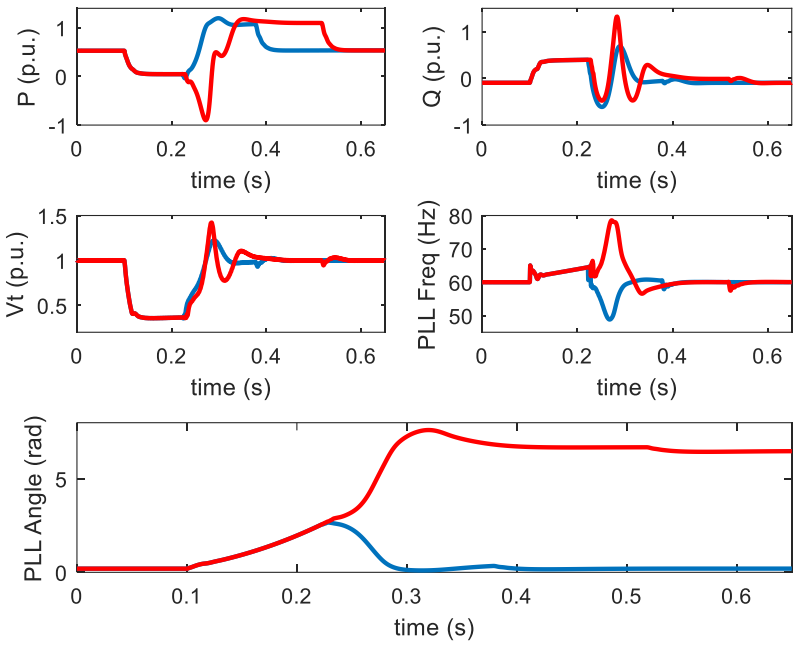

Figure 3.16 Response of WTG with higher VC gain. (blue curve: fault duration 0.1217s, stable; red curve: fault duration 0.1277s, unstable)

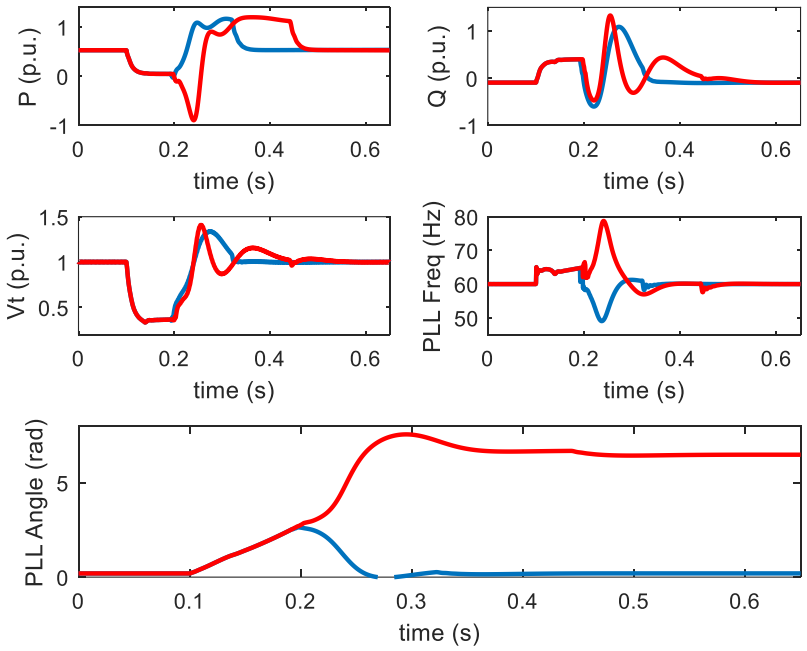

Figure 3.17 Response of WTG 5 with lower VC gain. (blue curve: fault duration 0.0911s, stable; red curve: fault duration 0.0971s, unstable)

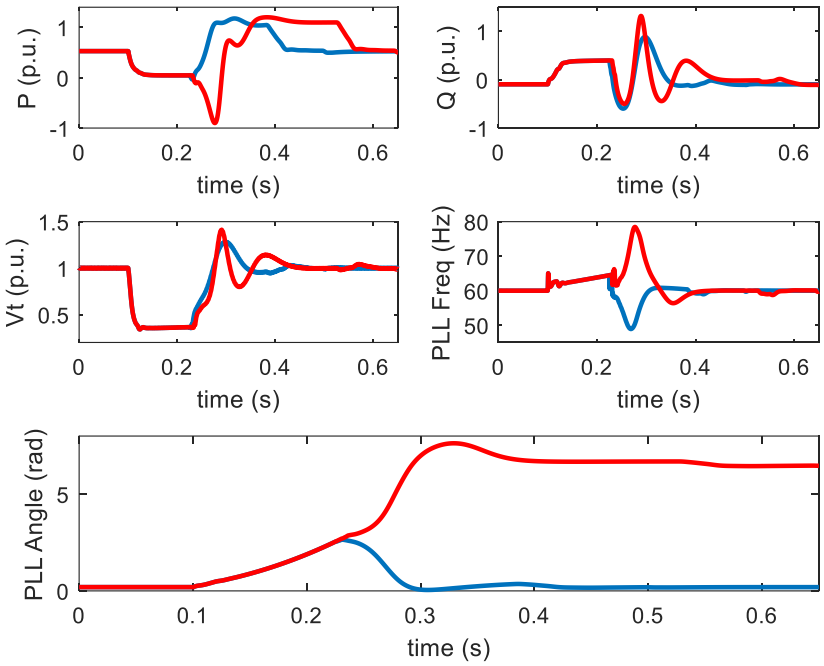

Figure 3.18 Response of WTG 5 with lower DCVC gain. (blue curve: fault duration 0.1244s, stable; red curve: fault duration 0.1304s, unstable)

It can be seen that with the wide range of control parameters tested, the CCTs calculated are very close to the simulated ones with small errors. Compared with the positive stability margin S_m in the base case, the stability margin is increased with lower PLL gain, higher terminal voltage control gain and lower DC link voltage control gain. Increase of the PLL gain and reduction of the terminal voltage control gain can both lead to a negative stability margin which should be avoided.

The study demonstrates the effectiveness of the proposed method to obtain CCT analytically and the usefulness of the stability margin index. Therefore, the proposed method can be applied to study the transient stability margin of CBGs quantitatively and identify the potential transient stability issues of the CBGs. It should be pointed out that

this conclusion is supported by other simulation studies with different operating conditions and control parameters. More demonstrating results are provided in the Appendix.

3.7.3. Comparison with WSCR index

The WSCRs associated with each individual WTG or group of WTGs in the base case are listed in Table 3.3. Details on the WSCR calculation can be found in [47]. For the three individual WTGs (WTG 5, 6, 9), the WSCR associated with WTG 9 has the lowest value, indicating the highest instability risk. This is in line with the proposed stability margin index S_m. However, the WSCR value associated with group 1 and group 2 WTGs are also low indicating high instability risk. For group 2, the WSCR is even lower than WTG 9. These WSCR results are very conservative in evaluating the transient stability of the WTGs since the dynamic simulations show that both group 1 and group 2 WTGs have larger transient stability margins than all the individual WTGs.

Furthermore, it has been shown clearly in Table 3.4 that variation of dynamic parameters has significant impacts on the transient stability margin, which cannot be captured by the WSCR. Therefore, the stability margin index S_m outperforms the WSCR method in evaluating the transient stability performance of CBGs. This is because that $\boldsymbol{S_m}$ is tailored especially for transient stability evaluation considering not only the system strength but also transient stability mechanism and associated control parameters. However, it should be emphasized that the WSCR method is also used as a high level indicator of other types of instability or operational issues that may not be captured by S_m. Thus, the purpose of the proposed transient stability margin index is not to replace the

WSCR method but rather it serves as a supplement to the WSCR method in indicating transient instability issues of CBGs.

3.8. Summary

In this study, the limitations of the present positive sequence modelling of CBGs are revealed. It is demonstrated that the positive sequence models cannot capture the CBG dynamics accurately in LSC systems. The mechanism of CBG transient instability is then investigated. The well-known equal area criterion is adapted to analyze the PLL tracking instability leveraging the similarity between the PLL dynamic equations and the SG swing equations. Influences of power generation, grid strength, and key control parameters on CBG transient stability are identified. Findings from this study shed light on the new transient stability issues that emerge from the integration of converter based generators. Furthermore, a transient stability margin index that can be obtained analytically is proposed considering dynamics from the PLL as well as the grid side converter controllers. It thus offers a convenient way to monitor the transient stability margin of the CBGs and identify potential transient instability in the online operations environment. The proposed index is not suggested to replace the existing SCR based method in indicating stability issues of CBGs. The SCR based method is a high level method aiming at indicating different types of instability and operational issues while the proposed index is tailored for transient stability only but is more precise. Thus it supplements the SCR based method and improves the transient stability evaluation of CBGs.

4. IMPACT OF TRANSMISSION TOPOLOGY CONTROL ON POWER SYSTEM STABILITY AND STABILITY ASSESSMENT OF TTC*

As mentioned in the Introduction, power system transmission topology control (TTC), also termed as transmission line switching, has been demonstrated to be beneficial to the system in both normal and emergency operating conditions. However, the results are obtained mainly from steady state power flow and optimization studies. Power system stability is a natural concern when implementing TTC actions actively and frequently. In this work, the impact of TTC on power system stability is studied in traditional power grids as well as in future smart grid with more renewable penetrations.

Furthermore, as it will be shown in this section, TTC can trigger different forms of instability. Therefore it is highly necessary to assess the stability impact of each proposed line switching before its implementation. In [21], a tool is developed based on eigenvalue analysis to assess the small-signal stability of the system after a line switching. However, even if the steady state solution after a line switching is small-signal stable, the system can still have nonlinear oscillations or become transiently unstable after the line switching. Thus to guarantee the safe implementation of a line switching, a method to efficiently assess all forms of stability (transient stability, voltage stability, small-signal and nonlinear oscillations) for a proposed line switching is needed.

Toward this goal, a dynamic simulation based method is developed to evaluate the above-mentioned different forms of stability all together. This approach saves time and effort and is easier to integrate compared to assessing different forms of stability separately

4.1. Impact of TTC on Transient Stability Margin in a Traditional Power System

Intuitively, TTC actions that switch off transmission lines will reduce the available transmission resources and result in a system with less stability margin. In this subsection the impact of TTC on system transient stability margin is investigated and it is shown that switching off transmission lines can actually improve system stability margin if done properly.

4.1.1. System Description and the Switching Scenario

The system studied is a 9-bus 3-area system which resembles the interconnected power system in the western U.S. and Canada, designated as the Western Systems Coordinating Council (WSCC) and is shown in Figure 4.1. The areas are denoted as top area, left area and right area. All the generators in the system are SGs and are modelled using the six order model. It is assumed that the generators share the same per unit parameters with different MVA bases and the same excitation system with the same control parameters was applied to each generator. Governor is not considered in the study since no generation re-dispatch is involved.

An emergency situation is considered where unexpected loss of generation in the right area causes overflows on the tie lines between the left and the right area. This scenario is shown in Figure 4.1. With no other control options, the load at bus Right2 must

be shed by 13% to reduce the tie line flows to their limit. However, by switching off the tie line between bus Top5 and Right1, line overflows can be relieved without any load shedding. The system power flow solution after switching off the tie line is shown in Figure 4.2. As can be seen, after switching off the tie line, the system is back to normal state directly from the emergency state (if the requirement to keep the same system topology is no longer a part of the normal state definition, which needs to be modified for smart grids with topology controls). What's more, the system after the line switching also satisfies the N-1 criterion, which means the system can withstand the loss of one more line or generator without violating any constraints.

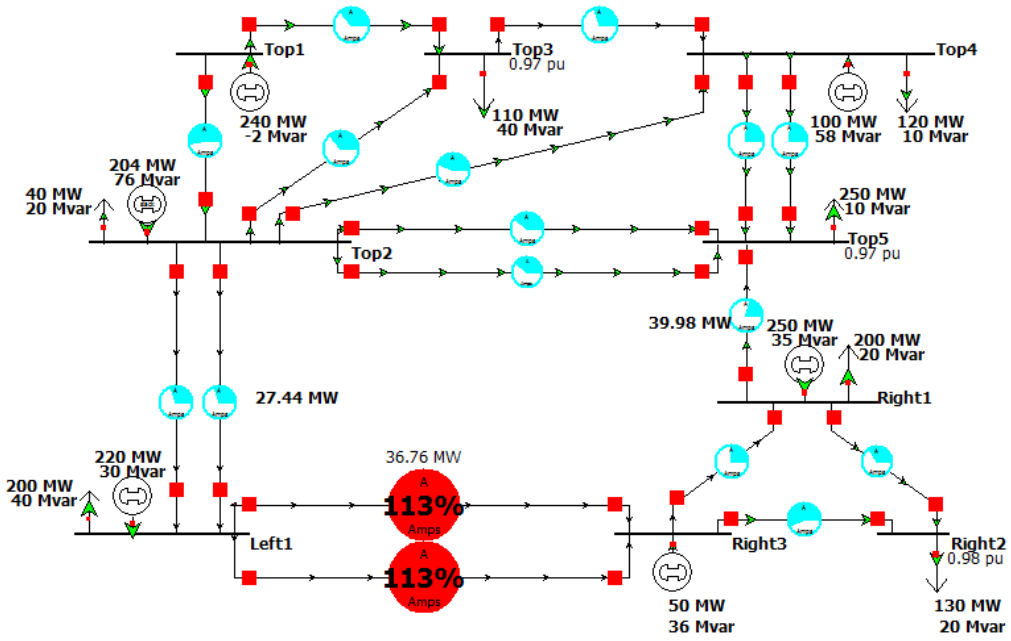

Figure 4.1 Emergency scenario with tie line overflows: Reprinted with permission from [© 2014, IFAC]

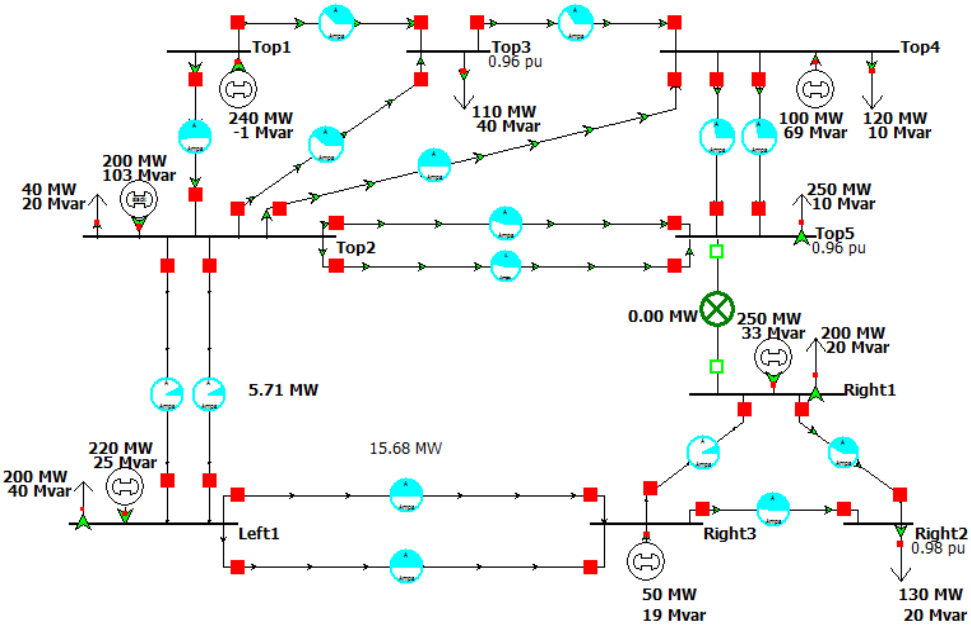

Figure 4.2 Tie line overflows relieved by line switching: Reprinted with permission from [© 2014, IFAC]

4.1.2. Stability Evaluation for the TTC

Dynamic simulation using PSS/E was performed to check whether the system can settle down after the tie line switching. Representative results of relative rotor angles (between generator at bus Right1 and Right3) and bus voltages are shown in Figure 4.3. It can be seen that the system settles down nicely after the tie line switching without causing any stability issues. Thus it is feasible to switch off the tie line to resolve the system emergency.

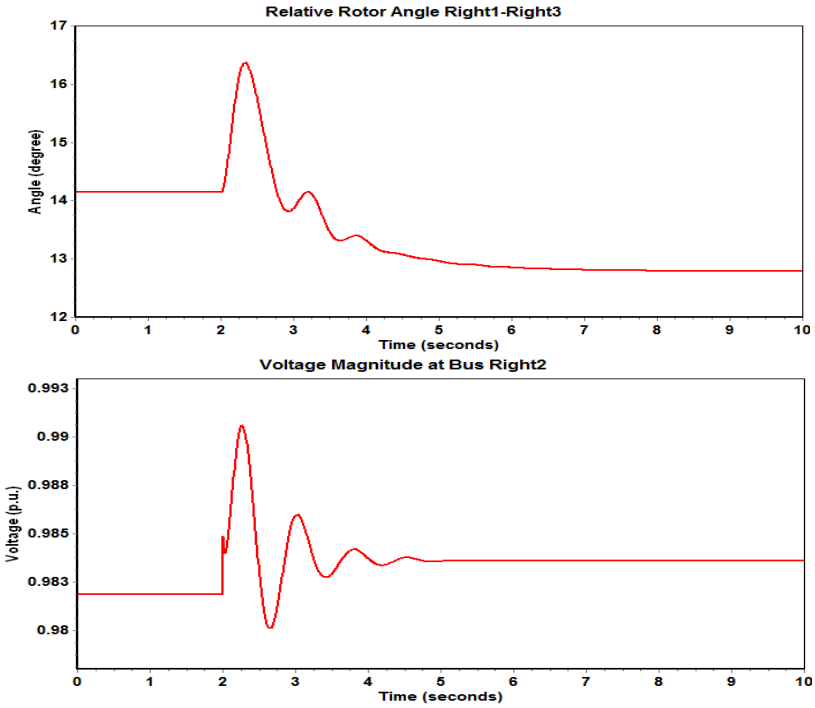

Figure 4.3 System dynamics following the line switching: Reprinted with permission from [© 2014, IFAC]

4.1.3. Impact of the TTC on System Transient Stability Margin

To compare the stability margin between the system before and after the tie line switching, a three phase solid fault was simulated on one tie line between Top2 and Left1 and very close to Top2. The fault was applied at $t = 2s$ and the tie line was taken out at different times to simulate system dynamic behaviour with different fault clearing time.

Critical fault clearing time (CCT), which is defined as the maximum fault clearing time allowed without losing synchronism among synchronous machines, was obtained for both cases based on the simulation results shown in Figure 4.4 and Figure 4.5. The CCT for the emergency system before the line switching is between 0.28s and 0.29s while

between 0.29s and 0.3s for the system after the line switching. This indicates that after the line switching, the system's transient stability margin is marginally improved.

Concluded from this scenario, switching lines alone, if done properly, can resolve system emergency and bring the system back into normal operating state with N-1 criterion satisfied. Also, system stability margin after switching off lines can be improved from the original system. Less transmission resources does not imply less security margin.

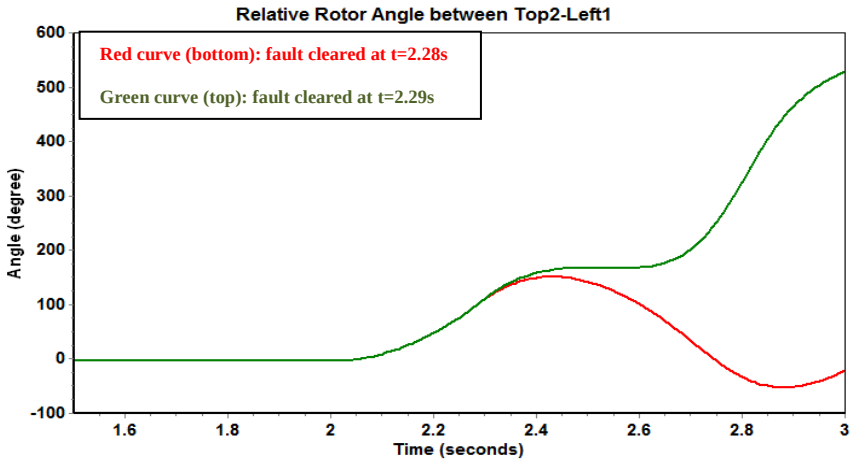

Figure 4.4 Relative rotor angle plot for the system before line switching: Reprinted with permission from [© 2014, IFAC]

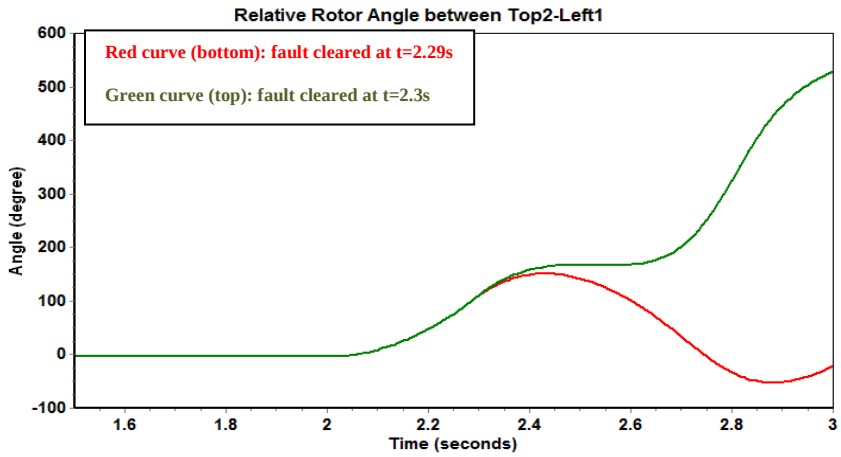

Figure 4.5 Relative rotor angle plot for the system after line switching: Reprinted with permission from [© 2014, IFAC]

4.2. Impact of TTC on Small Signal Stability in a Traditional Power System

In the planning phase, generation dispatch together with system topology can be optimized to minimize generation cost with a certain load profile, as is proposed in [3]. Since the optimized topology and generation dispatch plan may be different for different load profiles, when the forecasted load profile changes, system will transit from one planned optimal state to another by means of line switching and generation re-dispatch. The question to be investigated here is whether the line switching actions can damage system small signal stability and cause unstable oscillations.

4.2.1. System Description and the Switching Scenario

The IEEE 118-bus test case is used in the study. Data of the test system is from reference [48], with some modifications as described in [3]. The system consists of 118 buses, 186 transmission lines, 19 committed SGs with a total real power capacity of 5859

MW, 35 synchronous condensers, and 99 load buses with a total real power demand of 4519 MW.

Assume the system is initially working at the state where all lines were in service and only generation dispatch is optimized with a total cost of $2,054/h [3]. Then 9 lines are switched off one by one and the generation is re-dispatched at last to reach the state in which the generation cost is reduced by 22.3%. Generation cost in both cases is calculated in the DC optimization framework without considering power losses.

The set of line switching solution is obtained with a slight modification of the algorithm presented in [6]; specifically, the objective function was changed to the cost minimization function (as opposed to a load shed recovery function) proposed in [3]. The advantage of using the algorithm in [6] is that it provides a specific schedule to make the line switches one at a time; while the approach in [3] gives only a set of lines to switch without providing a switching sequence. Based on the switching sequence, lines were switched off one by one with 10 seconds in between till the optimal topology was reached (10 seconds is chosen to allow enough time for the breaker to operate and transients to damp down), then the generation was re-dispatched at last to optimize the total generation cost.

4.2.2. Impact of TTC on System Small Signal Stability in Different Loading Situations

Dynamic behaviour of the system can be quite different with the same set of line switching and generation re-dispatch when system loading is different and when different types of controls are applied in the system. In this study, fundamental excitation control

and governor systems are considered and system dynamic behaviour is simulated with different loading levels. To simplify the analysis, it is assumed that the same excitation control system with the same control parameters is applied to each synchronous machine and the SGs are equipped with the same type of governors with different real power output limits. Also, the synchronous machines share the same per unit parameters with different MVA bases. Synchronous machine parameters and control models and parameters can be found in [49].

The switching and dispatch solution described in section 4.2.1 is derived from the base case with a total of 4519 MW real power load, which is defined as 100% loading case. Higher loading situations (110% through 150% loading) are achieved by increasing load at each bus proportionally. The real power generation limit of each generator and line transmission limits are also increased proportionally. As a result, for each loading level, the same set of line switching solution is proposed and the proposed generation dispatch amount for each generator is increased from the base case with the same percentage as the increase of the load. This is due to the linear nature of DC optimization.

For each loading situation, PSS/E is used to simulate system dynamic response following each line switching and the final generation re-dispatch. Constant impedance load was used in the simulation. And the generation re-dispatch is carried out at once without considering generator ramp constraint, which served as the worst case study and speeded up the simulation.

With 100% loading, following each line switching and the generation re-dispatch, the low frequency oscillations in rotor angles and in voltages were damped down properly

and the system reached the optimal state fairly easily. Thus the system after each line switching action remains small signal stable. Representative rotor angle and voltage plots are shown in Figure 4.6 and Figure 4.7. Note that the first line was switched off at $t = 2s$.

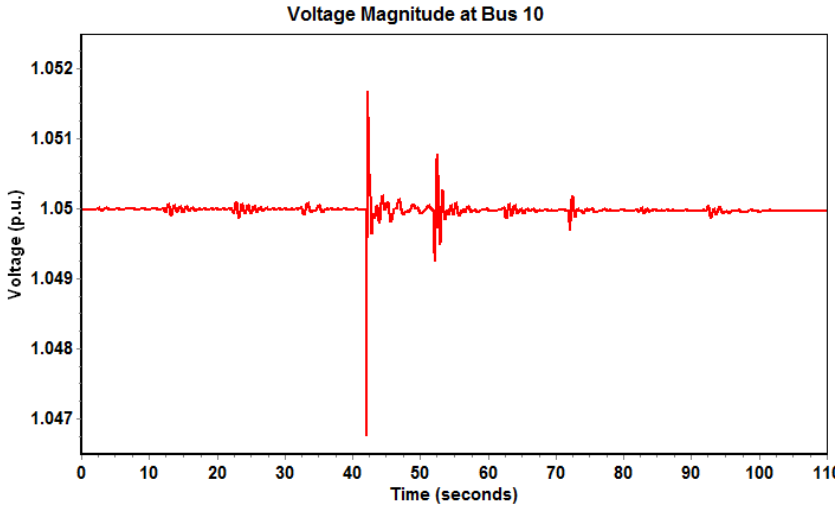

Figure 4.6 Representative bus voltage plot with 100% loading: Reprinted with permission from [© 2014, IFAC]

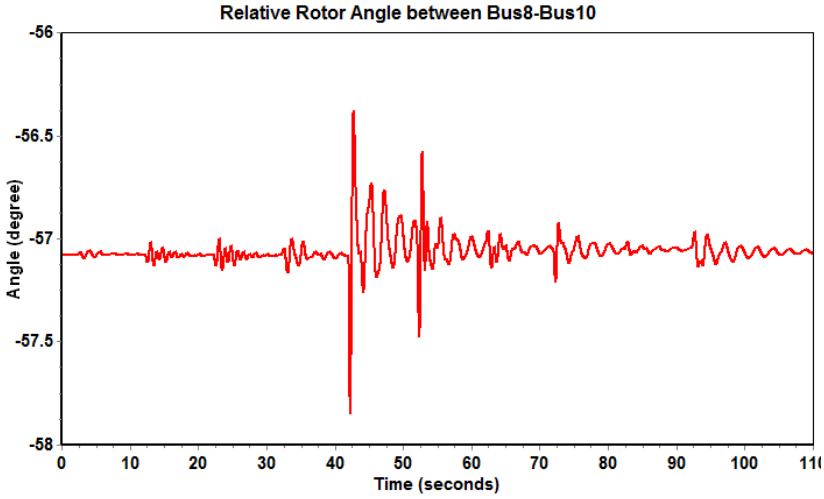

Figure 4.7 Representative rotor angle plot with 100% loading: Reprinted with permission from [© 2014, IFAC]

When the system loading goes higher, magnitudes of the oscillations becomes higher and damping of the oscillations becomes worse. Oscillations with increasing magnitude in rotor angles and voltages began to appear when system loading was increased to 140%, which implies small signal instability of the system after switching off the second line. In Figure 4.8 and Figure 4.9, simulation results following the first three line switching are shown and compared between 130% loading and 140% loading situation. Note that in Figure 4.9, the green curve was shifted up by three degrees for a better view.

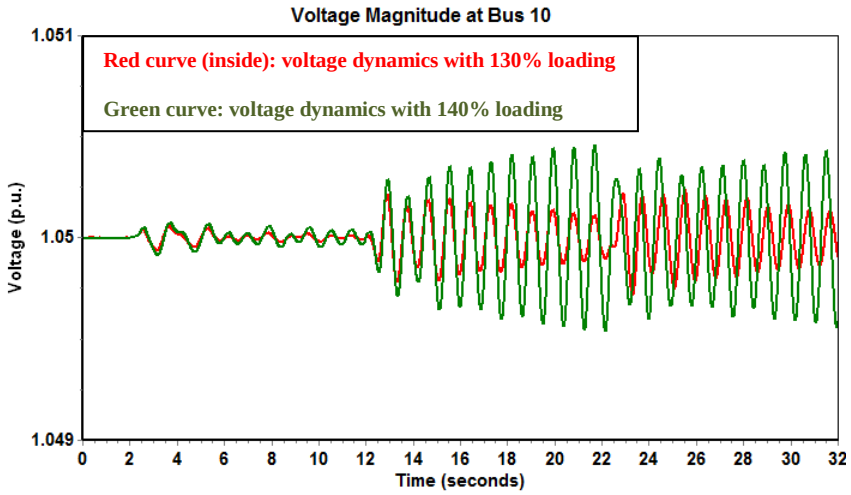

Figure 4.8 Representative bus voltage plot for the first three line switching: Reprinted with permission from [© 2014, IFAC]

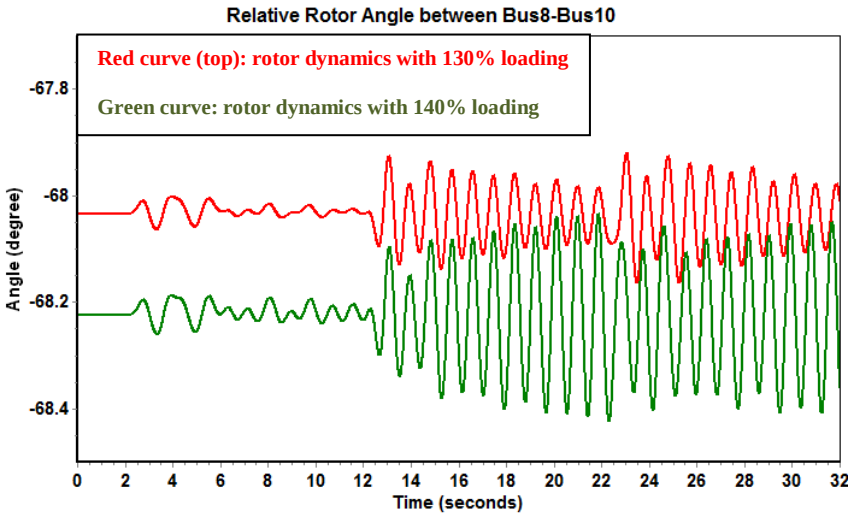

Figure 4.9 Representative rotor angle plot for the first three line switching: Reprinted with permission from [© 2014, IFAC]

From the simulation results, it can be concluded that when system loading is high, small signal instability can be triggered by line switching, which can cause unstable oscillations among SGs and will prevent the system from reaching the planned optimal state, even though the power flow solution exists.

4.2.3. Use of Power System Stabilizer to Damp the Unstable Oscillations Caused by TTC

Since poorly or even negatively damped rotor angle and voltage oscillations can be triggered by TTC actions, and system can become small signal unstable after the change of system topology, power system stabilizer (PSS) is a good candidate to improve system damping after TTC actions. In this subsection the effectiveness of using PSS to improve system damping and to better accommodate TTC actions is demonstrated through dynamic simulation. PSS models and parameters used in this subsection can be found in [49].

Dynamic simulation results for the same set of line switching solutions and with 150% loading are shown in Figure 4.10 and Figure 4.11, when PSS is added to each of the 9 SGs. As can be seen, after adding PSS to the SGs, the oscillations caused by each line switching action are damped down nicely even with higher loading levels and thus the planned optimal state can be reached. It demonstrates that with sufficient damping control in the system, line switching can be carried out to gain full benefits such as reducing the generation costs without worries on small signal instability.

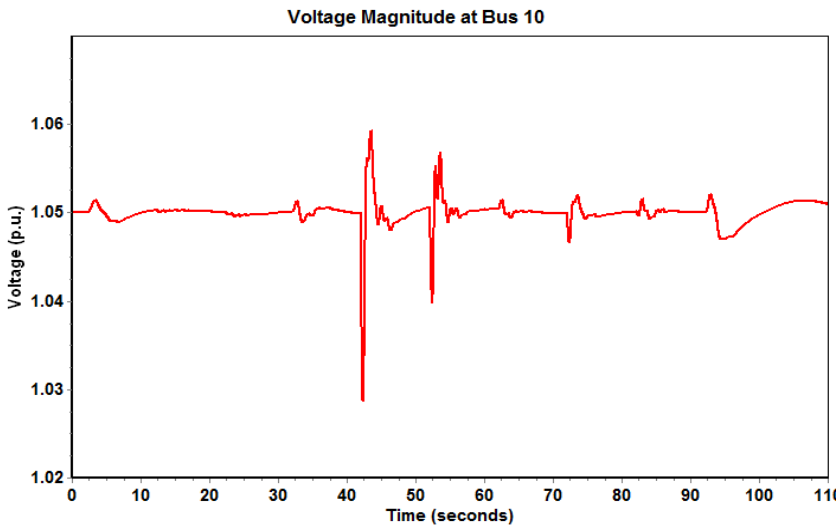

Figure 4.10 Representative bus voltage plot with 150% loading with PSS added: Reprinted with permission from [© 2014, IFAC]

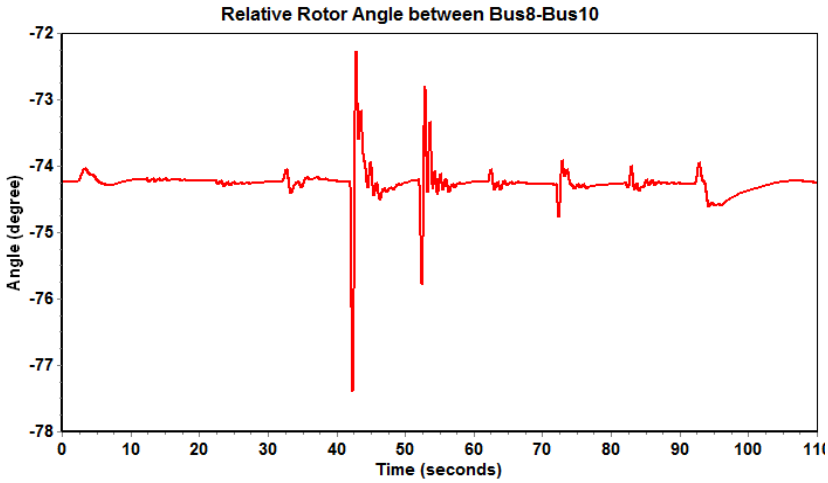

Figure 4.11 Representative rotor angle plot with 150% loading with PSS added: Reprinted with permission from [© 2014, IFAC]

4.3. Impact of TTC on Small Signal Stability in Power Systems with Renewable Integration

Since renewable generators introduce new dynamic behavior into power systems, the impact of TTC on system small signal stability needs to be studied in the new smart grid environment with renewable integrations. In this subsection, the impact of TTC on system small signal stability is investigated through simulation and eigenvalue analysis in a wind power integrated system.

4.3.1. System and TTC Scenario Description

To investigate the impact of TTC on system stability with wind penetration, a 9-bus 6-machine system is set up. The system is divided into two areas (top and bottom area), as can be seen from Figure 4.12.

A wind farm with capacity 311.73 MVA (19.3% of the total system capacity) is integrated in the bottom area (at bus W1). It generates 250 MW (17.8% of the total system

real power generation). A single wind turbine is used to represent the aggregation of 187 GE 1.5MW Type 3 wind turbines in the wind farm. This representation is suitable for analyzing the response of the wind power plant to grid disturbance [31]. The aggregate unit transformer, aggregate collector system and the aggregate substation transformer are also modeled with parameters the same as those presented in Appendix B of [31].

The wind power plant works at the voltage control mode and regulates the voltage at the point of interconnection (bus Bottom 1). The rest of the generators in the system SGs representing traditional coal power plants.

The generic Type 3 wind turbine dynamic model in PSS/E is used for the wind turbine along with its controllers. The example dynamic data in the PSS/E manual is used. The dynamic model and data for the SGs together with the exciters and governors are duplicated from the real Pennsylvania New Jersey Maryland Interconnection (PJM) system. PSS is not equipped with the SGs to begin with and the effect of adding PSS will be analyzed.

A scenario is considered where overflow occurs on the lines between buses Bottom 1 and Bottom 2 (shown in Figure 4.12). It represents a situation where unscheduled power flow (loop flow) causes line overflow in a neighboring system. As can be seen from Figure 4.12, 13 MW enters the bottom area and goes back to the top area without contributing to the net exchange between the two areas. The system is in the emergency state. Switching off the tie line from Top 2 to Bottom 1 is shown by the power flow solution to be an effective corrective solution to relieve the line overflow in the bottom area (shown in Figure 4.13).

This proposed TTC solution is considered hereafter and its impact on system stability is studied. The system before the line switching is denoted as the base case and after switching the switched case.

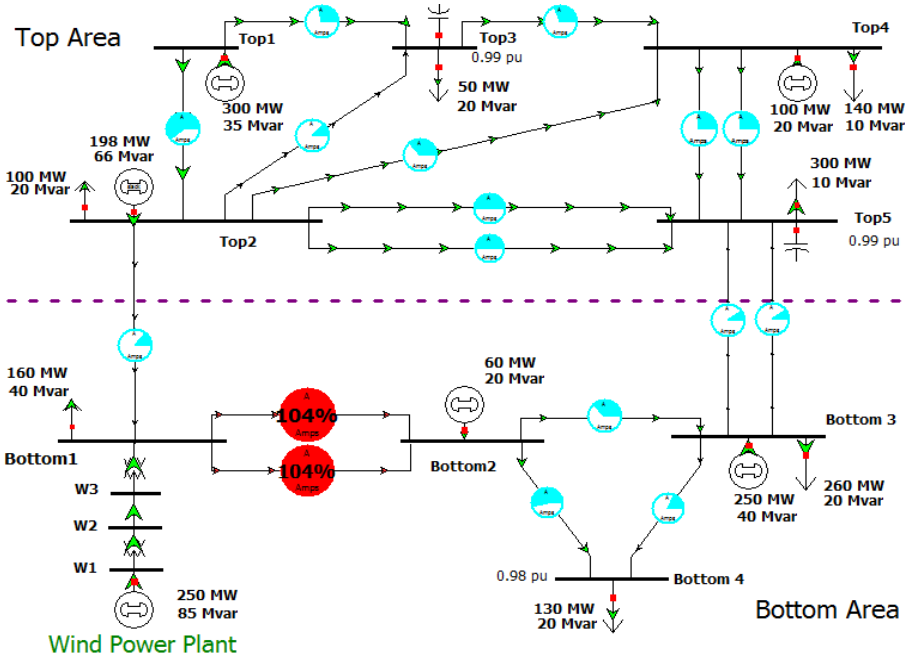

Figure 4.12 System in emergency state: Reprinted with permission from [© 2016, IEEE]

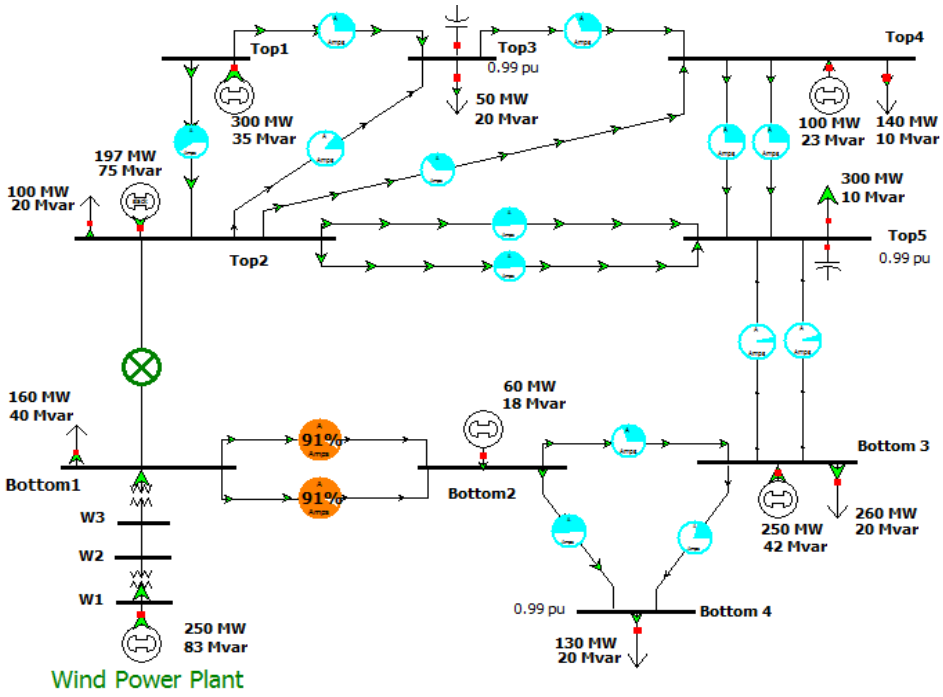

Figure 4.13 Power flow solution after the tie line switching: Reprinted with permission from [© 2016, IEEE]

4.3.2. Potential Small Signal Stability Issues with TTC

Dynamic response of the system after switching off the tie line is simulated using PSS/E and the results are presented in Figure 4.14. The line is switched off at t=1s and simulated till t=10s. From the simulation results, it can be concluded that the system becomes unstable after switching off the tie line. The unstable oscillation (around 1.47 Hz) presents in all the bus voltages and the rotor speeds/angles of all the SGs. Also, it can be seen that the unstable oscillation has the largest magnitude at the location of the wind power plant and propagates to the whole system.

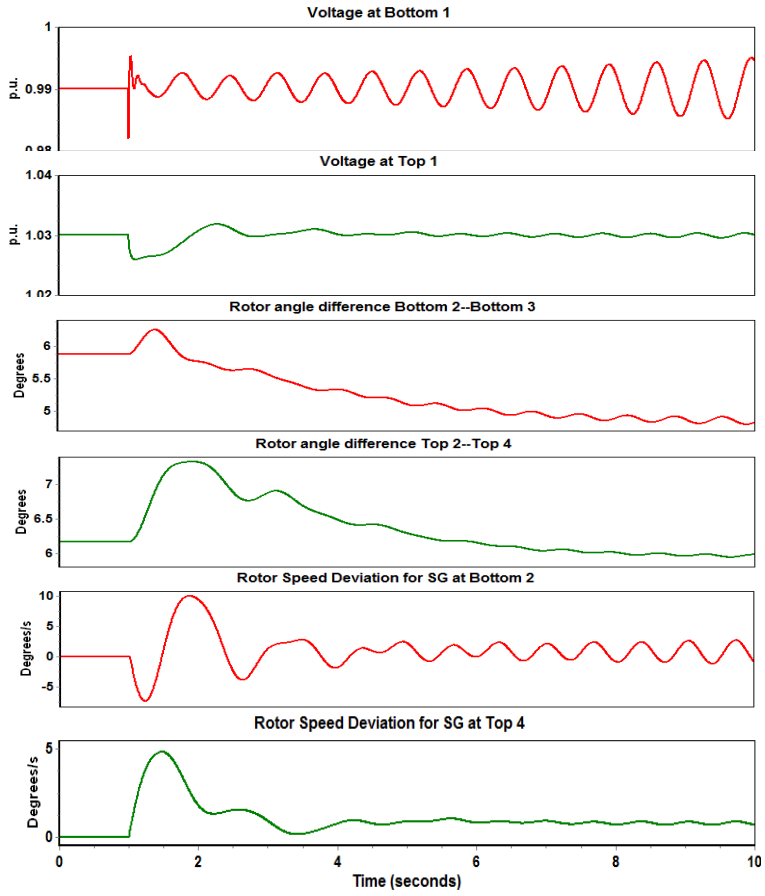

Figure 4.14 System dynamic response after the tie line switching: Reprinted with permission from [© 2016, IEEE]

Eigenvalue analysis is then carried out using the Small-signal Security Assessment Tool (SSAT) to gain a deeper understanding of the unstable oscillations. The critical oscillatory modes with lowest damping for both the base case and the switched case are calculated and listed in Table 4.1.

The eigenvalue analysis reveals four electro-mechanical modes in the system: one inter-area mode (No. 5), in which the two SGs in the bottom area oscillate against the SGs in the top area; two intra-area modes in the top area (No. 2 and 4) and one intra-area mode in the bottom area (No. 3). After the tie line switching, the connection between the two

areas is weakened thus the damping as well as the frequency of the inter-area mode are decreased. The switching affects the intra-area modes differently. Damping of mode 2 is decreased while the damping of mode 3 and 4 is slightly increased. All the electro-mechanical modes in both the base case and the switched case are well damped.

Table 4.1 Critical modes in the system: Reprinted with permission from [© 2016, IEEE]

No.	Base Case		Switched Case		Dominant State
	Freq. (Hz)	Damping (%)	Freq. (Hz)	Damping (%)	
1	1.4105	7.43	1.4786	-1.32	Wind turbine voltage control
2 intra-area	1.1912	11.01	1.184	10.75	Rotor speed at Top 2
3 intra-area	1.2523	12.23	1.2553	12.32	Rotor speed at Bottom 2
4 intra-area	1.1199	13.57	1.1142	14.08	Rotor speed at Top 4
5 inter-area	0.8619	15.07	0.7251	14.65	Rotor speed at Bottom 3

From the eigenvalue analysis, after the line switching, the damping of mode 1 deteriorates by a large amount and it becomes unstable. Its frequency matches the simulation results.

The participation factors related to mode 1 and greater than 0.01 are tabulated in Table 4.2. The studied Type 3 wind turbine generator has the same reactive power/voltage control loops as the ones shown in Figure 2.2 in section 2. The participating state variables from the wind turbine are associated with the reactive power/voltage control loops. With reference to Figure 2.2, Φ_{pv} and Φ_{iv} are state variables associated with the PI controller

in the supervisory voltage control, while Φ_{qi} and Φ_{vi} are state variables associated with the integrators in the reactive power and voltage control part of the VAR controller model. The participated state variables from the SGs include the rotor speed and angle (ω and δ), the generator flux linkage (φ_{fd}) and state variables inside the excitation control system. It can be seen that the participation of SG state variables in mode 1 is much less than the wind turbine voltage controller state variables.

The participation factors of the wind turbine mechanical state variables (rotor speed, turbine speed and twist angle) are zero in mode 1, indicating the decoupling of wind turbine mechanical part from this mode.

Table 4.2 Participation factors (PFs) of mode 1: Reprinted with permission from [© 2016, IEEE]

Bus	Generator Type	State Variable	PFs
W1	Wind (Type 3)	Φ_{qi}	1
		Φ_{pv}	0.3936
		Φ_{vi}	0.1082
		Φ_{iv}	0.0313
Bottom 3	SG	φ_{fd}	0.0518
		ω	0.0259
		δ	0.0250
		exciter internal	0.0203
Top 1	SG	ω	0.0248
		δ	0.0239
Bottom 2	SG	φ_{fd}	0.0193
		ω	0.0118
		δ	0.0114
Top 4	SG	φ_{fd}	0.0142

From the participation factor analysis, it can be concluded that mode 1 is in fact the DFIG VAR controller mode discussed in section 2. As analyzed in section 2.2, damping of the VAR controller mode is very sensitive to line impedance change close to the wind turbine. Therefore, line switching actions close to the wind turbine can deteriorate its damping and cause unstable voltage and power oscillations at the wind turbine, as illustrated here. As can be seen in Table 4.1, the frequency of mode 1 is not close to any of the electromechanical mode in the system. Based on the analysis in section 2.3, this explains the low participation from the SG state variables. If the frequency of mode 1 is close to the inter-area mode in the system, strong mode coupling can occur and the TTC action has the potential to cause severe inter-area oscillations in the system.

The case study demonstrates that this VAR controller mode originated from the wind turbine converter control is very sensitive to system topology change and negatively damped oscillation can be triggered by TTC even when the mode has enough damping (7.43%) before the line switching. This may put restrictions on TTC close to a wind power plant. This conclusion is supported by the real ERCOT event where an outage of a nearby transmission line caused negatively damped oscillations around the wind power plant [32].

4.3.3. Measures to Improve System Damping

Since this mode is associated primarily with the wind turbine voltage controller, its damping is largely affected by the control parameters. Table 4.3 shows the damping and frequency change after K_{Qi} is reduced to half of its initial value for the switched case. The damping of mode 1 increases from -1.32% to 17.39% after the parameter change. The

electro-mechanical modes are not affected by this change. This is expected since wind turbine does not participate in those modes.

PSS is effective in damping down oscillations in SG rotor speeds and angles. Since the SG state variables participate in mode 1 (even though the participation is low), adding PSS to the SGs can also help to increase the damping of mode 1 to some degree. The frequency and damping of the modes after adding PSS to all the SGs are also listed in Table 4.3. As can be concluded, adding PSS has more impact on the electro-mechanical modes and less impact on mode 1 compared to wind turbine voltage controller tuning. The dynamic response of voltage at Bottom 1 after each individual change is shown in Figure 4.15. The system is able to remain stable after the tie line switching with PSS added or K_{Qi} reduced to half.

Table 4.3 Critical modes with PSS added or controller tuned for the switched case: Reprinted with permission from [© 2016, IEEE]

No.	Adding PSS		K_{Qi} reduced to half		Dominant State
	Freq. (Hz)	Damping (%)	Freq. (Hz)	Damping (%)	
1	1.4371	2.56	1.1006	17.39	Wind turbine voltage control
2	0.7997	54.37	1.184	10.75	Rotor speed at Top 2
3	0.6454	53.9	1.2556	12.3	Rotor speed at Bottom 2
4	0.6789	48.86	1.1128	13.95	Rotor speed at Top 4
5	0.581	43.66	0.7213	14.38	Rotor speed at Bottom 3

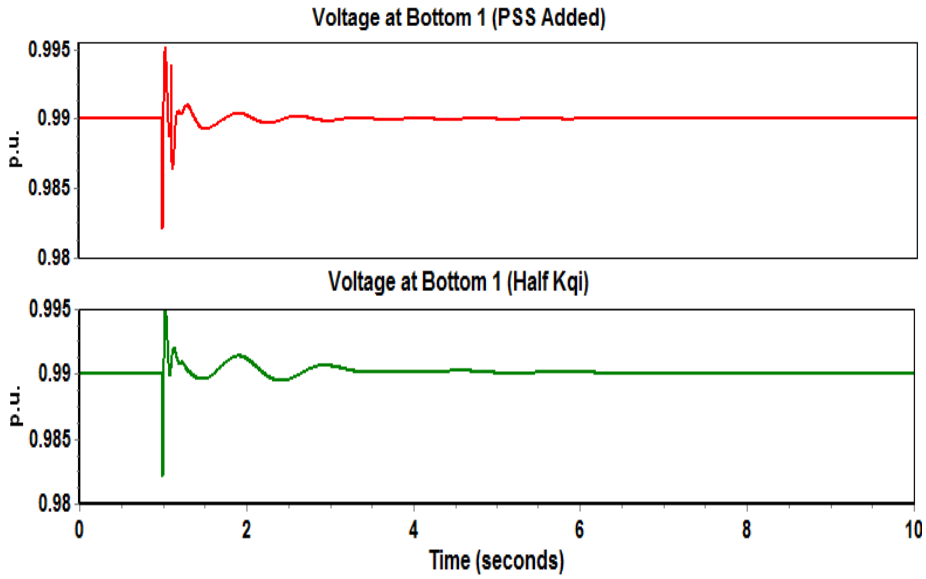

Figure 4.15 Dynamic response after line switching with different changes: Reprinted with permission from [© 2016, IEEE]

4.4. Nonlinear Oscillations Triggered by TTC

In section 4.2 and 4.3, the steady state solutions after the TTC actions are small signal unstable. The unstable oscillations after the TTC actions are indicated by negative damping in the eigenvalues. However, since power system is a complex nonlinear system, even if there exist a stable steady state solution after a TTC action, sustained nonlinear oscillation can occur which prevents the system from converge to the stable steady state solution. This is demonstrated in this section.

The system in Figure 4.12 is considered with some modifications. Oscillations from a hydraulic power plant were observed by the author when simulating the real-scale PJM system following a transmission line switching. Here to investigate the causes of the oscillations, the generator model and its controls at bus Bottom 2 in Figure 4.12 is replaced with the problematic hydraulic generator model and controls identified in the PJM system.

The control parameter K_{Qi} for the wind power plant is reduced in half to increase the damping of the wind turbine induced oscillation mode, so that the oscillations from the hydraulic plant can be focused on.

With the aforementioned changes, system dynamic response after switching off the tie line is shown in Figure 4.16. A sustained oscillation with frequency around 0.32 Hz is observed in the bus voltages as well as in the SG rotor speed and angle responses. The oscillation magnitude is highest at the hydraulic power plant and affects the whole system.

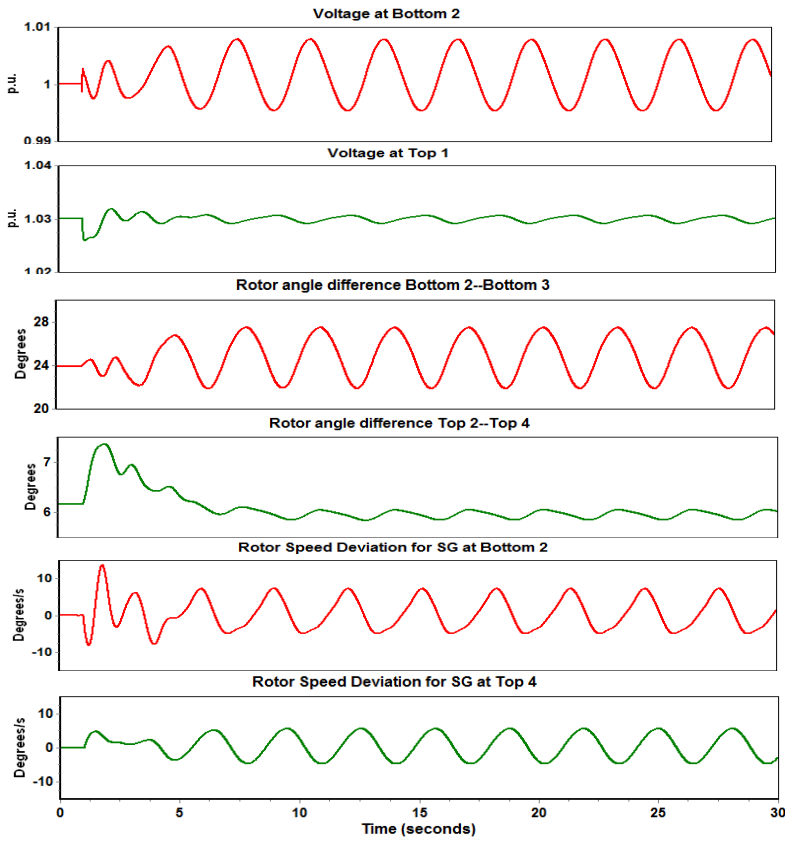

Figure 4.16 System dynamic response to the switching with hydropower integrated: Reprinted with permission from [© 2016, IEEE]

The critical eigenvalues of both the base case and switched case are calculated and tabulated in Table 4.4. As can be seen, the critical modes remain the same as the case without the hydropower integration and all the modes are well damped in both the base case and the switched case. Thus the equilibrium points are stable for the steady state operating points before and after the line switching, and the observed oscillation cannot be explained using the linearized equations as in the eigenvalue analysis.

Table 4.4 Critical modes with hydropower integration: Reprinted with permission from [© 2016, IEEE]

No.	Base Case		Switched Case		Dominant State
	Freq. (Hz)	Damping (%)	Freq. (Hz)	Damping (%)	
1	1.0406	23.6	1.1008	15.41	Wind turbine voltage control
2	1.1921	11.01	1.1841	10.73	Rotor speed at Top 2
3	1.1994	11.31	1.1948	11.77	Rotor speed at Bottom 2
4	1.1157	14.27	1.1075	14.31	Rotor speed at Top 4
5	0.8699	12.72	0.7363	11.7	Rotor speed at Bottom 3

Further investigation reveals that this is nonlinear oscillations caused by the dead-band block in the hydraulic plant excitation system. The IEEE type 4 excitation system is used for this machine and its model is shown in Figure 4.17. The dead-band block encircled in dashed lines introduces a stable limit cycle and the system converges to the limit cycle instead of the stable equilibrium point after the tie line switching.

When the dead-band block is removed from the excitation system, the system is able to settle down to the stable equilibrium point after the line switching. The system responses are shown in Figure 4.18.

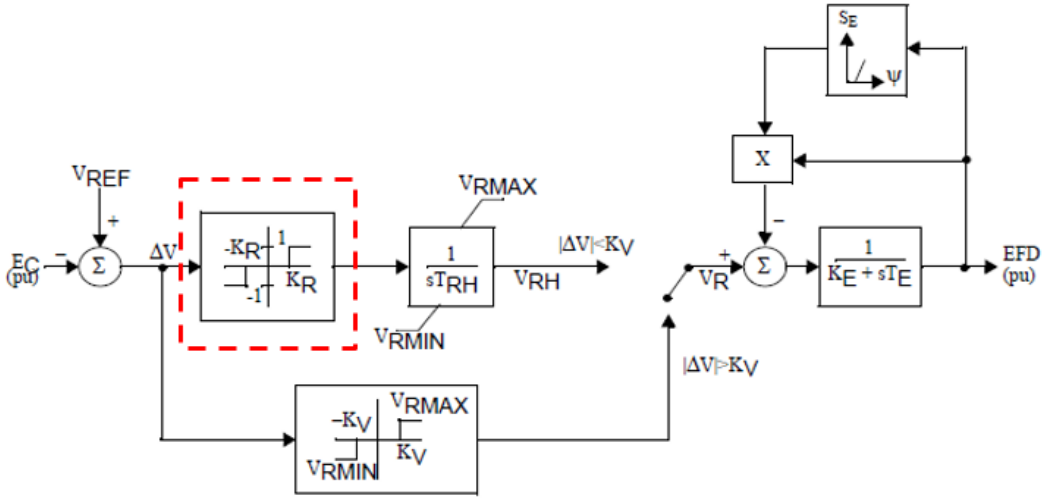

Figure 4.17 IEEE type 4 excitation system: Reprinted with permission from [© 2016, IEEE]

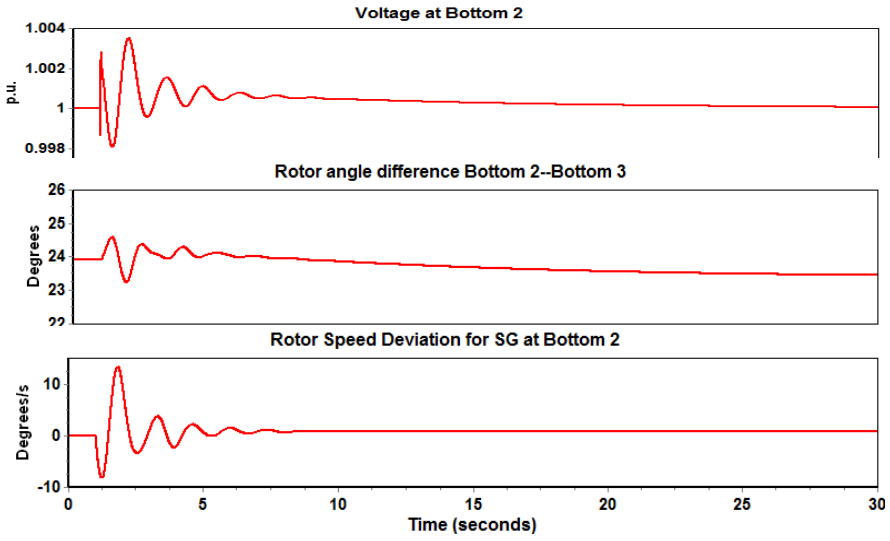

Figure 4.18 Dynamic response after the switching with dead-band block removed: Reprinted with permission from [© 2016, IEEE]

This case study demonstrates the possibility that TTC can trigger nonlinear oscillations in the system. The sustained oscillation propagates from the hydraulic plant and affects the nearby area even though the oscillation magnitude is decreased.

4.5. An Efficient Method to Assess System Stability With TTC

As shown in section 4.2 to 4.4, TTC can trigger negatively damped oscillations or sustained nonlinear oscillations in the system. The system can also become transiently unstable after a line switching [49] [50]. Also, voltage violations may occur in the system after a line switching. Small signal stability analysis falls short in detecting the nonlinear oscillations and transient instability. Thus dynamic simulation must be relied on to fully assess system stability after a proposed line switching.

Here we illustrate a method developed using Python and PSS/E to simulate system dynamic response after a line switching and assess the overall stability of the system. The overall flow chart of the method is shown in Figure 4.19 and the methodology of the method is explained below.

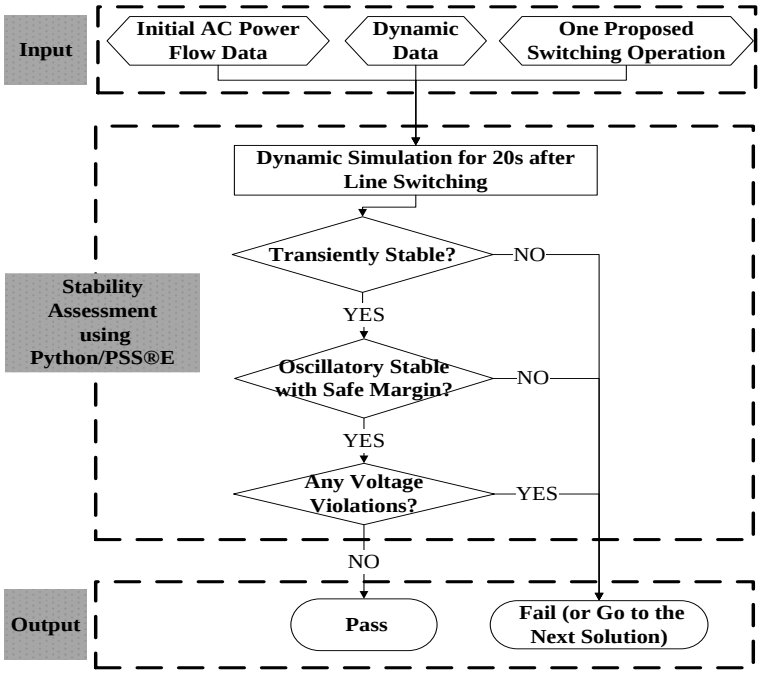

Figure 4.19 Stability assessment flowchart: Reprinted with permission from [© 2016, IEEE]

4.5.1. Transient Stability Assessment

A criterion based on angular separation is set up to detect transient instability. Define angle spread (AS) to be the difference between the largest SG rotor angle (LA) and the smallest SG rotor angle (SA) at a given time.

$$AS(t) = LA(t) - SA(t) \tag{4.1}$$

LA and SA are measured with reference to the system average angle. Define $AS(0)$ to be the initial angle spread at $t = 0s$, $ASmax$ to be the maximum $AS(t)$ from $t = 0s$ to $t = 20s$. Then transient instability is detected if

$$AS_{\max} - AS(0) > 2\pi \tag{4.2}$$

The 2π criterion for transient stability assessment is adopted from the Transient Security Assessment Tool (TSAT) [51].

4.5.2. Oscillatory Stability Assessment

In practice, sufficient damping is required for all the oscillations. For example, ISO New England requires a damping ratio larger than 3% for all the oscillations [52]. This translates to a reduction in oscillation magnitude greater than 32% over two oscillation periods.

In the approach developed, the dynamic simulation is run for 20s after the line switching so that only a single dominant mode (frequency) of oscillation remains in one studied signal. Speed deviation signals of all the generators are then screened by their largest deviation (LD) in the last 5 seconds of the simulation. LD is defined as the difference between the maximum value and the minimum value in the last 5 seconds. A signal is picked for further damping analysis if and only if the largest deviation is larger than 2e-5 p.u.

For each signal that passes the screening, the last peak-to-peak amplitude ($PP1$) and the third last peak-to-peak amplitude ($PP3$) are obtained (illustrated in Figure 4.20). Small-signal criterion is violated if for any one signal

$$PP1 > 0.68 \times PP3 \tag{4.3}$$

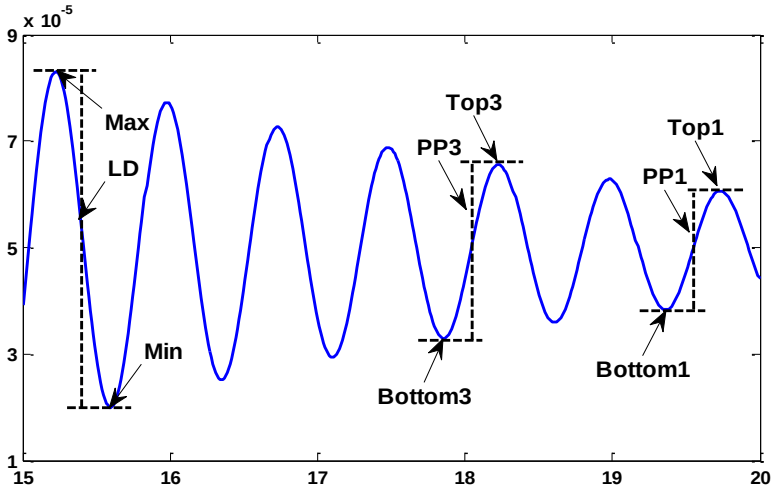

Figure 4.20 Oscillatory stability assessment illustration: Reprinted with permission from [© 2016, IEEE]

4.5.3. Voltage Stability Assessment

A criterion for voltage stability is that, following a given disturbance and following system-control actions, voltages at all buses reach acceptable steady-state levels [35]. If the system after a line switching passes the transient and oscillatory stability check, it then proceed to check for voltage violations in the new steady state.

The average voltage in the last 5 seconds is compared against the upper and lower voltage limits to check for voltage violations. It is to be noticed that even though bus voltages can be calculated by AC power flow, dynamic simulation takes into account all the voltage controls (exciters, excitation limiters, etc.) thus determines the new steady state voltages more accurately. This is why the bus voltages from dynamic simulation are checked against the voltage limits.

4.5.4. Comments on the Stability Assessment Method

The proposed stability assessment method has been implemented for TTC stability assessment in the PJM system for thousands of switching candidates in different scenarios. Based on the experience gained in the tests, this method is effective in detecting different forms of instability including transient, oscillatory and voltage instability. Thus it has the potential to be used in combination with the optimization program to search for TTC options that are beneficial to the system without jeopardizing system stability. When checking system stability following a TTC action, this method is also found to be much faster when compared with eigenvalue analysis alone (carried out using SSAT) for the PJM test cases.

4.6. Summary

As a beneficial tool to be incorporated into power system planning and operation, transmission line switching may cause undesirable disturbances into the system. System stability is undoubtedly a big concern to carry out frequent transmission line switching.

In this section, the impact of TTC on power system transient stability margin is first investigated. It is demonstrated that the transient stability margin of the system can be improved instead of harmed by switching off certain transmission lines.

Research in this section also reveals the potential small signal instability issues and nonlinear oscillation issues that can be caused by transmission line switching in both conventional power grids with SGs only and in power grid with renewable integration. Measures to improve the damping of the small signal oscillations are discussed. With enough well-tuned controls in place, it is promising that transmission line switching can

be beneficial to the system without damaging system stability margin or causing stability issues if it is done properly.

Stability assessment for TTC is highly necessary to avoid triggering sustained or even negatively damped oscillations or transient/voltage instability. Since TTC can trigger different forms of instability in the system, a stability assessment method based on time-domain simulation is proposed to assess different forms of stability all together following a proposed line switching operation. Real-world test cases have proven the effectiveness of the proposed method. The method is also much faster even when compared with eigenvalue analysis alone for the real-world test cases.

5. CONTROL DESIGN FOR BATTERY ENERGY STORAGE SYSTEM TO IMPROVE POWER SYSTEM TRANSIENT STABILITY

In this chapter the control design for BESS is discussed with the purpose to improve power system transient stability. A wide area control method to damp the relative motions among synchronous machines is proposed. It is theoretically proved that the control method can drive the system states to the post disturbance stable equilibrium point if it exists. Simulation studies are also carried out to test the performance of the control method and to compare it with a local damping control approach. The advantages of the proposed wide area control method are demonstrated in the simulation results.

5.1. Mathematical Formulation

5.1.1. System Equations

To develop the system equations, the internal node representation of a dynamic power system illustrated in [53] is adopted with the following assumptions:

1. The synchronous generators are modeled as voltage sources behind the transient reactance (classical model), whose voltage magnitude and the mechanical power input stay constant during the transient period.
2. Loads in the system are represented by passive impedances.
3. Transfer conductances in the system are ignored.

With assumptions 1 and 2, the load nodes and the terminal voltage nodes are eliminated. The resulting system contains only the internal machine nodes, thus the name internal node model. The load impedances and the machine reactances are implicitly

included in the Y matrix of the reduced system. Notice assumption 3 is necessary to construct analytical energy functions for the system and is employed widely in energy function analysis of power systems.

With the above assumptions, the dynamic equations of a n synchronous machine power system are:

$$\begin{aligned} &\dot{\delta}_i = \omega_i \\ &M_i\dot{\omega}_i = P_i - P_{ei} \qquad i = 1, 2, \cdots n \end{aligned} \tag{5.1}$$

where

$$\begin{aligned} &P_{ei} = \sum_{\substack{j=1 \\ j\neq i}}^{n} C_{ij} \sin\left(\delta_i - \delta_j\right) \\ &P_i = P_{mi} - E_i^2 G_{ii} \\ &C_{ij} = E_i E_j B_{ij} \end{aligned} \tag{5.2}$$

and for unit i

$\delta_i, \omega_i =$ generator rotor angle and speed

$M_i =$ moment of inertia

$P_{mi} =$ mechanical power input

$E_i =$ constant generator voltage behind the reactance

$G_{ii} =$ driving point conductance

$B_{ij} =$ transfer susceptance

$\delta_i, \omega_i =$ generator rotor angle and speed

Equation (5.1) is written with respect to a synchronous reference frame. It can be transformed to the well-known center of inertia (COI) reference frame. Denote the total moment of inertia of the system as

$$M_T = \sum_{i=1}^{n} M_i \tag{5.3}$$

The center of angle and center of speed can be defined as

$$\begin{aligned} \delta_o &= \frac{1}{M_T} \sum_{i=1}^{n} M_i \delta_i \\ \omega_0 &= \frac{1}{M_T} \sum_{i=1}^{n} M_i \omega_i \end{aligned} \tag{5.4}$$

The rotor angles and speeds can be defined relative to the center of angle and speed as

$$\begin{aligned} \theta_i &= \delta_i - \delta_o \\ \tilde{\omega}_i &= \omega_i - \omega_o \end{aligned} \tag{5.5}$$

Write (5.1) in terms of the new variables, we have

$$\begin{aligned} \dot{\theta}_i &= \tilde{\omega}_i \\ M_i \dot{\tilde{\omega}}_i &= P_i - P_{ei} - M_i \dot{\omega}_o \qquad i = 1, 2, \cdots n \end{aligned} \tag{5.6}$$

From (5.1)

$$M_T \dot{\omega}_o = \sum_{i=1}^{n} M_i \dot{\omega}_i = \sum_{i=1}^{n} P_i - \sum_{i=1}^{n} P_{ei} = 0 \tag{5.7}$$

Notice in the above equation the sum of P_i and P_{ei} both equal to zero, as is shown in [56]. Plug (5.7) into (5.6), the system dynamic equations in the center of inertia formulation are

$$\begin{aligned} \dot{\theta}_i &= \tilde{\omega}_i \\ M_i \dot{\tilde{\omega}}_i &= P_i - P_{ei} \qquad i = 1, 2, \cdots n \end{aligned} \tag{5.8}$$

5.1.2. Transient Energy Functions

Transient energy function has been well defined for the dynamic system in synchronous reference frame described in (5.1) [53]. Assuming there is a stable equilibrium point after the disturbance, the transient energy function for (5.1) is defined as

$$V(\omega,\delta)=\frac{1}{2}\sum_{i=1}^{n}M_i\omega_i^2-\sum_{i=1}^{n}P_i\left(\delta_i-\delta_i^s\right)-\sum_{i=1}^{n-1}\sum_{j=i+1}^{n}C_{ij}\left(\cos\delta_{ij}-\cos\delta_{ij}^s\right) \qquad (5.9)$$

where ω and δ are the speed and angle vectors and the superscript "s" denotes values at the stable equilibrium point.

The transient energy function is related to physical energy where the kinetic energy stored in generator rotors is

$$V_{KE}(\omega)=\frac{1}{2}\sum_{i=1}^{n}M_i\omega_i^2 \qquad (5.10)$$

and the potential energy in the system is

$$V_{PE}(\delta)=-\sum_{i=1}^{n}P_i\left(\delta_i-\delta_i^s\right)-\sum_{i=1}^{n-1}\sum_{j=i+1}^{n}C_{ij}\left(\cos\delta_{ij}-\cos\delta_{ij}^s\right) \qquad (5.11)$$

It can be seen that at the stable equilibrium point, system transient energy reaches its minimum value zero. Notice the above transient energy function is defined relative to a synchronous reference frame. Therefore when the transient energy becomes zero, the rotors are synchronized and the rotor speed is the same as the synchronous speed.

The transient energy function can also be developed for system equations in the COI reference frame as

$$V(\tilde{\omega},\theta)=\frac{1}{2}\sum_{i=1}^{n}M_i\tilde{\omega}_i^2-\sum_{i=1}^{n}P_i\left(\theta_i-\theta_i^s\right)-\sum_{i=1}^{n-1}\sum_{j=i+1}^{n}C_{ij}\left(\cos\theta_{ij}-\cos\theta_{ij}^s\right) \quad (5.12)$$

The kinetic and potential energy in the COI reference frame relate to those in the synchronous reference frame as follows

$$V_{KE}(\tilde{\omega})=\frac{1}{2}\sum_{i=1}^{n}M_i\tilde{\omega}_i^2=\frac{1}{2}\sum_{i=1}^{n}M_i\omega_i^2-\frac{1}{2}M_T\omega_o^2 \quad (5.13)$$

The kinetic energy relative to COI is the total kinetic energy minus the COI kinetic energy.

$$\begin{aligned}V_{PE}(\theta)&=-\sum_{i=1}^{n}P_i\left(\theta_i-\theta_i^s\right)-\sum_{i=1}^{n-1}\sum_{j=i+1}^{n}C_{ij}\left(\cos\theta_{ij}-\cos\theta_{ij}^s\right)\\&=V_{PE}(\delta)-\sum_{i=1}^{n}P_i\left(\delta_0-\delta_o^s\right)\end{aligned} \quad (5.14)$$

The potential energy in the COI reference frame is the total potential energy minus the COI potential energy.

It can be seen that the transient energy defined in the COI reference frame is the energy related to relative rotor angles and speeds. Therefor the energy related to the COI is subtracted from the total system energy. This framework is very useful in power system transient stability analysis since power system transient stability mainly concerns about relative motions among the synchronous machines and the synchronism among them. If the rotor speeds relative to COI is zero and the relative rotor angles stay constant then the system is considered to be stable, even though the COI may be in motion relative to the synchronous reference frame. In other words, power system transient stability concerns about whether the system converges to a synchronous equilibrium but not a frequency equilibrium [54]. It is reasonable to analyze synchronous equilibrium and frequency equilibrium separately since synchronization needs to be guaranteed right after a large

disturbance by fast control actions while overall frequency of the system can be driven to synchronous frequency by relatively slower control such as the governors.

Based on the above observations, the COI based framework will be used to analyze the effect of different control methods on power system transient stability.

5.2. Control Design

5.2.1. Motivation via Single Machine System

Consider a single machine infinite bus system whose post-disturbance system equations are

$$\begin{aligned} \dot{\delta} &= \omega \\ M\dot{\omega} &= P_m - P_e \sin\delta \end{aligned} \tag{5.15}$$

Its potential energy can be obtained as

$$V_{PE} = -P_m\left(\delta - \delta_s\right) - P_e\left(\cos\delta - \cos\delta_s\right) \tag{5.16}$$

The potential energy function is plotted in Figure 5.1 [53], where $\delta = \delta^s$, $\omega = 0$ is the post-disturbance stable equilibrium point. δ^u and $\hat{\delta}^u$ are the two closest unstable equilibrium points and δ^{cl} is the rotor angle right after the disturbance.

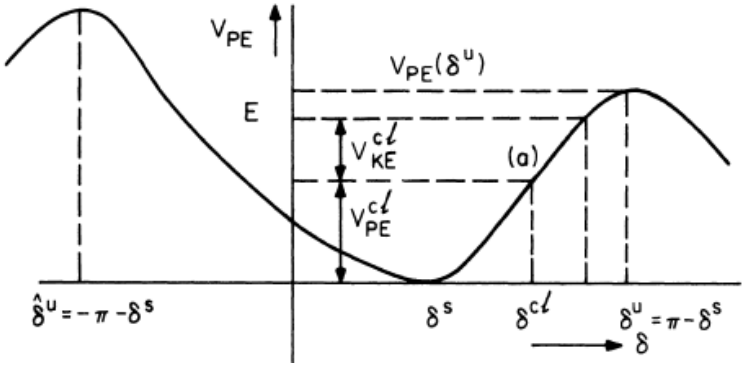

Figure 5.1 Potential energy "well": Reprinted from [53]

The total transient energy after the disturbance is

$$E = V_{KE}^{cl} + V_{PE}^{cl} \tag{5.17}$$

The rotor angle is increasing after the disturbance toward the unstable equilibrium point due to the kinetic energy stored in the system. Since the system is conservative, there is no energy loss along the path. The system will become transiently unstable and pole slipping will occur if the transient energy E is greater than the potential energy at δ^u, which defines the edge of the potential energy well.

From this illustration, transient stability of the system will be improved if the potential energy at the unstable equilibrium point is increased. This method has been pursued and can be achieved, for example, by fast excitation control of the synchronous generators.

Another control method to improve the transient stability is to add damping to the system so that the kinetic energy is reduced along the path and thus the unstable equilibrium point is not reached. This idea is relatively less pursued before probably because of a lack in equipment to provide fast and high energy injection/absorption to achieve significant damping effect right after a large disturbance. With the rapid development in BESS technology, the power and energy capacity of BESS is increasing and its deployment in power system is becoming more common. It is promising to utilize the BESS to provide damping to power system and improve its transient stability.

Notice that damping has been widely discussed with regard to power system small signal stability and oscillation performance and there are devices deployed to increase oscillation damping of the system. The most common device is the PSS. However, these

devices are designed to work in the neighborhood of the operating point only and their influence on power system transient stability is not significant. For example, it is pointed out in [35] that PSS has little influence on the first swing stability while it mainly damps the subsequent swings.

5.2.2. Local Damping Control

Damping control method for BESS to improve oscillation damping in power system is proposed in [55] based on the linearized analysis. The method is based on frequency measurement at the local generator and requires no wide area signal thus no communication requirement.

This control method is termed local damping control and its influence on power system transient stability is discussed and tested in this work.

Real power output of the BESS is regulated to provide damping to the system. The BESS is assumed to connect at a synchronous generator terminal and its real power output is controlled as

$$P_{BESS} = -D\omega \tag{5.18}$$

where D is a constant and ω is the speed deviation (from the synchronous speed) of the local synchronous generator.

Consider the scenario where one BESS is connected at each generator terminal bus (as is the scenario in [55]) with local damping control. The system dynamic equations in (5.1) become

$$\begin{aligned} &\dot{\delta}_i = \omega_i \\ &M_i\dot{\omega}_i = P_i - P_{ei} - D_i\omega_i \qquad i = 1, 2, \cdots n \end{aligned} \tag{5.19}$$

As discussed in section 5.1.2, the transient energy function based on the COI reference frame is well suited for transient stability study. Thus (5.19) is first transformed into the COI reference frame as

$$\begin{aligned} \dot{\theta}_i &= \tilde{\omega}_i \\ M_i\dot{\tilde{\omega}}_i &= P_i - P_{ei} - D_i\omega_i - M_i\dot{\omega}_o \qquad i = 1, 2, \cdots n \end{aligned} \tag{5.20}$$

and

$$M_T\dot{\omega}_o = \sum_{i=1}^{n} M_i\dot{\omega}_i = \sum_{i=1}^{n} P_i - \sum_{i=1}^{n} P_{ei} - \sum_{i=1}^{n} D_i\omega_i = -\sum_{i=1}^{n} D_i\left(\tilde{\omega}_i + \omega_o\right) \tag{5.21}$$

Plug (5.21) into (5.20), we have

$$\begin{aligned} \dot{\theta}_i &= \tilde{\omega}_i \\ M_i\dot{\tilde{\omega}}_i &= P_i - P_{ei} - D_i\tilde{\omega}_i - D_i\omega_o - \frac{M_i}{M_T}\sum_{i=1}^{n} D_i\tilde{\omega}_i - \frac{M_i}{M_T}\sum_{i=1}^{n} D_i\omega_o \qquad i = 1, 2, \cdots n \end{aligned} \tag{5.22}$$

Equation (5.22) is the set of system equations in the COI reference frame. It is important to notice that the relative motions are now coupled with the COI motion because of the damping control. Therefore the motion of the center of inertia will affect the relative motions and thus affect the transient stability of the system.

Notice that this coupling can be eliminated by applying "uniform damping" to the system where

$$\frac{D_i}{M_i} = \mu \quad for\ \forall i \in 1, 2, \cdots n \tag{5.23}$$

and μ is a positive constant. With uniform damping, it can be easily shown as in [56] that (5.22) becomes

$$\begin{aligned} \dot{\theta}_i &= \tilde{\omega}_i \\ M_i \dot{\tilde{\omega}}_i &= P_i - P_{ei} - D_i \tilde{\omega}_i \qquad i = 1, 2, \cdots n \end{aligned} \tag{5.24}$$

Therefore with uniform damping, the motion relative to COI is independent of the COI motion itself.

The transient energy function for the COI based dynamic equations in (5.20) or equivalently (5.22) is

$$V(\tilde{\omega}, \theta) = \frac{1}{2} \sum_{i=1}^{n} M_i \tilde{\omega}_i^2 - \sum_{i=1}^{n} P_i \left(\theta_i - \theta_i^s \right) - \sum_{i=1}^{n-1} \sum_{j=i+1}^{n} C_{ij} \left(\cos\theta_{ij} - \cos\theta_{ij}^s \right) \tag{5.25}$$

Notice the energy function is the same as (5.12) and is unchanged after applying the local damping control. However, with the damping control, the system is no longer conservative and the derivative of the energy function can be derived as

$$\begin{aligned} \dot{V}(\tilde{\omega}, \theta) &= \frac{\partial V_{PE}(\theta)}{\partial \theta} \dot{\theta} + \frac{\partial V_{KE}(\tilde{\omega})}{\partial \tilde{\omega}} \dot{\tilde{\omega}} \\ &= -\sum_{i=1}^{n} \tilde{\omega}_i \left(P_i - P_{ei} \right) + \sum_{i=1}^{n} \tilde{\omega}_i \left(P_i - P_{ei} \right) - \dot{\omega}_o \sum_{i=1}^{n} M_i \tilde{\omega}_i - \sum_{i=1}^{n} D_i \omega_i \tilde{\omega}_i \\ &= -\sum_{i=1}^{n} D_i \omega_i \tilde{\omega}_i \end{aligned} \tag{5.26}$$

As can be seen, the total energy dissipation rate is the sum of the dissipation rate at each generator location. Notice $D_i \omega_i \tilde{\omega}_i$ is sign indefinite. This means during the transient period, local damping control at some locations may dissipate the transient energy while at other locations may actually inject transient energy into the system, which is harmful for the transient stability.

Moreover, since the dissipation rate depends on the trajectory of ω_i and $\tilde{\omega}_i$ which can be different for different disturbances, the local damping control at a certain location

can dissipate transient energy for some disturbances while inject energy for others. It can also happen that the local damping control first inject energy and then dissipate energy as time evolves. All these points will be illustrated and discussed in more details later on.

5.2.3. COI based Wide Area Damping Control

The sign indefiniteness of the dissipation rate associated with the local damping control and the possibility that it injects transient energy into the system and affect transient stability adversely motivates the design of a novel control method to avoid the aforementioned drawbacks.

In this section a wide area damping control method to improve the transient stability of the system is proposed. The control is designed solely based on the COI reference frame, thus it is termed the COI based damping control.

Same as the local damping control, real power output of the BESS is regulated to provide damping to the system. The BESS is assumed to connect at a synchronous generator terminal and its real power output is controlled as

$$P_{BESS} = -D\tilde{\omega} \tag{5.27}$$

where D is a damping constant and $\tilde{\omega}$ is the speed deviation (from the COI speed) of the local synchronous generator.

It can be seen that to achieve this control, measurement of all the rotor speeds in the system is needed to find the speed of COI. Thus it is a wide area control method which requires data transfer across the system.

The system dynamic equation with the COI based damping control applied at each synchronous machine is

$$\begin{aligned} \dot{\delta}_i &= \omega_i \\ M_i\dot{\omega}_i &= P_i - P_{ei} - D_i\tilde{\omega}_i \qquad i = 1, 2, \cdots n \end{aligned} \tag{5.28}$$

Convert the equations to the COI reference frame, we have

$$\begin{aligned} \dot{\theta}_i &= \tilde{\omega}_i \qquad\qquad\qquad i = 1, 2, \cdots n \\ M_i\dot{\tilde{\omega}}_i &= P_i - P_{ei} - D_i\tilde{\omega}_i - M_i\dot{\omega}_o \\ &= P_i - P_{ei} - D_i\tilde{\omega}_i - \frac{M_i}{M_T}\sum_{i=1}^{n} D_i\tilde{\omega}_i \end{aligned} \tag{5.29}$$

Notice from (5.29) the important difference when compared with the local damping control is that with the COI based control, the relative motions in the system are completely decoupled with the motion of the COI.

Unlike the local damping control, this control will not drive the rotor speed of each synchronous machine toward the synchronous speed. Rather, it hinders the relative motion among different rotor angles and drive the rotor speeds in the system to the speed of the COI, which is not necessarily the synchronous speed.

An interesting case would be when the local rotor speed is higher than the synchronous speed but lower than the COI speed. With COI based control, the BESS at the local generator will inject power to increase its rotor speed with the purpose to reduce the speed difference among SGs in the system, even though the local rotor speed is already higher than the synchronous speed. This is the main difference of COI based control when compared with local damping control. The effect of COI based control is always against relative rotor motions in the system. As discussed in section 5.1.2, transient stability is directly related to the relative motion among the synchronous machines. Therefore, this control method is always beneficial for the transient stability of the system.

Note that with COI based control, the task of driving the COI speed to the synchronous speed is left to the Automatic Generation Control (AGC), which is outside the time scale of transient stability analysis.

The transient energy function for (5.29) is the same as (5.25) and the derivative of the transient energy function is derived as

$$\begin{aligned}\dot{V}(\tilde{\omega},\theta) &= \frac{\partial V_{PE}(\theta)}{\partial\theta}\dot{\theta} + \frac{\partial V_{KE}(\tilde{\omega})}{\partial\tilde{\omega}}\dot{\tilde{\omega}} \\ &= -\sum_{i=1}^{n}\tilde{\omega}_i\left(P_i - P_{ei}\right) + \sum_{i=1}^{n}\tilde{\omega}_i\left(P_i - P_{ei}\right) - \dot{\omega}_o\sum_{i=1}^{n}M_i\tilde{\omega}_i - \sum_{i=1}^{n}D_i\tilde{\omega}_i\tilde{\omega}_i \\ &= -\sum_{i=1}^{n}D_i\tilde{\omega}_i^2\end{aligned} \tag{5.30}$$

Compare with (5.26) , the derivative of the energy function is negative whenever there is relative motion in the system. This indicates that the COI based damping control at each location contributes to dissipate the transient energy and help to stabilize the system during the entire transient period, which makes it superior compared to the local damping control.

It is worth pointing out that when uniform damping condition in (5.23) is assumed, the system dynamic equations for the COI damping control are

$$\begin{aligned}\dot{\theta}_i &= \tilde{\omega}_i \qquad\qquad i = 1,2,\cdots n \\ M_i\dot{\tilde{\omega}}_i &= P_i - P_{ei} - D_i\tilde{\omega}_i - \frac{M_i}{M_T}\sum_{i=1}^{n}D_i\tilde{\omega}_i \\ &= P_i - P_{ei} - D_i\tilde{\omega}_i - \frac{\mu M_i}{M_T}\sum_{i=1}^{n}M_i\tilde{\omega}_i \\ &= P_i - P_{ei} - D_i\tilde{\omega}_i\end{aligned} \tag{5.31}$$

which is the same as the equations with local damping control in the COI reference frame shown in (5.24).

5.3. Theoretical Basis for Utilizing Damping Control to Improve Transient Stability

As discussed in section 5.2.1, the idea to add damping to power system to improve transient stability is motivated from the single machine example. In this section, we provide theoretical basis to the method and prove that power system transient stability can be guaranteed in a multi-machine power system with sufficient damping.

Throughout this section the uniform damping condition in (5.23) is assumed and the system dynamic equations in (5.24) and equivalently (5.31) are considered. Therefore the conclusion in this section applies both to the local and the COI based damping control.

5.3.1. Preliminaries

5.3.1.1. The Gradient System and Its Stability

As shown in section 5.1.2, the potential energy function for the system in (5.24) is shown as

$$V_{PE}(\theta) = -\sum_{i=1}^{n} P_i\left(\theta_i - \theta_i^s\right) - \sum_{i=1}^{n-1}\sum_{j=i+1}^{n} C_{ij}\left(\cos\theta_{ij} - \cos\theta_{ij}^s\right) \tag{5.32}$$

Then (5.24) is equivalent to

$$\begin{aligned}
&\dot{\theta} = \tilde{\omega} \\
&M\dot{\tilde{\omega}} = -\frac{\partial V_{PE}(\theta)}{\partial \theta} - D\tilde{\omega} \\
&\theta = \left[\theta_1 \cdots \theta_n\right]^T;\ \tilde{\omega} = \left[\tilde{\omega}_1 \cdots \tilde{\omega}_n\right]^T \\
&M = diag\left(M_1 \cdots M_n\right) \\
&D = diag\left(D_1 \cdots D_n\right)
\end{aligned} \tag{5.33}$$

Notice (5.33) is shown in the vector form.

The gradient system of (5.33) is defined in [57] as

$$\dot{\theta} = -\frac{\partial V_{PE}(\theta)}{\partial \theta} \tag{5.34}$$

Two theorems regarding the stability and the stability region of the gradient system are provided next along with the proof.

Theorem 1

Let $\theta = \theta^s, \tilde{\omega} = 0$ be a stable equilibrium of (5.33), then $\theta = \theta^s$ is an asymptotically stable equilibrium point of the gradient system (5.34).

Proof:

Since $\theta = \theta^s, \tilde{\omega} = 0$ is a stable equilibrium point of (5.33), from the Lyapunov theory, V_{PE} has a local minimum value at $\theta = \theta^s$. Then by Theorem 3.2.1 in [56] $\theta = \theta^s$ is an asymptotically stable equilibrium point of the gradient system (5.34).

Theorem 2

Stability boundary of the gradient system (5.34) with respect to the stable equilibrium point $\theta = \theta^s$ is the union of all stable manifolds of the unstable equilibrium points on the stability boundary.

$$\partial A(\theta^s) = \bigcup_{\theta_i \in E \cap \partial A(\theta^s)} W^s(\theta_i) \tag{5.35}$$

This is proved in [57] as Theorem 3-2. Notice to prove this theorem it is assumed that the intersections of the stable and unstable manifolds of the equilibrium points on the stability boundary satisfy the transversality condition. This condition is considered to be a generic property of nonlinear dynamic systems [58].

The stability boundary of the gradient system (5.34) is defined as the Potential Energy Boundary Surface (PEBS) of the original system (5.24) or equivalently (5.33) [57]. Notice that PEBS is defined in the angle subspace of the original system.

Theorem 1 and 2 can be visualized from a three machine infinite bus example introduced in [59]. For the gradient system, the equipotential contours of the potential energy $V_{PE}(\theta)$, some trajectories and the stability boundary are plotted in Figure 5.2 taken from [59]. The stability boundary (also is the PEBS of the original system) is shown by the bold line and inside the stability boundary, trajectories converge to the asymptotically stable equilibrium point.

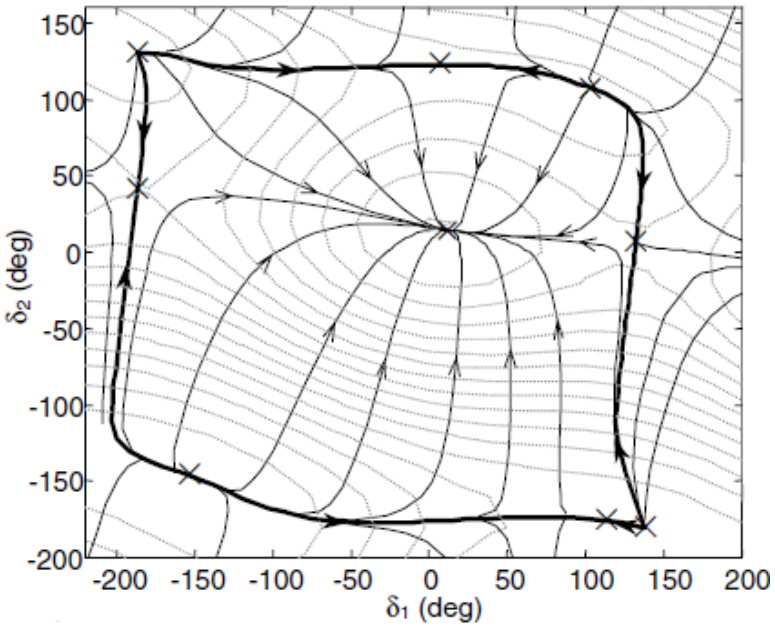

Figure 5.2 Phase portrait of the gradient system for a 3-machine system: Reprinted from [59]

5.3.1.2. Equilibrium Points Distribution in Multi-Machine System

As pointed out in [58], the equilibrium point and the stability region of the power system described in (5.24) is periodically repeated by a period of 2π in every angle coordinate. This point is well illustrated in Figure 5.3 taken from [56] which plots the equipotential contours of a three machine system.

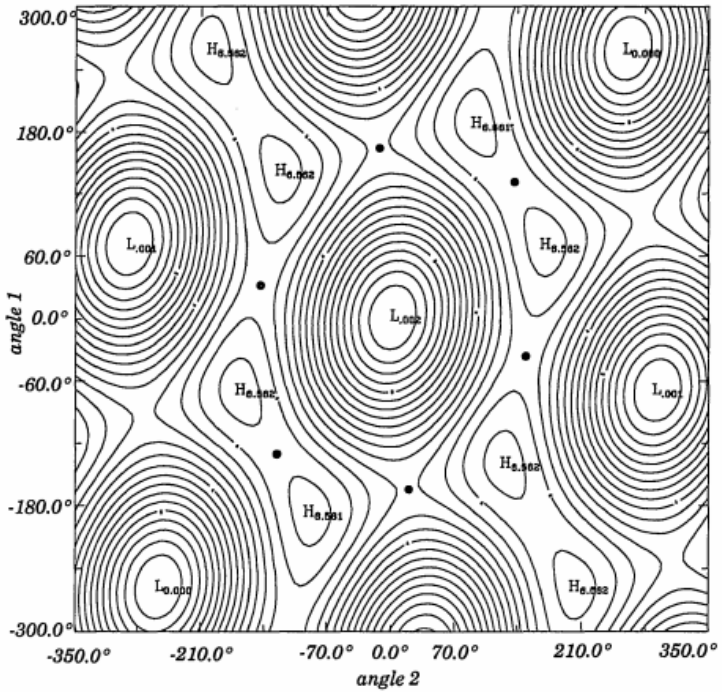

Figure 5.3 Equipotential contours of a three machine system: Reprinted from [56]

The L points are the local minimum in potential energy that corresponds to the stable equilibria and the H points are the local maximum in potential energy that corresponds to sources. The black dots surrounding the equilibria are saddle points. The stability boundary of a stable equilibrium in the gradient system is the union of all stable

manifolds of the unstable equilibria on the stability boundary, as shown in Figure 5.4 taken also from [56]. As can be seen, this pattern is repeated in the whole angle space.

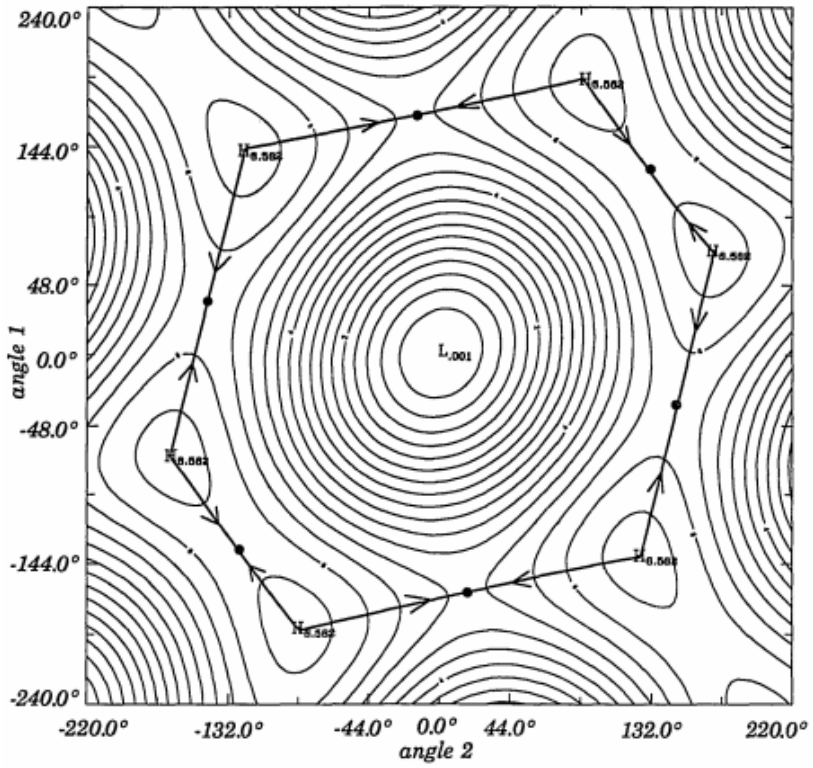

Figure 5.4 Equipotential contours with stability boundary: Reprinted from [56]

It is also worth pointing out that even though these alternate stable equilibria and stability regions are mathematically equivalent, to get from one to another requires pole slipping which will cause high currents like a short circuit and may trigger protective action [58]. Therefore, if the initial rotor angle states after a disturbance are within the potential energy boundary surface (PEBS) of a stable equilibrium point, the damping control should stabilize the system to that particular stable equilibrium point without causing any pole slipping.

5.3.2. Effectiveness of Damping Control in Transient Stability Improvement

In this section the effectiveness of damping control in transient stability improvement is proved in a multi-machine system.

Statement

Consider an n synchronous machine system with damping control whose dynamic equations in the COI reference frame are:

$$\begin{aligned} &\dot{\theta}_i = \tilde{\omega}_i \\ &M_i\dot{\tilde{\omega}}_i = P_i - P_{ei} - D_i\tilde{\omega}_i \qquad i = 1, 2, \cdots n \end{aligned} \tag{5.36}$$

Assume that:

1) A stable equilibrium point exists for the post disturbance system and the initial rotor angles after the disturbance are within the potential energy boundary surface (PEBS) of the stable equilibrium point.
2) Damping control is employed at every synchronous machine and the damping is distributed uniformly as in (5.23) with a sufficiently large μ.

Prove that:

After the disturbance (or a series of disturbances), the damping control can drive the system states to the stable equilibrium point.

Proof of the statement

When damping is sufficiently large, singular perturbation techniques can be employed to analyze the dynamics of (5.36).

Define the singular perturbation parameter

$$\varepsilon = \frac{1}{\mu} \tag{5.37}$$

The original system (5.36) can be rewritten as

$$\begin{aligned} \dot{\theta} &= \tilde{\omega} \\ \varepsilon I \dot{\tilde{\omega}} &= -\tilde{\omega} - D^{-1} \frac{\partial V_{PE}(\theta)}{\partial \theta} \end{aligned} \tag{5.38}$$

where the parameters are defined in the vector form as in (5.33)

Based on the assumptions, denote the initial condition after the disturbance as $\theta = \theta_0, \tilde{\omega} = \tilde{\omega}_0$ and θ_0 is inside the PEBS of a stable equilibrium point denoted as $\theta = \theta^s, \tilde{\omega} = 0$.

When damping is large, ε is small and (5.38) can be considered as a two time scale system with slow and fast dynamics. Following the procedure in [57], the rotor angle and rotor speed dynamics can be estimated using the singular perturbation techniques.

For consistency with the notation in [57] define

$$\begin{aligned} x &= \theta \\ y &= \tilde{\omega} \\ f(x) &= \frac{\partial V_{PE}(x)}{\partial x} \\ x_0 &= \theta_0;\ y_0 = \tilde{\omega}_0;\ x^s = \theta^s;\ y^s = 0 \end{aligned} \tag{5.39}$$

System in (5.38) is thus equivalently expressed as

$$\begin{aligned} \dot{x} &= y \\ \varepsilon I \dot{y} &= -y - D^{-1} f(x) \end{aligned} \tag{5.40}$$

with initial conditions $x(0) = x_0$, and $y(0) = y_0$.

The degenerate system, which is obtained by setting $\varepsilon = 0$, is

$$\begin{aligned} \dot{\bar{x}}(t) &= -D^{-1} f(\bar{x}) \qquad \bar{x}(0) = x_0 \\ \bar{y}(t) &= -D^{-1} f(\bar{x}) \end{aligned} \tag{5.41}$$

The boundary layer system of (5.40) can be obtained as follows:

(i) Introduce the time-scale variable $\tau = t/\varepsilon$ and the fast variables $\tilde{x}(\tau)$, $\tilde{y}(\tau)$ then

$$\begin{aligned} x(t) &= \bar{x}(t) + \tilde{x}(\tau) \\ y(t) &= \bar{y}(t) + \tilde{y}(\tau) \end{aligned} \tag{5.42}$$

(ii) Substitute (5.42) into (5.40) and set $\varepsilon = 0$, the boundary layer system is obtained as

$$\begin{aligned} \frac{d\tilde{x}}{d\tau} &= 0, \qquad \tilde{x}(0) = 0 \\ \frac{d\tilde{y}}{d\tau} &= -D(\tilde{y}(\tau)), \quad \tilde{y}(0) = y(0) + D^{-1} f(x_0) \end{aligned} \tag{5.43}$$

Then based on [57] and [60], there exists $\varepsilon_* > 0$ such that for all $\varepsilon < \varepsilon_*$ (5.40) has a unique solution

$$\begin{aligned} x(t) &= \bar{x}(t) + O(\varepsilon) \\ y(t) &= -D^{-1} f(\bar{x}(t)) + e^{-D\tau}\left(y_0 + D^{-1} f(x_0)\right) + O(\varepsilon) \end{aligned} \tag{5.44}$$

Based on Theorem IV.2 in [60], there exist ε sufficiently small such that the approximation error in (5.44) converge exponentially to zero as $t \to +\infty$.

Therefore, with ε sufficiently small, $(x(t), y(t))$ will converge to the stable equilibrium (x^s, y^s) if $\left(\bar{x}(t), -D^{-1} f(\bar{x}(t)) + e^{-D\tau}\left(y_0 + D^{-1} f(x_0)\right)\right)$ converges to (x^s, y^s) as $t \to +\infty$. It is easy to see that the fast dynamics $e^{-D\tau}\left(y_0 + D^{-1} f(x_0)\right)$ will approach zero as $t \to +\infty$ regardless of the initial condition. Therefore it is sufficient to show that $\left(\bar{x}(t), -D^{-1} f(\bar{x}(t))\right)$ approach zero as $t \to +\infty$.

Notice the slow dynamics in $\bar{x}(t)$ is described by $\dot{\bar{x}}(t) = -D^{-1} f(\bar{x})$ which is exactly the gradient system of (5.40). Based on Theorem 1 and Theorem 2, since the initial condition x_0 is inside the stability boundary of the gradient system associated with the equilibrium point $x = x^s$, $\bar{x}(t)$ will converges to the stable equilibrium point $x = x^s$ as $t \to +\infty$. As $\bar{x}(t)$ approaches x^s, $-D^{-1} f(\bar{x}(t))$ will approach $y^s = 0$ since $f(x^s) = 0$.

Since ε is reversely related to μ, ε can be made sufficiently small when each damping D_i is sufficiently large. Thus the statement is proved.

5.3.3. Estimate of the Minimum Required Damping in SMIB System

Section 5.3.2 proves the effectiveness of damping control assuming that the damping factors are sufficiently large. To gain a better understanding of the damping control, in this section, the minimum damping required to stabilize a SMIB system with a certain disturbance is estimated.

With reference to Figure 5.1, the post-disturbance SMIB system has a stable equilibrium at $\delta = \delta^s, \omega = 0$. The minimum damping required depends on the initial conditions after a disturbance. In this section, a case is considered where $\delta_0 \in (\delta^s, \delta^u); \omega_0 \in (0, +\infty)$. It means that the initial rotor angle is greater than δ^s and is moving toward δ^u right after the disturbance. Note that other cases can be similarly analyzed and are not illustrated here.

The SMIB system with damping has the dynamic equations

$$\begin{aligned} \dot{\delta} &= \omega \\ M\dot{\omega} &= P_m - P_e \sin\delta - D\omega \end{aligned} \tag{5.45}$$

To estimate the minimum damping, first ignore the $P_m - P_e \sin\delta$ term in (5.45) and the dynamic equations reduce to

$$\begin{aligned} \dot{\delta} &= \omega \\ \dot{\omega} &= -\frac{D}{M}\omega \end{aligned} \tag{5.46}$$

therefore

$$\omega - \omega_0 = -\frac{D}{M}\left(\delta - \delta_0\right) \tag{5.47}$$

With minimum damping factor D, the rotor speed reaches zero when the rotor angle equals δ^u. Therefore the minimum damping required D_{min} considering the simplified dynamic equations in (5.46) can be obtained as

$$D_{\min} = \frac{M\omega_0}{\delta^u - \delta_0} \tag{5.48}$$

Now consider the full dynamic equations in (5.45). Since $P_m - P_e \sin\delta$ is negative in the entire range (δ_0, δ^u), the effect of including this term is to make ω decrease faster and thus the maximum angle reached when $D = D_{min}$ is less than δ^u. Therefore, D_{min} is sufficient to stabilize the system with the given initial condition.

This can be illustrated as in Figure 5.5, which shows the phase portrait of the system. Given initial condition (δ_0, ω_0) that satisfy $\delta_0 \in (\delta^s, \delta^u); \omega_0 \in (0, +\infty)$, with the simplified dynamic equations in (5.46), the system states move from (δ_0, ω_0) to $(\delta_1, 0)$ follow the red line. This is indicated by the linear dependency between $\dot{\delta}$ and $\dot{\omega}$ in (5.46). With the full system dynamics, the system states will move from (δ_0, ω_0) to $(\delta_2, 0)$ and then converge to $(\delta^s, 0)$. As can be seen, δ_2 is always smaller than δ_1.

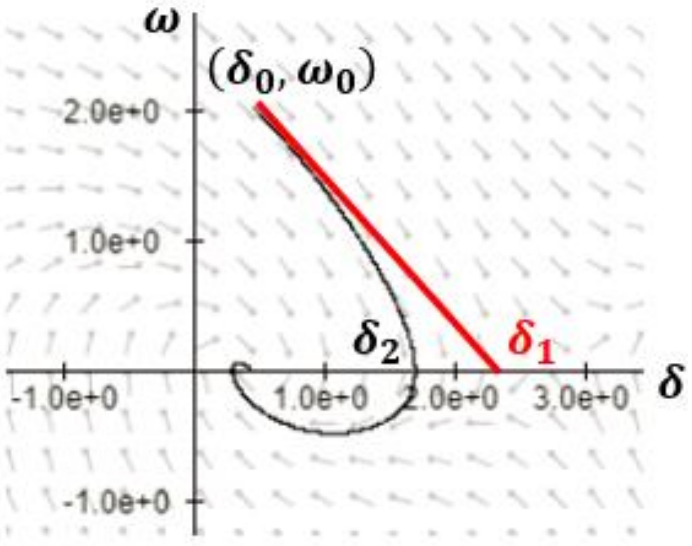

Figure 5.5 Phase portrait and illustrative trajectories

Therefore with the calculated D_{min} it is true that $\delta_2 < \delta_1 = \delta^u$ and D_{min} serves as a conservative estimate for the minimum required damping.

As can be seen from (5.47)(5.48), the minimum required damping will increase if the initial rotor speed is higher and/or if the initial rotor angle is closer to the unstable equilibrium point (or equivalently the PEBS).

Note that in a multi-machine system, when a critical or a cluster of critical machines exist, the system can be reduced to a SMIB system to analyze the minimum required damping. The more general cases requires future study.

5.4. Simulation Study

The proof in section 5.3.2 assumes strong conditions on the damping control. In practice, BESS may not be installed at every generator location thus the uniform damping condition may not hold and the damping factor D_i in the control design is restricted by the capacity of the BESS and cannot be made large without bound.

Therefore in this section, the performance of the two damping control schemes (i.e. local damping control and COI based damping control) are tested through simulation studies with practical considerations. Comparisons between the two control schemes are then made followed by discussions.

5.4.1. System Description

The system considered in the simulation study is the well-known Kundur two area system described in [35] on page 814 to 815. The system is developed in MATLAB/Simulink environment. The example file [61] provided by Mathworks contains the developed system in Simulink and is used with modifications. The system is shown in Figure 5.6, Figure 5.7 and Figure 5.8.

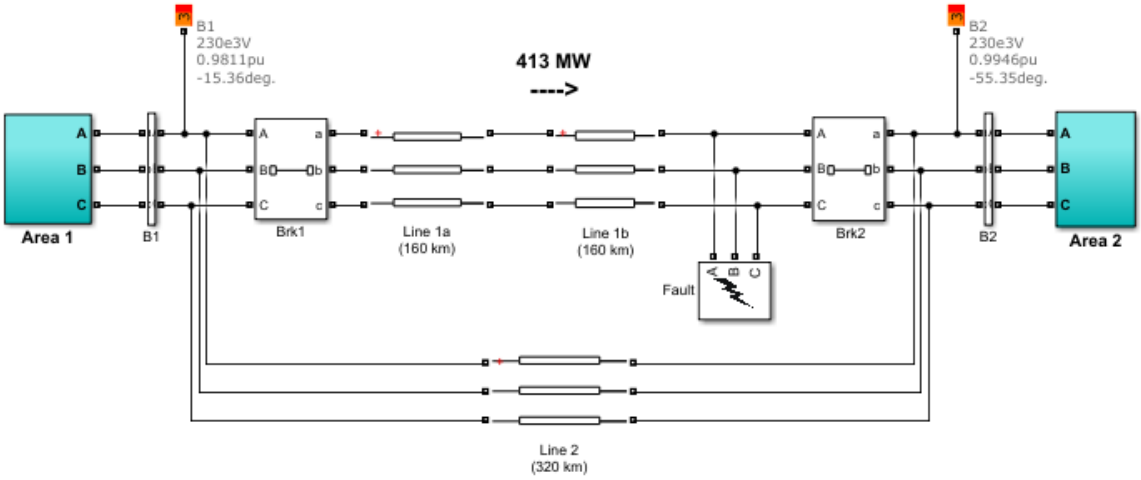

Figure 5.6 The studied two area system

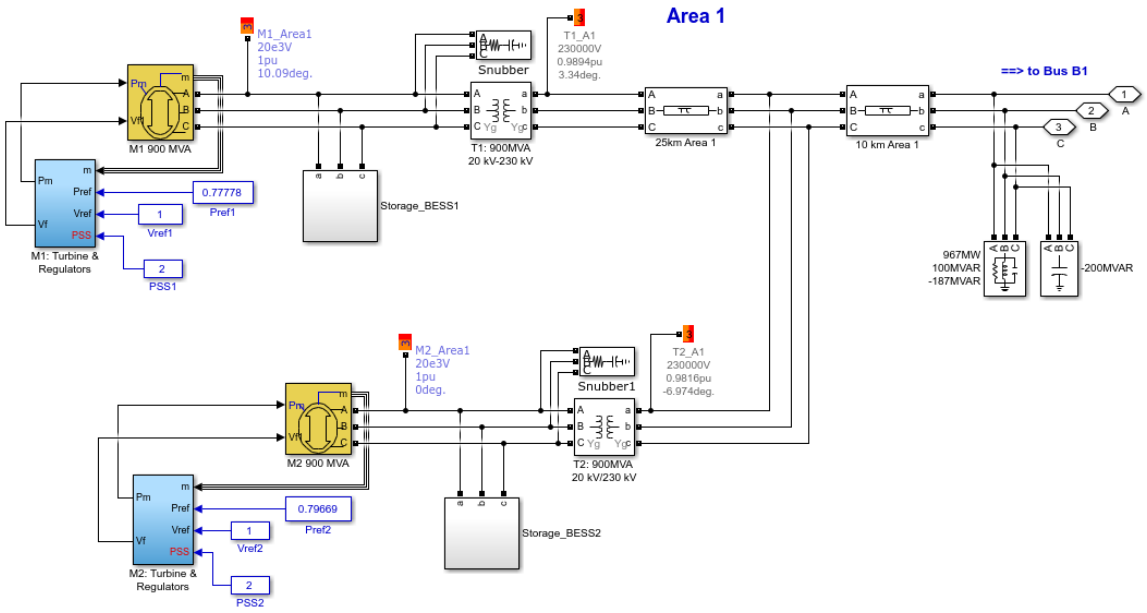

Figure 5.7 System layout inside Area 1

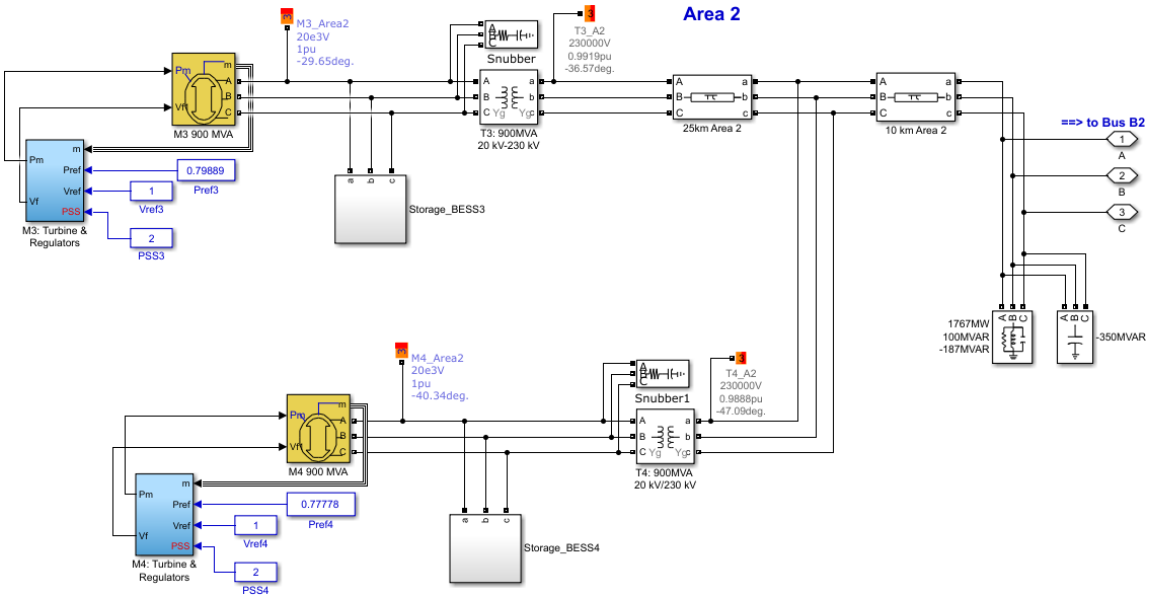

Figure 5.8 System layout inside Area 2

The following changes are made to the example file [61]:

1) The inertia time constant of generator 1 and 2 in area 1 is reduced from 6.5s to 4s while the inertia time constant of generator 3 and 4 in area 2 is reduced from 6.175s to 2s. The inertia are reduced so that the system is more prone to transient instability and thus the effects of damping controls are more obvious.
2) The length of the tie line connecting area 1 and area 2 is increased from 220km to 320km to represent a weaker system.
3) The Conventional Delta w PSS [62] is selected for every generator.
4) 4 BESS are added to the system, one at each generator terminal.

It should be emphasized that the synchronous generators in the system are modeled by the full 6 order dynamic model with the same dynamic parameters except for the inertia time constant. The same exciter, governor and PSS are applied for each generator. And the load is modeled as constant impedance in the simulation. Phasor based simulation is selected and the electromagnetic transients in the system are thus ignored. Notice that the simplification assumptions made in section 5.1.1 are removed except for the constant impedance. Therefore the performance of the damping control methods without the assumptions is tested.

Details of the BESS model are presented next. The BESS model developed is shown in Figure 5.9 through Figure 5.11. The BESS model is modeled as a controlled current source in the study.

As shown in Figure 5.9, voltage phasor at the storage terminal bus is measured and its magnitude and phase are used in the storage control together with the frequency

deviation signal Dfreq. The frequency deviation can be either local or with respect to COI depending on the control algorithm.

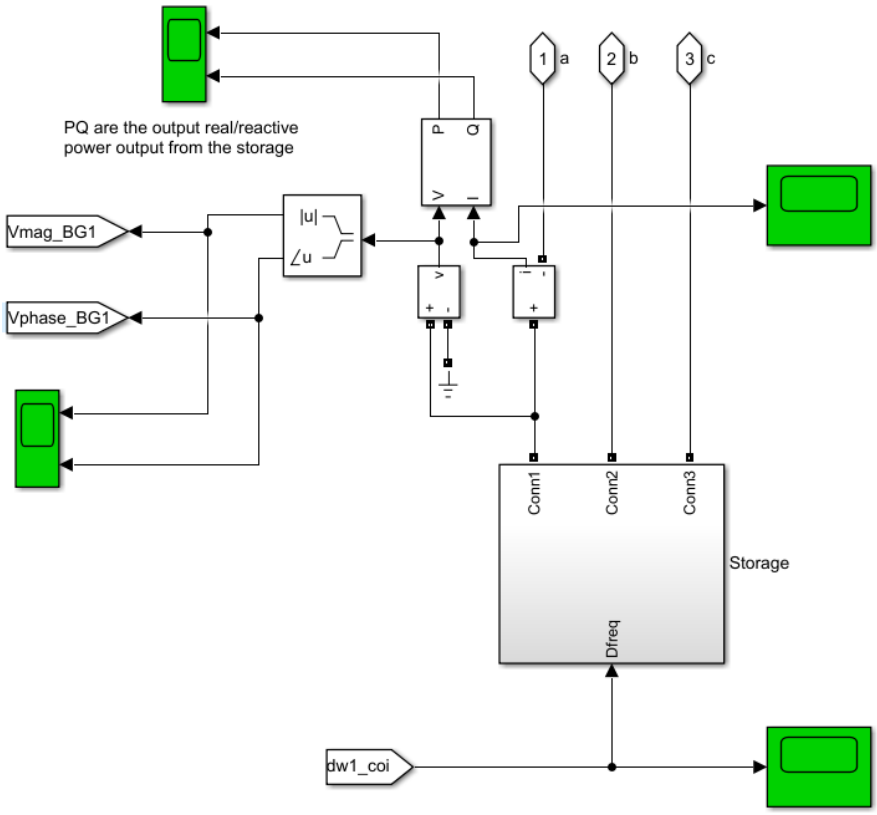

Figure 5.9 The developed BESS model

As shown in Figure 5.10, the voltage phase and magnitude as well as the frequency deviation signal are passed through a first order time delay block to model the measurement delays. The time constant for the delay block is set to 0.01s throughout the study. The frequency deviation is multiplied by the damping factor to produce the real power generation command Porder in p.u., whose magnitude is restricted by the limiter before passing to the actuator. The real power output limit of each BESS is set at 50MW

throughout the study. Since each generator generates around 700MW real power, the maximum real power output from the BESS is about 7% of the generator real power output.

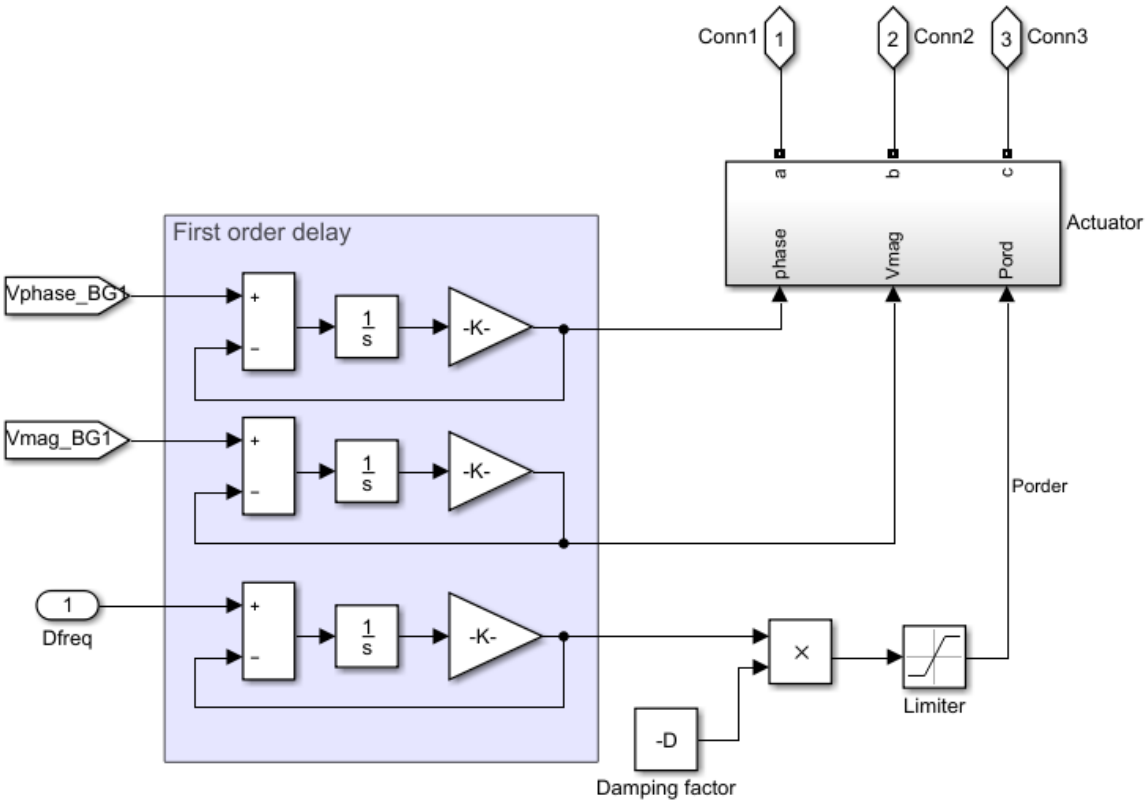

Figure 5.10 Real power output command generation

Inside of the actuator is shown in Figure 5.11. The real power output command together with the measured terminal voltage phasor are used to calculate the required current phasor to produce the desired real power. The current phasor is passed to the controlled current source to output. The switch controls when the storage outputs current

and power to the grid. The reactive power generation is designed to be zero by align the current phasor with the voltage phasor.

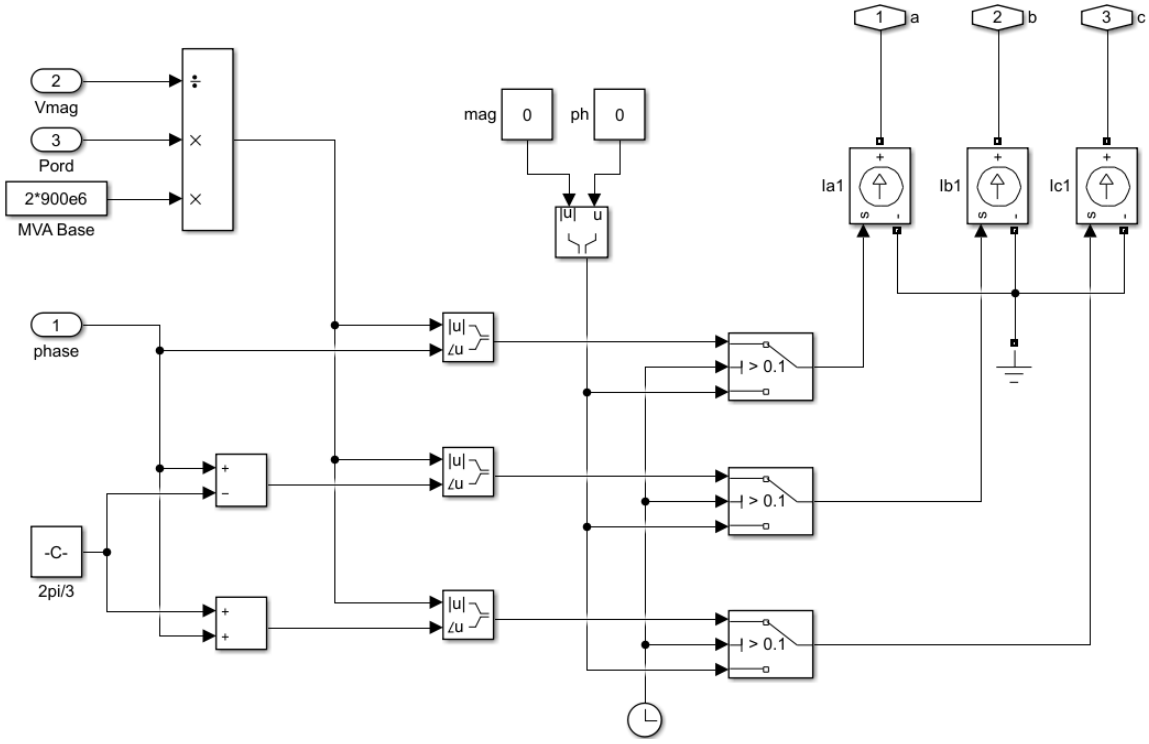

Figure 5.11 Controlled current source in the BESS model

5.4.2. Simulation Results

In this study, a solid three phase balanced fault is applied to the system and the critical clearing time (CCT) is obtained through dynamic simulation. The two damping control algorithms are compared for their ability to improve the transient stability of the system. For the same fault location, the control algorithm that results in a longer CCT is superior since the system can survive larger disturbance with it.

The following parameters are varied to thoroughly investigate the performance of the damping control methods:

1) Fault locations
2) Number and location of the active BESS units
3) Control parameters

5.4.2.1. Case Study I: Fault at Bus B1

In the first case study, a solid three phase fault is applied at bus B1 in Figure 5.6, which is the load bus in Area 1. To obtain the CCT, different fault duration is simulated with a step size of 1 cycle (0.0167s). For instance, if the CCT is found to be 5 cycle, it means the system is stable with a 5 cycle fault but will be unstable when it goes to 6 cycle. Notice the fault is cleared without any line tripping in the simulations and the BESS is active during and after the fault.

Denote the inertia time constants for the four synchronous generators as a vector $H = [H_1, H_2, H_3, H_4] = [4,4,2,2]$ and the damping factors for the four BESS as $D = [D_1, D_2, D_3, D_4]$. Recall that for local damping control the BESS at generator i regulates its real power output as $P_{BESSi} = D_i\omega_i$, where ω_i is the local rotor speed with respect to the synchronous speed. And for COI based damping control $P_{BESSi} = D_i\widetilde{\omega}_i$, where $\widetilde{\omega}_i$ is the local rotor speed with respect to the COI speed.

Following the proof in section 5.3.2, the case where all four BESS are active and provide uniform damping to the system is considered first. Thus D_i/H_i is the same for all the four storage units. The CCT results are shown in Table 5.1.

Table 5.1 CCT (4 BESS active, uniform damping)

	CCT (cycles)			
	Local Damping Control		COI Based Damping Control	
	With Limit	Without Limit	With Limit	Without Limit
D=[0,0,0,0]	11	11	11	11
D=[4,4,2,2]	14	15	14	14
D=[8,8,4,4]	13	19	18	18
D=[12,12,6,6]	13	23	21	22

In Table 5.1, $D = [0,0,0,0]$ refers to the case where all the BESS are inactive and it serves as the base case. As can be seen from the table, when output from the BESS is not limited, the two control methods result in close CCTs and the CCTs are improved with larger damping factors. This is in line with the theoretical study in section 5.2 since the system dynamic equations are the same with both control methods when the damping is distributed uniformly. However, an important observation is that when the 50MW real power output limit is applied to each storage unit, the local damping control can only improve the CCT by 3 cycles while the COI based method can improve the CCT by 10 cycles. This is due to the fact that local damping control in this case requires more real power output from the storage units and it quickly hit the limit when the damping factors are increased.

Since in practice the number and location of BESS are restricted, the case when BESS is only available and active in one of the two areas is studied next. The corresponding CCTs are listed in Table 5.2 and Table 5.3.

When 2 BESS are installed and active at the generator locations in Area 1, as shown in Table 5.2, the local damping control shows better performance when the limit is not applied but its performance becomes similar to the COI based damping control when the output limit is applied.

Compare Table 5.3 to Table 5.2, the COI based damping control is more effective when the BESS is installed in Area 2 whereas the local damping control is only effective when the BESS is installed in Area 1. In fact, when the BESS is installed in Area 2, with local damping control the transient stability of the system is deteriorated as the CCTs are reduced compared to the base case. This is a major drawback of the local damping control method. In power system the operating conditions and the location of the disturbance constantly changes and the available storage units for transient stability control may also change. It is therefore important to guarantee that each storage unit in the system, when activated for the damping control, contributes positively to the transient stability regardless of system operating conditions and disturbance locations.

Table 5.2 CCT (2 BESS active in Area 1)

	CCT (cycles)			
	Local Damping Control		COI Based Damping Control	
	With Limit	Without Limit	With Limit	Without Limit
D=[0,0,0,0]	11	11	11	11
D=[4,4,0,0]	14	16	12	12
D=[8,8,0,0]	14	16	13	13
D=[12,12,0,0]	14	20	14	15

Table 5.3 CCT (2 BESS active in Area 2)

	CCT (cycles)			
	Local Damping Control		COI Based Damping Control	
	With Limit	Without Limit	With Limit	Without Limit
D=[0,0,0,0]	11	11	11	11
D=[0,0,2,2]	9	9	13	13
D=[0,0,4,4]	8	8	15	15
D=[0,0,6,6]	7	6	17	18

To understand why local damping control can fail, refer back to (5.26) where it is shown that the derivative of the transient energy function is $-D_i\omega_i\tilde{\omega}_i$ and is sign indefinite.

Notice $P_{BESSi} = D_i\omega_i$ is the real power output from storage unit i. Therefore, the output of storage unit i can either dissipate system transient energy and improve the transient stability when $-D_i\omega_i\tilde{\omega}_i$ is negative or it can inject transient energy to the system and deteriorate the transient stability when $-D_i\omega_i\tilde{\omega}_i$ is positive.

As an illustration, the derivative of the transient energy function when BESS are active at generator 3 and 4 in Area 2 is plotted in Figure 5.12. In this case $\dot{V} = -D_3\omega_3\tilde{\omega}_3 - D_4\omega_4\tilde{\omega}_4$ and $D_3 = D_4 = 6$. This corresponds to the last row in Table 5.6. The fault is applied at $t = 2s$ and is cleared after 7 cycles. The relative rotor angle between generator 1 and generator 4 is also plotted in Figure 5.13.

As can be seen, the derivative is positive from 2s to 2.75s and the angle swing between generator 1 and generator 4 reaches its peak around $t = 2.75s$. Therefore, the local damping control in Area 2 actually injects transient energy to the system during the first swing and the transient stability is deteriorated as a result. This demonstrates that due to the sign indefiniteness of $-D_i\omega_i\tilde{\omega}_i$, local damping control can affect the transient stability adversely.

On the other hand, the COI based damping control always dissipate transient energy since the derivative of the transient energy function is $-D_i\tilde{\omega}_i^2$ as shown in (5.30). Therefore it is guaranteed that the COI based damping control can improve system transient stability regardless of the BESS location, even though BESS at different locations may improve the transient stability in different degrees. This point is supported by the results shown in Table 5.2 and Table 5.3.

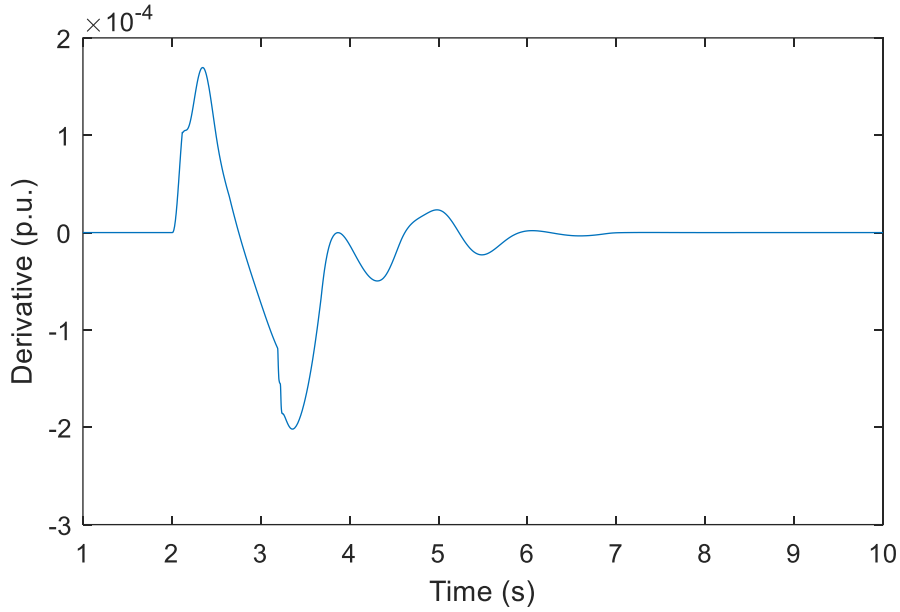

Figure 5.12 Derivative of the transient energy function

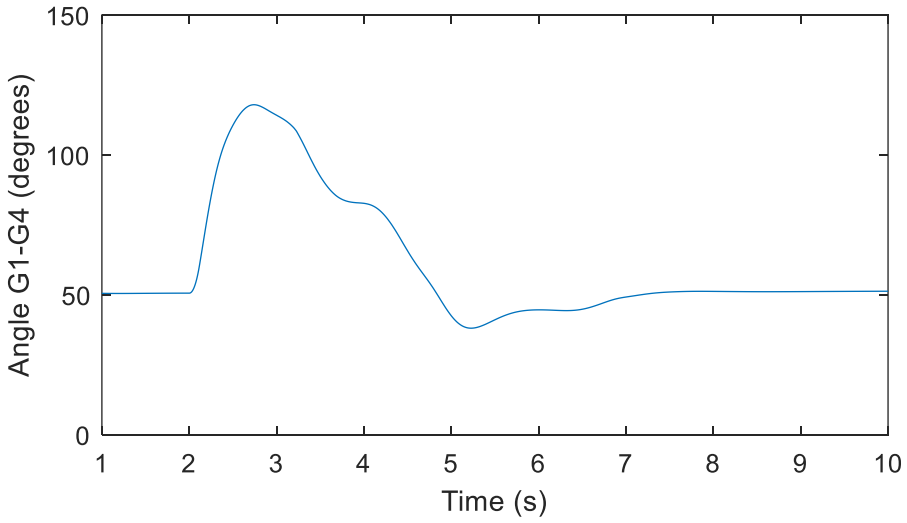

Figure 5.13 Relative rotor angle between generator 1 and 4

In the above explanation, the transient energy is defined in the COI reference frame. As mentioned in section 5.1.2, transient energy defined in the COI reference frame

contains energy from the relative motion only and is suitable for transient stability study. It is interesting to notice that if synchronous reference frame is used instead, the transient energy dissipation rate with local damping control is simply $-D_i\omega_i^2$ and is always negative when ω_i is different from the synchronous speed. Therefore, the adverse effect of local damping control on transient stability cannot be revealed and understood in synchronous reference frame since relative motion and COI motion are considered together. Indeed, even if the relative motion energy is increasing (which deteriorates transient stability), the total transient energy measured in the synchronous frame can still decrease if the COI energy decreases faster, which applies to the cases in Table 5.3.

5.4.2.2. Case Study II: Fault at Bus B2

In the second case study, a solid three phase fault is applied at bus B2 in Figure 5.6, which is the load bus in Area 2. All the other conditions remain the same as in case study I. The purpose of this case study is to test the ability of the damping control algorithms to deal with different disturbances.

The results with uniform damping distribution are shown in Table 5.4. The cases where BESS is only installed in Area 1 and Area 2 are shown in Table 5.5 and Table 5.6 , respectively.

Table 5.4 CCT (4 BESS active, uniform damping)

	CCT (cycles)			
	Local Damping Control		COI Based Damping Control	
	With Limit	Without Limit	With Limit	Without Limit
D=[0,0,0,0]	5	5	5	5
D=[4,4,2,2]	8	8	8	8
D=[8,8,4,4]	11	13	11	12
D=[12,12,6,6]	12	17	12	16

Table 5.5 CCT (2 BESS active in Area 1)

	CCT (cycles)			
	Local Damping Control		COI Based Damping Control	
	With Limit	Without Limit	With Limit	Without Limit
D=[0,0,0,0]	5	5	5	5
D=[4,4,0,0]	6	6	6	6
D=[8,8,0,0]	6	6	7	7
D=[12,12,0,0]	6	6	7	8

Table 5.6 CCT (2 BESS active in Area 2)

	CCT (cycles)			
	Local Damping Control		COI Based Damping Control	
	With Limit	Without Limit	With Limit	Without Limit
D=[0,0,0,0]	5	5	5	5
D=[0,0,2,2]	7	7	7	7
D=[0,0,4,4]	8	8	10	10
D=[0,0,6,6]	9	10	10	13

As can be seen, in this case, when the storage output limit is in place, the performance of the two damping control methods are quite comparable with the COI based control showing slight advantage when BESS is only active in Area 1 or 2. Another observation is that unlike the previous case, BESS in both areas contribute positively to system transient stability when local damping control is applied. Also, with local damping control, the BESS in Area 2 can improve the CCT better than the BESS in Area 1. This is very different from the previous case where the BESS in Area 2 actually affect the transient stability adversely.

With COI based damping control, however, the BESS in Area 2 is more effective in improving transient stability in both cases. This is possibly due to the fact that Area 2 has smaller inertia and the COI based damping control can always drive this small inertia to approach the speed of the larger inertia more effectively. This is another advantage of

the COI based control since it gives guidance on where to install the BESS and the installed BESS can be effective for disturbances at various locations in the system. It is interesting to notice that the work in [63] also shows that adding damping in low inertia areas is beneficial to power system small signal oscillations.

6. CONCLUSIONS

6.1. Conclusions

The conclusions of this dissertation are organized based on sections.

In section 2 the impact of CBGs on power system small signal stability is investigated. An oscillation mode originated from the reactive power/voltage control loop of the CBG is analyzed using damping torque analysis. Damping of the oscillation mode is found to be sensitive to system operating conditions and the line impedance outside the CBG. It is shown that its dynamic coupling with the SG electromechanical oscillation mode can be explained based on the mode coupling theory. When the oscillation mode from the CBG has similar frequency as the inter area mode, the CBG dynamics have high influence on power system inter-area oscillations through mode coupling. Otherwise the CBGs have little dynamic interaction with the SGs. It should be noticed that this analysis is valid for CBGs that are synchronized with the grid through fast PLLs and are working in the grid-following mode.

In section 3, the limitations of the positive sequence model for CBGs are revealed through simulation study. Transient stability mechanism of the CBGs is then analyzed based on mathematical analogy with the SG swing equations. Subsequently, a novel method to evaluate the transient stability margin of the CBGs considering detailed control loops is proposed. The proposed index can be obtained analytically without running dynamic simulations. The advantage of the proposed method over the short circuit ratio (SCR) based method in evaluating the transient stability margin of the CBGs is shown.

Section 4 investigate the impact of TTC on power system stability. Firstly, the impact of TTC on system transient stability margin is discussed. It is shown that properly designed TTC can improve system transient stability margin with less transmission resource. The impact of TTC on power system small signal stability is then investigated in a traditional power system considering different loading levels. Renewable integration is then considered and the impact of TTC on power system small signal stability as well as nonlinear oscillations is investigated. It is shown that TTC can trigger both small signal and nonlinear oscillations in the system. Measures to improve power system small signal stability to better accommodate the TTC actions are discussed and a simulation based method is proposed to assess system overall stability after a TTC action.

Section 5 proposes a novel wide area control method to improve system transient stability. The control algorithm uses SG rotor speeds relative to the center of inertia as feedback signals. The proposed method does not require knowledge of the system model or the post-disturbance steady state information. It is proved theoretically that the proposed control method can stabilize the system given certain conditions. Its effectiveness and advantage over a local damping control method is demonstrated through simulation studies.

6.2. Future Works

Future works related to the research in this dissertation are suggested in this section.

6.2.1. Transient stability of CBGs

Transient stability of CBGs is analyzed in this research ignoring the dynamic interaction between CBGs and SGs. This simplifies the analysis but may cause errors in evaluating the transient stability for CBGs. Future research is suggested to investigate the influence of dynamic interaction between CBGs and SGs on transient stability of CBGs.

Also, in the current research a group of CBGs can be considered together taking into account the dynamic interactions among them only if they are connected in parallel. Future research is needed to deal with the more general connection scenarios.

Influence of the CBG dynamics on SG transient stability can also be studied.

6.2.2. Control design for BESS

This research demonstrates that the proposed control algorithm is effective in improving power system transient stability. In section 5.3.3, the minimum required damping to stabilize the system is estimated in a SMIB system, future research should explore means to estimate the required damping in general multi-machine systems.

Besides, more research is needed to study the optimal locations for the BESS if the number of BESS is restricted and less than the number of SGs in the system. Moreover, the effect of communication delay and communication failure on the proposed method can be analyzed.

Future work should also consider the dynamics from the CBGs and further evaluate the effectiveness of the proposed damping control algorithm. The use of CBGs as actuators to provide damping control can also be investigated. The impact of the proposed control on power system oscillations is another interesting topic.

REFERENCES

[1] “Integrating Variable Energy Resources into Weak Power Systems”, NERC Reliability Guideline, June 2017.

[2] J. Aho, M. Amin, A. M. Annaswamy, G. Arnold, A. Buckspan, A. Cadena, D. Callaway, E. Camacho, M. Caramanis, A. Chakrabortty et al., “Smart grid research: Control systems-IEEE vision for smart grid controls: 2030 and beyond,” 2013.

[3] E. B. Fisher, R. P. O’Neill, and M. C. Ferris, “Optimal transmission switching,” IEEE Trans. Power Syst., vol. 23, no. 3, pp. 1346-1355, Aug. 2008.

[4] K.W. Hedman, M.C. Ferris, R.P. O’Neill, E.B. Fisher, S.S. Oren, “Co-optimization of generation unit commitment and transmission switching with N-1 reliability”, IEEE Trans. Power Syst. 25 (2010) 1052–1063.

[5] W. Shao, V. Vittal, “Corrective switching algorithm for relieving overloads and voltage violations”, IEEE Trans. Power Syst. 20 (2005) 1877–1885.

[6] A.R. Escobedo, E. Moreno-Centeno, K.W. Hedman, “Topology control for load shed recovery”, IEEE Trans. Power Syst. 29 (2014) 908–916.

[7] D. Gautam, V. Vittal and T. Harbour, "Impact of Increased Penetration of DFIG-Based Wind Turbine Generators on Transient and Small Signal Stability of Power Systems," in *IEEE Transactions on Power Systems*, vol. 24, no. 3, pp. 1426-1434, Aug. 2009.

[8] J. G. Slootweg and W. L. Kling, “The impact of large scale wind power generation on power system oscillations,” Elect. Power Syst. Res., vol. 67, no. 1, pp. 9–20, Oct. 2003.

[9] J. J. Sanchez-Gasca, N. W. Miller, and W. W. Price, “A modal analysis of a two-area system with significant wind power penetration,” in Proc. Power Syst. Conf. Expo., 2004.

[10] L. P. Kunjumuhammed, B. C. Pal, K. K. Anaparthi, and N. F. Thornhill, “Effect of wind penetration on power system stability,” in Proc. IEEE Power and Energy Soc. General Meeting (PES), Vancouver, BC, Canada, Jul. 2013, pp. 1–5.

[11] H. A. Pulgar-Painemal and P. W. Sauer, “Power system modal analysis considering doubly-fed induction generators,” in Proc. IREP Symp. —Bulk Power System Dynamics and Control, Brazil, 2010.

[12] S. Jiaying and S. Chen, "Impact of DFIG wind power on power system small signal stability," in Innovative Smart Grid Technologies (ISGT), 2013 IEEE PES, Washington, DC, 2013, pp. 1-6.

[13] W. Du, J. Bi, J. Cao and H. F. Wang, "A Method to Examine the Impact of Grid Connection of the DFIGs on Power System Electromechanical Oscillation Modes," in IEEE Transactions on Power Systems, vol. 31, no. 5, pp. 3775-3784, Sept. 2016.

[14] G. Tsourakis, B. Nomikos, and C. Vournas, “Effect of wind parks with doubly fed asynchronous generators on small-signal stability,” in *Electr. Power Syst. Res.*, vol. 79, no. 1, pp. 190–200, 2009.

[15] L. Fan, Z. Miao, and D. Osborn, “Impact of doubly fed wind turbine generation on inter-area oscillation damping,” in *Proc. IEEE Power Eng. Soc. Gen. Meeting*, 2008, pp. 1–8.

[16] J. Quintero, V. Vittal, G. T. Heydt and H. Zhang, "The Impact of Increased Penetration of Converter Control-Based Generators on Power System Modes of Oscillation," in *IEEE Transactions on Power Systems*, vol. 29, no. 5, pp. 2248-2256, Sept. 2014.

[17] S. Ma, H. Geng, L. Liu, G. Yang and B. C. Pal, "Grid-Synchronization Stability Improvement of Large Scale Wind Farm During Severe Grid Fault," in *IEEE Transactions on Power Systems*, vol. 33, no. 1, pp. 216-226, Jan. 2018.

[18] I. Erlich et al., "Effect of wind turbine output current during faults on grid voltage and the transient stability of wind parks," *2009 IEEE Power and Energy Society General Meeting*, Calgary, AB, 2009, pp. 1-8.

[19] B. Weise, "Impact of K-factor and active current reduction during faultride-through of generating units connected via voltage-sourced converters on power system stability," *IET Renew. Power Generation*, vol. 9, no. 1, pp. 25–36, Jan. 2015.

[20] Ö. Göksu, R. Teodorescu, C. L. Bak, F. Iov and P. C. Kjær, "Instability of Wind Turbine Converters During Current Injection to Low Voltage Grid Faults and PLL Frequency Based Stability Solution," in *IEEE Transactions on Power Systems*, vol. 29, no. 4, pp. 1683-1691, July 2014.

[21] A. T. Saric and A. M. Stankovic, "Rapid small-signal stability assessment and enhancement following changes in topology," IEEE Trans. Power Syst., vol. 30, no. 3, pp. 1155–1163, May, 2015.

[22] Y. Chen et al. “The influence of topology changes on inter-area oscillation modes and mode shapes,” in Proc. IEEE PES General Meeting, San Diego, CA, July 2011, pp. 1–7.

[23] Y. Zhu, C. Liu, K. Sun, D. Shi and Z. Wang, "Optimization of Battery Energy Storage to Improve Power System Oscillation Damping," in *IEEE Transactions on Sustainable Energy*.

[24] B. C. Pal, et al, “Robust damping controller design in power systems with superconducting magnetic energy storage devices,” *IEEE Trans. Power Syst.*, vol. 15, no. 1, pp. 320-325, Feb 2000.

[25] B. C. Pal, A. H. Coonick, I. M. Jaimoukha, H. El-Zobaidi, “A Linear Matrix Inequality Approach to Robust Damping Control Design in Power Systems with Superconducting Magnetic Energy Storage Device,” *IEEE Trans. Power Syst.*, vol. 15, no. 1, pp. 356-362, Feb 2000

[26] M. Beza, M. Bongiorno, “An Adaptive Power Oscillation Damping Controller by STATCOM With Energy Storage,” *IEEE Trans. Power Syst.*, vol. 30, no. 1, pp. 484-493, Jan. 2015.

[27] A. Kanchanaharuthai, V. Chankong and K. A. Loparo, “Transient Stability and Voltage Regulation in Multimachine Power Systems Vis-à-Vis STATCOM and Battery Energy Storage,” *IEEE Trans. Power Syst.*, vol. 30, no. 5, pp. 2404-2416, Sept. 2015.

[28] M. Ayar, S. Obuz, R. D. Trevizan, A. S. Bretas and H. A. Latchman, "A Distributed Control Approach for Enhancing Smart Grid Transient Stability and Resilience," in *IEEE Transactions on Smart Grid*, vol. 8, no. 6, pp. 3035-3044, Nov. 2017.

[29] A. Farraj, E. Hammad and D. Kundur, "On the Use of Energy Storage Systems and Linear Feedback Optimal Control for Transient Stability," in *IEEE Transactions on Industrial Informatics*, vol. 13, no. 4, pp. 1575-1585, Aug. 2017.

[30] G. Tsourakis, B. Nomikos, and C. Vournas, "Effect of wind parks with doubly fed asynchronous generators on small-signal stability," in *Electr. Power Syst. Res.*, vol. 79, no. 1, pp. 190–200, 2009.

[31] CIRGE Technical Brochure 328, Modeling and dynamic behavior of wind generation as it relates to power system control and dynamic performance, August 2007, CIRGE WG C4.601. (www.e-cigre.org)

[32] S-H. Huang et al. "Voltage Control Challenges on Weak Grids with High Penetration of Wind Generation: ERCOT Experience," in *Proc. IEEE PES General Meeting*, San Diego, CA, July 2012, pp. 1–7.

[33] I. Dobson, J. Zhang, S. Greene, H. Engdahl, and P. W. Sauer, "Is strong resonance a precursor to power system oscillations?," in *IEEE Trans. Circuits Syst. I, Fundam. Theory Appl.*, vol. 48, no. 3, pp. 340–349, Mar. 2001.

[34] K. R. Padiyar and H. V. SaiKumar, "Investigations on strong resonance in multimachine power systems with STATCOM supplementary modulation controller," in *IEEE Transactions on Power Systems*, vol. 21, no. 2, pp. 754-762, May 2006.

[35] P. Kundur, Power System Stability and Control. New York, NY, USA: McGraw-Hill, 1994.

[36] "Deploying Utility-Scale PV Power Plants in Weak Grids", First Solar, *2017 IEEE PES General Meeting*, Chicago, IL, July 2017.

[37] J. Z. Zhou, H. Ding, S. Fan, Y. Zhang and A. M. Gole, "Impact of Short-Circuit Ratio and Phase-Locked-Loop Parameters on the Small-Signal Behavior of a VSC-HVDC Converter," in *IEEE Transactions on Power Delivery*, vol. 29, no. 5, pp. 2287-2296, Oct. 2014.

[38] W. Wang and G. M. Huang, "Impacts of DFIG reactive power/voltage control on power system oscillations through mode coupling," *2017 IEEE Power and Energy Society General Meeting*, Chicago, IL, 2017, pp. 1-5.

[39] W. Wang and G. M. Huang, "Impacts of smart grid topology control on power system stability with renewable integration," *2016 North American Power Symposium (NAPS)*, Denver, CO, 2016, pp. 1-6.

[40] J. Hu, Q. Hu, B. Wang, H. Tang and Y. Chi, "Small Signal Instability of PLL-Synchronized Type-4 Wind Turbines Connected to High-Impedance AC Grid During LVRT," in *IEEE Transactions on Energy Conversion*, vol. 31, no. 4, pp. 1676-1687, Dec. 2016.

[41] W. Wang et al., "Instability of PLL-Synchronized Converter-Based Generators in Low Short-Circuit Systems and the Limitations of Positive Sequence Modeling," *2018 North American Power Symposium (NAPS)*, Fargo, ND, 2018.

[42] "Large-Scale Integration of Wind Plants in Weak Networks: The ERCOT Experience", ERCOT, *2017 IEEE PES General Meeting*, Chicago, IL, July 2017.

[43] Model User Guide for Generic Renewable Energy System Models. EPRI, Palo Alto, CA: 2015. 3002006525.

[44] H. Wu and X. Wang, "Transient angle stability analysis of grid-connected converters with the first-order active power loop," *2018 IEEE Applied Power Electronics Conference and Exposition (APEC)*, San Antonio, TX, USA, 2018, pp. 3011-3016.

[45] James K. Robinson, "Power System Stability-Computation of Critical Clearing Time and Stability Margin Index", Master of Science Thesis, Department of Electrical Engineering, Lehigh University, Bethlehem, Pennsylvania, USA, 1976.

[46] S. R. Sanders, J. M. Noworolski, X. Z. Liu, and G. C. Verghese, "Generalized averaging method for power conversion circuits," *IEEE Trans. on Power Electron*, vol. 6, no. 2, pp. 251–259, Apr. 1991.

[47] Y. Zhang, S. H. F. Huang, J. Schmall, J. Conto, J. Billo and E. Rehman, "Evaluating system strength for large-scale wind plant integration," *2014 IEEE Power and Energy Society General Meeting*, National Harbor, MD, 2014, pp. 1-5

[48] Power System Test Case Archive, Univ. Washington, Dept. Elect. Eng., 2007. [Online]. Available: https://www.ee.washington.edu/research/pstca/index.html.

[49] G. M. Huang, W. Wang, and J. An, “Stability issues of smart grid transmission line switching,” in Proc. 19th IFAC World Congr., Cape Town, South Africa, Aug. 2014, pp. 7305–7310.

[50] Tian Lan, Garng. M. Huang. “Transmission line switching in power system planning with large scale renewable energy,” in 2015 First Workshop on Smart Grid and Renewable Energy (SGRE), Doha, pp. 1-6, Mar. 22-23, 2015.

[51] Transient Security Assessment Tool User Manual, Powertech Labs, Inc.

[52] Reliability Standards for the New England Area Bulk Power Supply System, [Online]. Available: http://www.iso-ne.com/rules_proceds/isone_plan/pp03/pp3_final.pdf.

[53] M. A. Pai, Energy Function Analysis for Power System Stability. Norwell, MA: Kluwer, 1989.

[54] T. Athay, R. Podmore and S. Virmani, "A Practical Method for the Direct Analysis of Transient Stability," in *IEEE Transactions on Power Apparatus and Systems*, vol. PAS-98, no. 2, pp. 573-584, March 1979.

[55] Y. Zhu, C. Liu, B. Wang, K. Sun, “Damping Control for a Target Oscillation Mode Using Battery Energy Storage,” *Journal of Modern Power Systems and Clean Energy*, 2018 [Online]. Available: https://doi.org/10.1007/s40565-017-0371-3

[56] R. T. Treinen, V. Vittal, and W. Kliemann, “An Improved Technique to Determine the Controlling Unstable Equilibrium Point in a Power System,” IEEE Trans. Circuit and Systems, Vol.43, No.4, pp.313-323, 1996.

[57] Chiang, H. D., F. F. Wu, and P. P. Varaiya. "Foundations of the Potential Energy Boundary Surface Method for Power System Transient Stability Analysis." *IEEE Transactions on Circuits and Systems,* Vol. CAS-35, No. 6 (June 1988); 712-728.

[58] J. Zaborszky, G. Huang, B. Zheng and T. -. Leung, "On the phase portrait of a class of large nonlinear dynamic systems such as the power system," in *IEEE Transactions on Automatic Control*, vol. 33, no. 1, pp. 4-15, Jan. 1988.

[59] J. T. Scruggs and L. Mili, "Dynamic gradient method for PEBS detection in power system transient stability assessment," International Journal of Electrical Power & Energy Systems, vol. 23, pp. 155-165, 2/1/ 2001.

[60] F. Dörfler and F. Bullo, "Synchronization and transient stability in power networks and non-uniform Kuramoto oscillators," *Proceedings of the 2010 American Control Conference*, Baltimore, MD, 2010, pp. 930-937.

[61] “Performance of Three PSS for Interarea Oscillations” [Online]. Available: https://www.mathworks.com/help/physmod/sps/examples/performance-of-three-pss-for-interarea-oscillations.html.

[62] M. Klein, G. J. Rogers, S. Moorty and P. Kundur, "Analytical investigation of factors influencing power system stabilizers performance," in *IEEE Transactions on Energy Conversion*, vol. 7, no. 3, pp. 382-390, Sept. 1992.

[63] H. Pulgar-Painemal, Y. Wang and H. Silva-Saravia, "On Inertia Distribution, Inter-Area Oscillations and Location of Electronically-Interfaced Resources," in *IEEE Transactions on Power Systems*, vol. 33, no. 1, pp. 995-1003, Jan. 2018.

APPENDIX

To further demonstrate the effectiveness of the proposed method in section 3.6 to obtain CCT analytically and the usefulness of the stability margin index, a different operating condition is considered where the real power generation amount of each WTG in the AEP system is reduced by half. The total real power generation by the WTGs is reduced from 664.9 MW to 332.4 MW while the real power load in the system stays unchanged at 241.4 MW. Consequently, the real power exported to the external system is reduced from 393.4 MW to 82.9 MW. The new generation amounts for the WTGs are shown in Table 1.

Table 1 SCRs at different WTG locations

WTG No.	MVA	PGen (MW)	QGen (MVar)
1	193.98	78.50	0.051
2	8.40	3.75	-1.22
3	25.20	11.25	-4.45
4	25.20	11.20	-5.36
5	125.00	33.00	-10.81
6	117.00	34.75	-7.45
7	166.50	67.50	-15.67
8	166.50	67.50	-2.12
9	66.50	25.00	-3.45

To begin with, the base case control parameters shown in Table 3.2 are used for each WTG. The calculated CCTs and stability margin indices are compared with the simulated ones in Table 2. As can be seen, with the new system operating condition, the calculated CCTs and transient stability margin indices are again very close to the

simulated ones. Moreover, transient stability margins for the WTGs are improved as the real power generation is reduced, which is in line with the analysis in section 3.7. The updated WSCRs are also shown in Table 2. Compared to the WSCRs in Table 3.3, the WSCRs are doubled uniformly for the WTG locations under the new operating condition due to the halved real power generation amount. However, the transient stability margins increase to different extents at different WTG locations. Therefore, the WSCR index is not able to accurately quantify the improvement in transient stability margins of the WTGs.

Table 2 CCT and S_m for WTGs with reduced generation amounts

	CCT_S (s)	CCT_C (s)	Error (%)	$S_{m\_}S$	$S_{m\_}C$	WSCR
WTG 9	0.0690	0.07	1.45	-31.0	-30.0	3.56
WTG 5	0.1220	0.1164	-4.59	22.0	16.4	10.88
WTG 6	0.1245	0.1204	-3.29	24.5	20.4	9.53
Group 2	0.1305	0.1267	-2.91	30.5	26.7	3.30
Group 1	0.1302	0.1246	-4.30	30.2	24.6	3.63

The time domain response of WTG 7 and WTG 8 inside Group 2 following the fault is plotted in Figure 1 and Figure 2. The blue curve shows the response when the fault is cleared 0.003s before the CCT and the red curve 0.003s after the CCT. As can be seen, in this case both WTGs become unstable when the fault is cleared after the CCT.

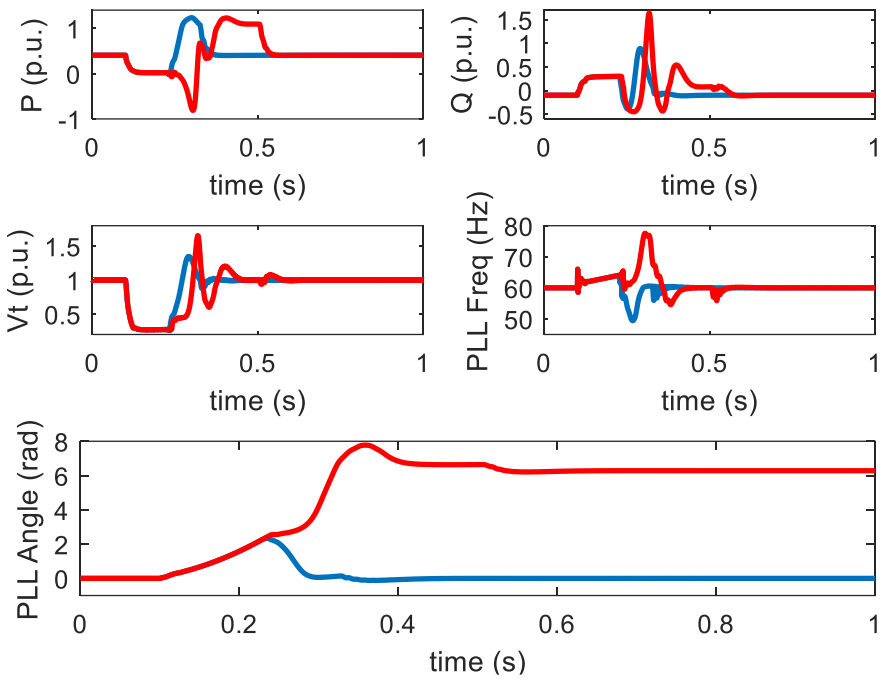

Figure 1 Response of WTG 7 with base case control parameters. (blue curve: fault duration 0.1275s, stable; red curve: fault duration 0.1335s, unstable)

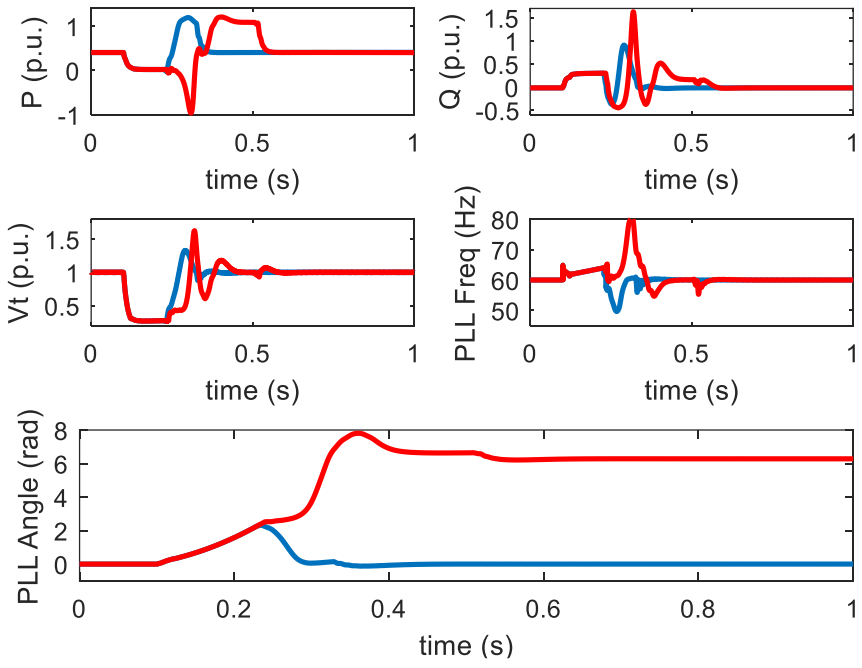

Figure 2 Response of WTG 8 with base case control parameters. (blue curve: fault duration 0.1275s, stable; red curve: fault duration 0.1335s, unstable)

Next, the control parameters of WTG 7 inside Group 2 are varied to study its impact on the transient stability margin of Group 2. Notice that the control parameters for other WTGs including WTG 8 are kept the same as in Table 3.2. When control parameters of WTG 7 are changed, the two WTGs inside Group 2 no longer have the same control parameters. The proposed CCT calculation method is thus tested for close by WTGs with different control parameters. The results are shown in Table 3 and the dynamic simulation results for WTG 7 and WTG 8 with fault clearing time 0.003s before or after the CCT are shown in Figure 3 through Figure 12. With all the control parameters tested, the calculated CCTs and stability margin indices match closely to the simulated ones, which further demonstrates the effectiveness of the proposed methodology in evaluating CCTs and transient stability margins of the WTGs. It should be noticed that when the control parameters of WTG 7 are changed and are different from those of WTG 8, the CCTs calculated for the two WTGs will be different and the smaller one is chosen as the CCT for Group 2 (described in section 3.6). Therefore when the fault is cleared 0.003s after the CCT, only one of the two WTGs in Group 2 goes unstable while the other one remains stable.

Table 3 CCT and S_m of Group 2 with different control parameters for WTG 7

		CCT_S (s)	CCT_C (s)	Error (%)	S_m_S	S_m_C
Higher PLL gain	K_i=2800 K_p=120	0.0805	0.0798	-0.87	-19.5	-20.2
Lower PLL gain	K_i=700 K_p=30	0.1385	0.1349	-2.60	38.5	34.9
Higher VC gain	K_{vi}=240 K_{vp}=0	0.1330	0.1297	-2.48	33.0	29.7
Lower VC gain	K_{vi}=60 K_{vp}=0	0.1190	0.1148	-3.53	19.0	14.8
Lower DCVC gain	K_{dci}=4 K_{dcp}=1	0.1358	0.1309	-3.61	35.8	30.9

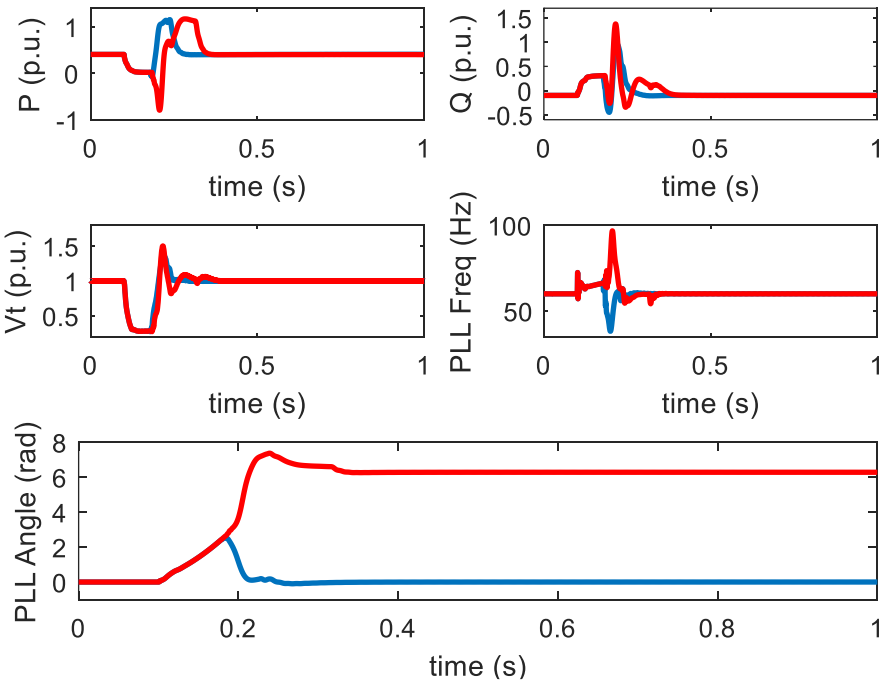

Figure 3 Response of WTG 7 with higher PLL gain. (blue curve: fault duration 0.0775s, stable; red curve: fault duration 0.0835s, unstable)

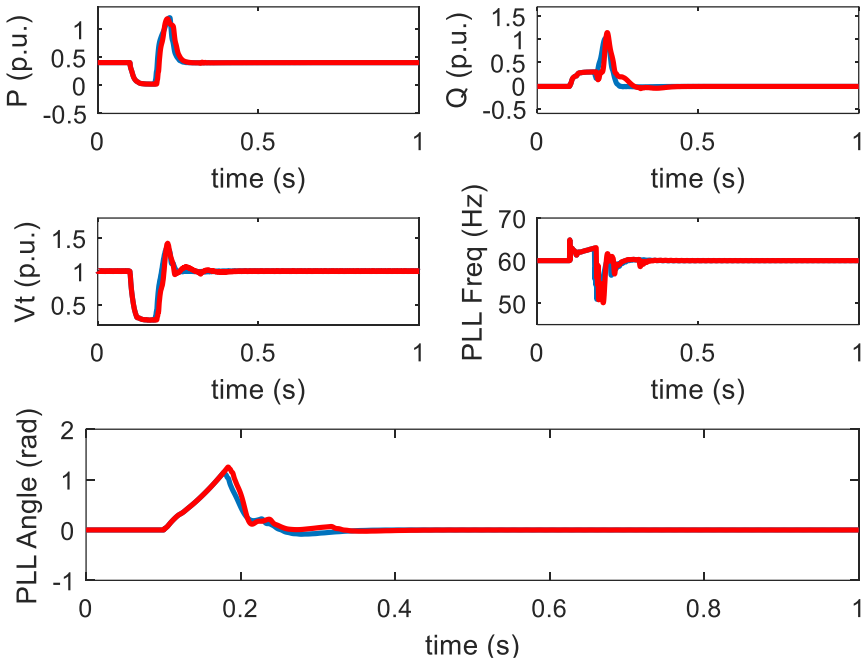

Figure 4 Response of WTG 8 when WTG 7 has higher PLL gain. (blue curve: fault duration 0.0775s, stable; red curve: fault duration 0.0835s, stable)

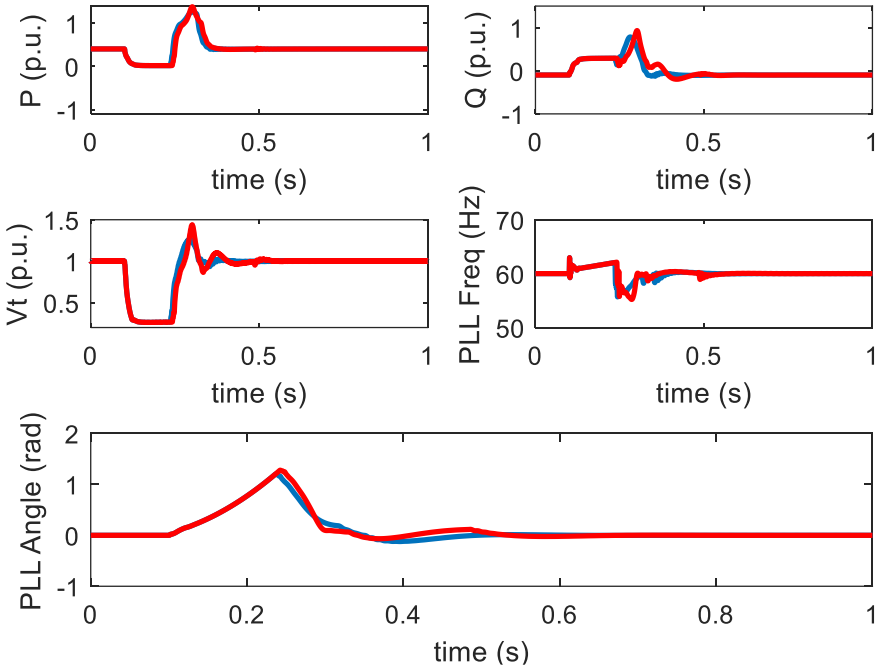

Figure 5 Response of WTG 7 with lower PLL gain. (blue curve: fault duration 0.1355s, stable; red curve: fault duration 0.1415s, stable)

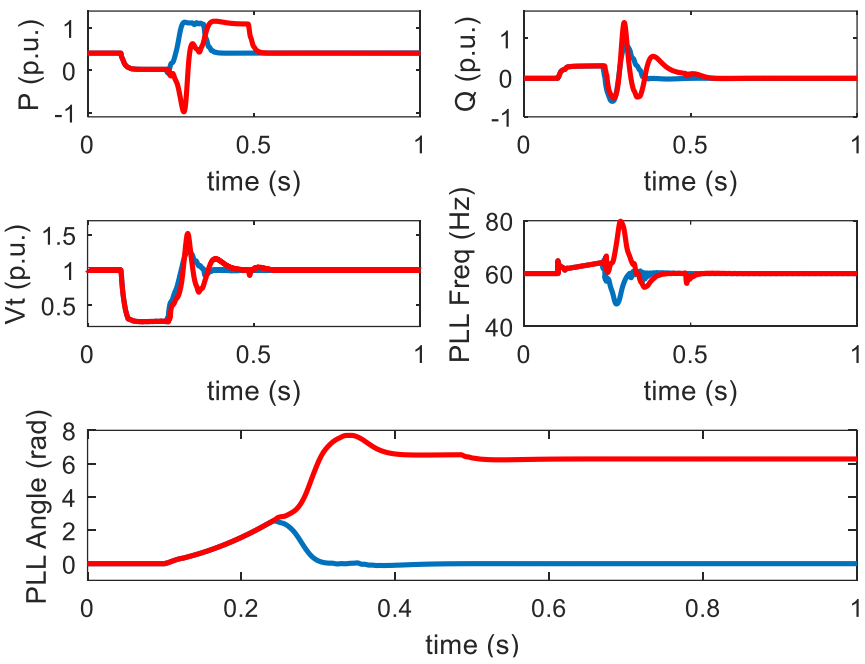

Figure 6 Response of WTG 8 when WTG 7 has lower PLL gain. (blue curve: fault duration 0.1355s, stable; red curve: fault duration 0.1415s, unstable)

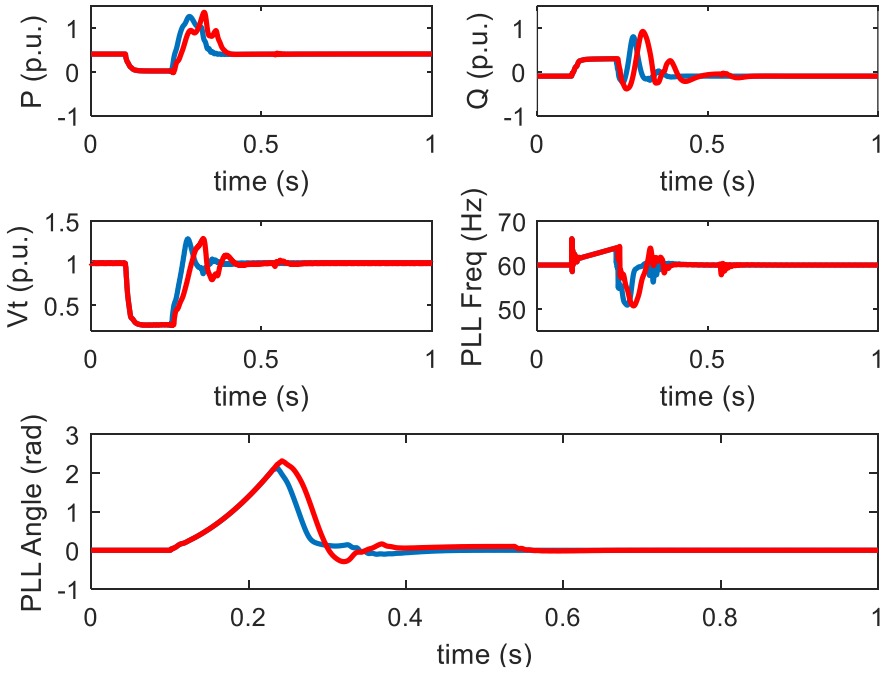

Figure 7 Response of WTG 7 with higher VC gain. (blue curve: fault duration 0.130s, stable; red curve: fault duration 0.136s, stable)

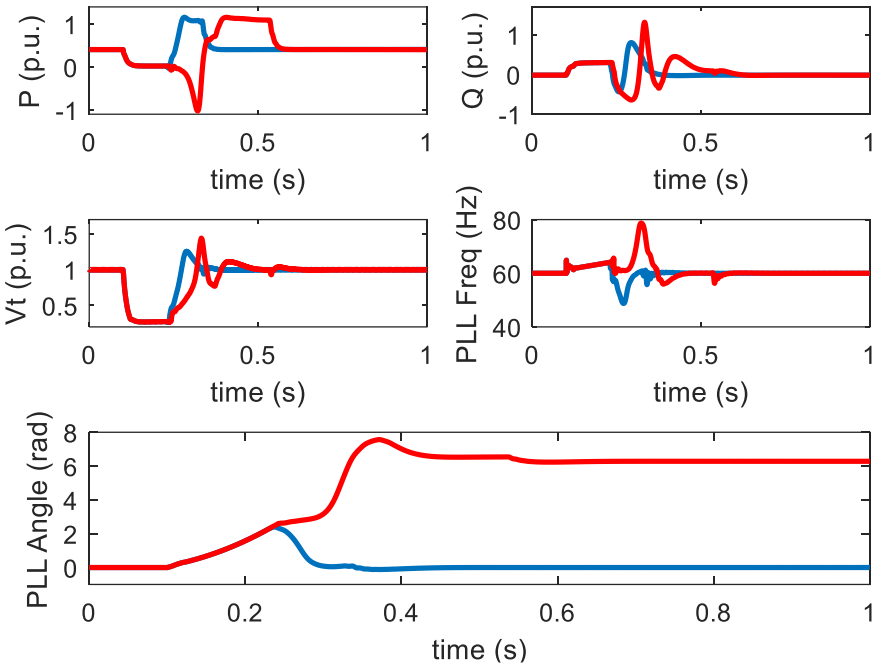

Figure 8 Response of WTG 8 when WTG 7 has higher VC gain. (blue curve: fault duration 0.130s, stable; red curve: fault duration 0.136s, unstable)

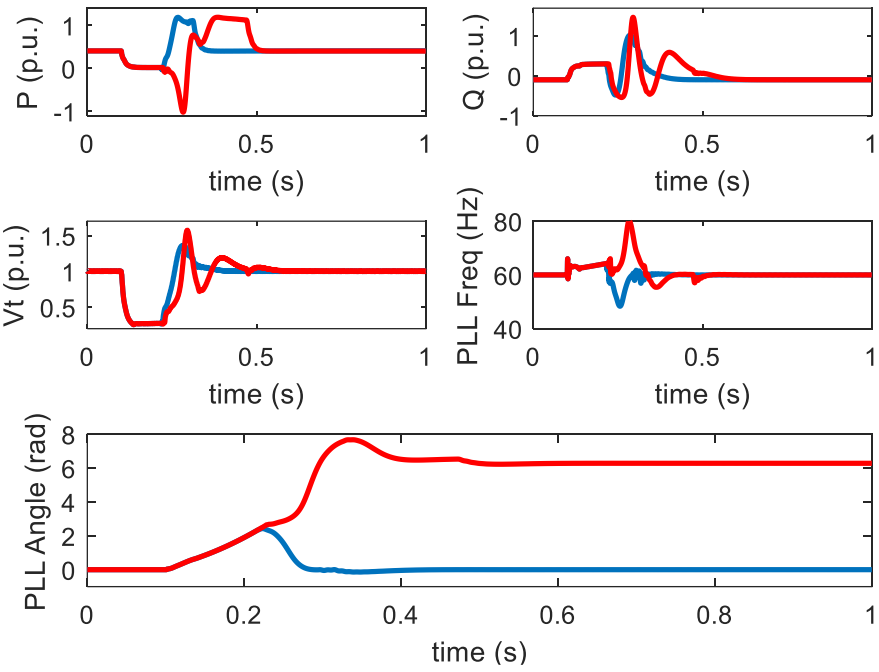

Figure 9 Response of WTG 7 with lower VC gain. (blue curve: fault duration 0.116s, stable; red curve: fault duration 0.122s, unstable)

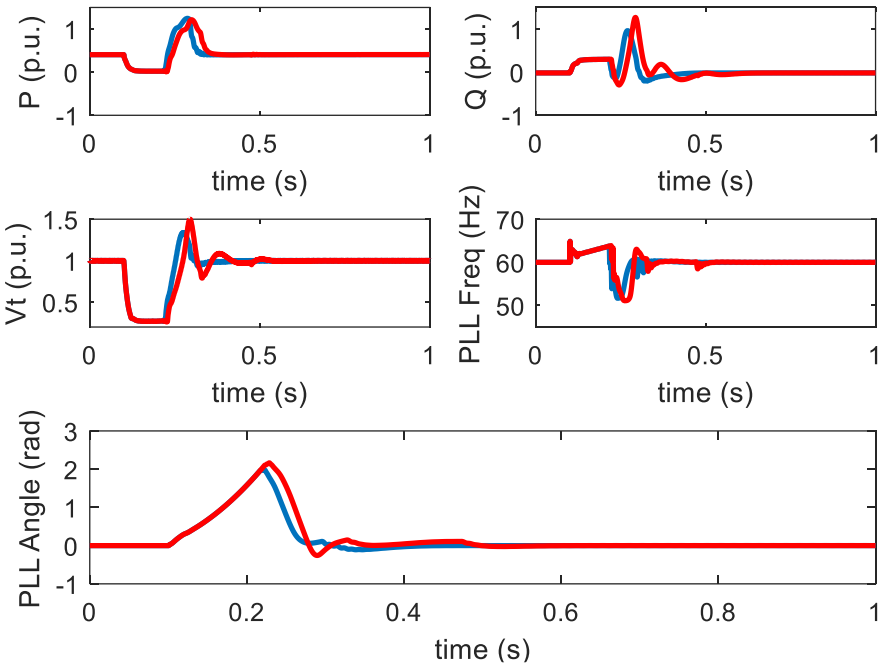

Figure 10 Response of WTG 8 when WTG 7 has lower VC gain. (blue curve: fault duration 0.116s, stable; red curve: fault duration 0.122s, stable)

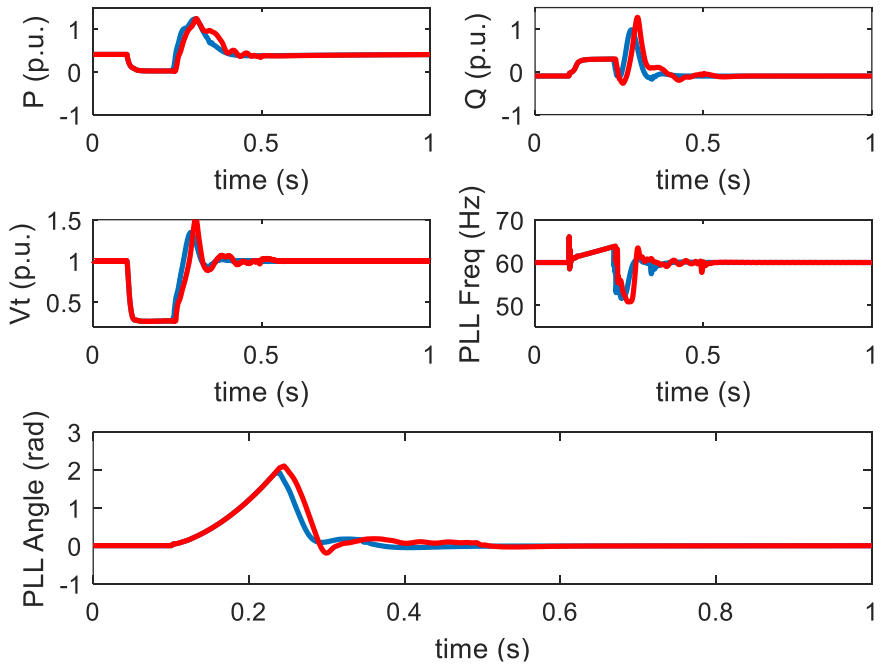

Figure 11 Response of WTG 7 with lower DCVC gain. (blue curve: fault duration 0.1328s, stable; red curve: fault duration 0.1388s, stable)

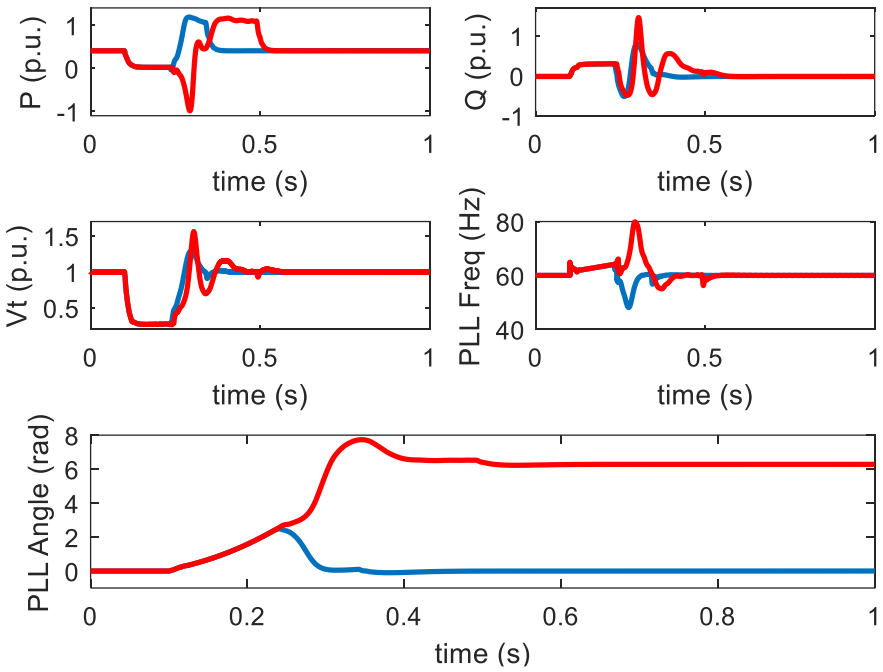

Figure 12 Response of WTG 8 when WTG 7 has lower DCVC gain. (blue curve: fault duration 0.1328s, stable; red curve: fault duration 0.1388s, unstable)